Johannes Götz, B.Sc.

Development and Characterization of Photocuring Thiol-Ene Polymer Systems as Imprint Resins for Ultraviolet Light-Assisted Nanoimprint Lithography

MASTER'S THESIS

to achieve the university degree of

Diplom-Ingenieur

Master's degree programme: Advanced Materials Science

submitted to

Graz University of Technology

Supervisor

Prof. Dipl.-Ing. Dr.techn.
Emil J.W. List-Kratochvil

Institute of Solid State Physics

in cooperation with
JOANNEUM RESEARCH Forschungsgesellschaft mbH

Graz, November 2015

AFFIDAVIT

I declare that I have authored this thesis independently, that I have not used other than the declared sources/resources, and that I have explicitly indicated all material which has been quoted either literally or by content from the sources used. The text document uploaded to TUGRAZonline is identical to the present master‘s thesis dissertation.

Date

Signature

Acknowledgements

I am grateful to Prof. Dr. Emil List-Kratochvil for supervising my master's thesis and his support.

I want to thank Dr. Paul Hartmann for giving me the opportunity to conduct my thesis at the Institute of Surface Technologies and Photonics of the JOANNEUM RESEARCH company and Dr.^{in} Barbara Stadlober for allowing me to join her research team Micro- and Nanostructuring of Materials.

Special thanks goes to Dr. Dieter Nees for being a great advisor who taught me a lot. He critically observed my work and made sure it is thorough but yet gave me enough freedom to work independently and was always available for discussions and giving advice, for which I am very thankful.

I appreciate Stephan Ruttloff for his great experimental support especially at the R2R-machine as well as Wolfgang Nemitz, Dr.^{in} Maria Belegratis, Dr. Christian Wolf and Philipp Schäffner for their help.

I want to thank all collegues at Joanneum Research for the nice working atmosphere.

I am indebted to my parents who offered me the opportunity to study.

I am grateful to Johanna Meuser for her support and the life beyond work.

Abstract

Ultraviolet light-assisted nanoimprint lithography (UV-NIL) is a technique for fabricating micro- and nanostructures. It replicates the surface pattern of a template by pressing it into a liquid monomer solution which polymerizes and gets rigid upon exposure to UV light. In this way the resolution is not limited by the wavelength of light as in the case of photolithography but only be the resolution of the technique used to fabricate the master. Roll-to-roll UV-NIL allows to perform this process in a continuous way and at large areas which enables a cost-effective and high-throughput production. A key feature of the process is the imprint resin as it not only determines the properties of the produced structures but has also to fulfill certain requirements to be suitable for imprinting. Typically, imprint resins are based on acrylates which, however, exhibit some drawbacks such as oxygen inhibition, incomplete conversion, slow reaction, large polymerization shrinkage, shrinkage-induced stress and network inhomogeneity. Thiol-enes have the potential to overcome these limitations and it is the aim of this work to investigate how they can be used to improve conventional imprint resins.

The experimental work comprises a series of techniques to characterize the liquid as well as the cured resin. Rheometry, contact angle measurement, Fourier-transform infrared spectroscopy, hydrostatic weighing and microindentation are employed to measure the viscosity, surface energy, polymerization rate and final conversion, volumetric shrinkage and mechanical properties, respectively. Furthermore, the replication fidelity is investigated using light microscopy, electron microscopy, profilometry and atomic force microscopy.

It was found that thiol-enes generally polymerize at higher rates and to higher final conversions than acrylates. On the other hand, they exhibit limited shelf-life stability which, however, can simply be solved by using them as two-component systems. Regarding their mechanical properties, their hardness is significantly reduced compared to acrylates but their elastic modulus can be comparable to acrylates when using stiff monomers. The investigation of volumetric shrinkage of bulk samples revealed that they tend to shrink less than acrylates which is due to their step-growth polymerization mechanism leading to lower cross-link densities than in the case of acrylates. Surprisingly, it was found that during NIL shrinkage does, however, not significantly reduce the size of imprinted features. This might be explained by the fact that the imprint is constrained by the template and shrinkage is accommodated by density fluctuations inside the imprinted features instead.

Furthermore, replication fidelity may not only be compromised by shrinkage but also by mechanical failure of the imprint resin during demolding. To allow for defect-free replications it is therefore essential that the imprint can be easily removed from the template after polymerization. Unfortunately, it was found that thiol-ene imprints generally adhere well to the template making it much more difficult to separate them from each other than it is the case for acrylates. Therefore, replications made with thiol-ene resins are often not defect-free. In fact, the good adhesion properties of thiol-enes are well known which originates from their low build-up of polymerization-induced stress. Therefore, despite all their advantages, thiol-enes are less well-suited for UV-NIL than acrylates. However, they might turn out as useful additives when used at lower concentrations.

Kurzfassung

Ultraviolettlichtgestützte Nanoprägelithographie (UV-NIL) ist eine Methode zur Herstellung von Mikro-und Nanostrukturen mit der die Oberflächenstruktur eines Stempels repliziert wird, indem diese in eine flüssige Monomerlösung gedrückt wird, welche anschließend durch ultraviolettes Licht polymerisiert und damit gehärtet wird. Die Auflösung ist daher im Gegensatz zur Photolithographie nicht durch die Lichtwellenlänge begrenzt, sondern durch das Verfahren zur Stempelherstellung. UV-NIL kann auch im Rolle-zu-Rolle Verfahren durchgeführt werden, was eine kostengünstige Produktion mit hohem Durchsatz ermöglicht. Eine Schlüsselrolle spielt dabei der verwendete Prägelack, da er nicht nur die Eigenschaften der produzierten Strukturen bestimmt, sondern auch weitere Anforderungen erfüllen muss, um als Prägelack geeigent zu sein. Üblicherweise werden acrylatbasierte Prägelacke verwendet, die jedoch eine Reihe von Nachteilen wie Sauerstoffinhibierung, unvollständige und verhältnismäßig langsame Reaktion, großen Polymerisationsschrumpf und dadurch induzierte Spannungen, sowie inhomogene Netzwerke mit sich bringen. Thiol-Ene weisen viele dieser Probleme nicht oder in verminderter Form auf und sollen daher in dieser Arbeit auf ihre Eignung als Prägelacke untersucht werden.

Mithilfe von Rheometrie, Kontaktwinkelmessungen, Fourier-Transform-Infrarotspektroskopie, hydrostatischem Wiegen und Mikroindentation wurden Viskosität, Oberflächenenergie, Polymerisationsrate und -umsatz, Schrumpf und mechanische Eigenschaften bestimmt. Außerdem wurde die Prägetreue mittels Lichtmikroskopie, Rasterelektronenmikroskopie, Rasterkraftmikroskopie und Profilometrie untersucht. Es zeigte sich, dass Thiol-Ene im Allgemeinen mit höheren Polymerisationsraten und zu höheren Umsätzen reagieren als Acrylate. Andererseits weisen sie eine geringere Lagerstabilität auf, was jedoch einfach durch Handhabung als Zweikomponentensystem gelöst werden kann. Ihre Härte ist deutlich gegenüber Acrylaten reduziert, ihr Elastizitätsmodul kann jedoch durch die Verwendung von steifen Monomeren ähnlich hohe Werte erreichen. Die Untersuchung des Schrumpfs ergab, dass dieser bei Thiol-Enen tendenziell geringer ausfällt als bei Acrylaten. Dies ist ihrem Polymerisationssmechanismus, dem Stufenwachstum, zuzuschreiben, der zu geringeren Vernetzungsdichten als bei Acrylaten führt. Überraschenderweise zeigte sich jedoch, dass die Größe der mittels UV-NIL geprägten Strukturen gegenüber den Originalstrukturen nicht signifikant durch Schrumpf verringert wird. Dies kommt möglicherweise dadurch zustande, dass die Strukturen aufgrund ihrer Wechselwirkung mit dem Stempel sich nicht frei bewegen können und der Schrumpf stattdessen in Form von internen Dichtefluktuationen auftritt.

Ein weiterer wichtiger Aspekt ist die mechanische Belastung des Prägelacks beim Entformen. Um defektfreie Replikationen zu gewährleisten, ist eine einfache Trennung von Stempel und Prägelack essentiell. Ünglicklicherweise zeigen Thiol-Ene jedoch eine gute Haftung, weswegen ihre Entformung erheblich größere Kräfte erfordert, als dies bei Acrylaten der Fall ist, weswegen mit Thiol-Enen oft keine defektfreien Abformungen möglich sind. Die guten Adhäsionseigenschaften von Thiol-Enen sind auf die geringen Spannungen zurückzuführen ist, die sie während der Polymerisation aufbauen und welche wesentlich kleiner ausfallen als bei Acrylaten. Thiol-Ene sind deswegen, trotz ihrer zahlreichen Vorteile, den Acrylaten als Prägelacke für Rolle-zu-Rolle UV-NIL unterlegen.

Contents

1 Introduction **9**
1.1 Applications of nanoimprint lithography . . . 12

2 Theoretical background **13**
2.1 Roll-to-roll nanoimprint lithography . . . 13
2.1.1 Substrate coating . . . 13
2.1.2 Mold filling . . . 13
2.1.3 Polymerization . . . 15
2.1.4 Demolding . . . 15
2.1.5 Summary of material requirements . . . 19
2.2 Photopolymerization . . . 20
2.2.1 Initiation . . . 20
2.2.2 Chain-growth polymerization . . . 21
2.2.3 Network development . . . 22
2.2.4 Polymerization shrinkage . . . 24
2.2.5 Step-growth polymerization . . . 26
2.2.6 Mechanical properties of polymers . . . 29

3 Experimental **32**
3.1 Materials . . . 32
3.2 Methodology . . . 34
3.2.1 Surface energy - contact angle measurement . . . 34
3.2.2 Viscosity - rheometry . . . 35
3.2.3 Degree of conversion - Fourier-Transform Infrared Spectroscopy . . . 36
3.2.4 Shrinkage - hydrostatic balance . . . 40
3.2.5 Mechanical properties - microindentation . . . 41
3.2.6 Pattern replication by nanoimprint lithography . . . 43
3.2.6.1 Batch process . . . 43
3.2.6.2 Residue-free imprinting . . . 43
3.2.6.3 Roll-to-roll process . . . 44
3.2.6.4 Anti-adhesive coating . . . 44
3.2.7 Evaluation of replication fidelity . . . 45
3.2.7.1 Atomic Force Microscopy . . . 45
3.2.7.2 Profilometry . . . 47
3.2.7.3 Scanning Electron Microscopy . . . 48
3.3 Results and discussion . . . 49
3.3.1 Surface energy . . . 49
3.3.2 Degree of conversion . . . 50
3.3.3 Shelf-life stability . . . 54

3.3.4 Volumetric shrinkage of bulk samples 55
3.3.5 Mechanical properties 57
3.3.6 Nanoimprint lithography 60
3.3.6.1 Evaluation of demolding 60
3.3.6.2 Evaluation of shrinkage 62
3.3.7 Roll-to-roll imprinting 69
3.3.7.1 Evaluation of shrinkage 69
3.3.7.2 Long-term behavior 73
3.4 Summary 79

4 Outlook **82**

Bibliography **83**

1 Introduction

"The ability to replicate patterns at the micro- to the nanoscale is of crucial importance to the advance of micro- and nanotechnologies and the study of nanosciences" [1]. However, classical lithography methods are facing restrictions at some points. The resolution of photolithography is limited by the wavelength and reducing the minimum feature size is a challenge for this technique which causes drastically increasing costs. Electron beam lithography is a serial technique which is limited regarding its throughput. Therefore, much effort has been undertaken to explore alternative techniques that enable large-area production of nanostructures at high throughput and low cost. One particular promising candidate that meets these requirements is nanoimprint lithography (NIL) which has been reviewed several times [1][2][3][4][5][6]. Using NIL, a pattern on the surface of a rigid template is replicated by pressing it into a softer material to achieve conformal contact and subsequent hardening of the imprint so that it maintains its shape after separation from the master. The great potential of NIL has been demonstrated soon after its invention and since 2003, NIL is listed in the International Technology Roadmap for Semiconductors (ITRS) for the 32 *nm* node and beyond. NIL was also chosen by the MIT Technology Review as one of ten emerging technologies that will have a tremendous influence in the near future and have the potential to change our lives [7].

Imprint lithography (from the Greek words lithos (stone) and graphein (to write)) has been known for a long time but was introduced into the field of nanotechnology by Chou et al. in 1995 in the form of thermal NIL (also called hot embossing lithography) [8][9]. The process, illustrated in Figure 1.1, is in principle as follows: a mold is pressed into a thermoplastic polymer which is heated above its glass transition temperature T_g causing the polymer to fill in the mold cavities under sufficient pressure and time. Before removing the mold the polymer is cooled below its T_g and thereby gets rigid which leads to a negative replication of the original mold pattern. In their early work the authors already demonstrated 25 *nm* resolution and improved it to sub-10 *nm* resolution in 1997 [10]. Another variant of imprint lithography, namely ultraviolet light assisted NIL (UV-NIL) introduced by Haisma et al. [11] appeared quickly after thermal NIL in 1996. During this process, illustrated in Figure 1.1, the mold is pressed into a liquid monomer mixture. Hardening is achieved by polymerization upon exposure to UV light before the mold is released leading to a negative replication of the original mold pattern. Compared to thermal NIL, UV-NIL has several advantages: (i) there is no need for elevated temperatures which reduces problems arising due to thermal expansion mismatch between substrate and resin, (ii) the lower viscosity of the liquid resin requires lower pressure and reduces the cavity filling time which allows for higher process throughput as does (iii) the lack of a temperature cycle (i.e. heating and cooling of the thermoset which takes several minutes).

A first step towards high-troughput production was the development of step and flash imprint lithography (SFIL) in 1999 [12] in which a relatively small mold is replicated in a step and repeat manner. A continuous UV roll nanoimprinting process has been developed in 2006 by Ahn et al.[13]. Later, Ahn et al. presented a roll-to-roll UV-NIL (R2R-UV-NIL) process in which polymer patterns down to 70 *nm* feature size were continuously imprinted on a

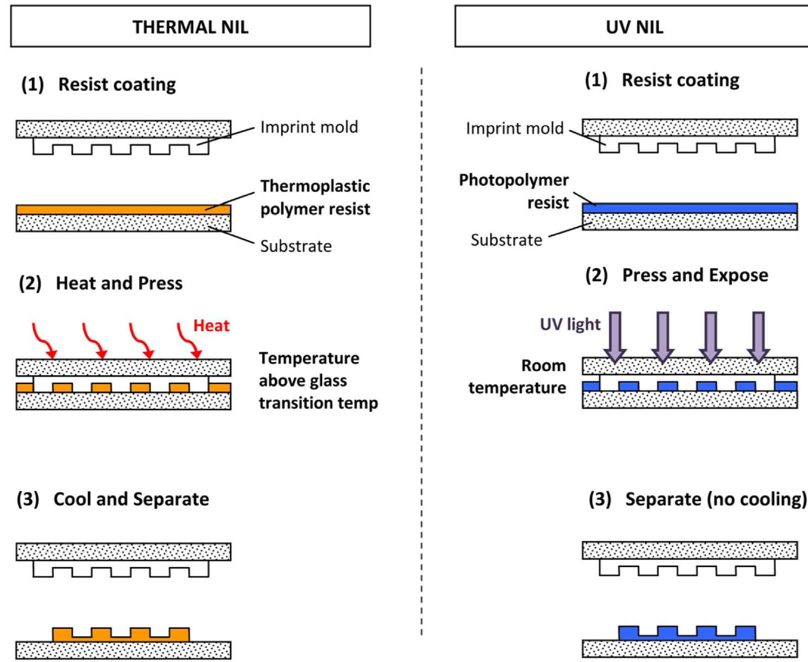

Figure 1.1: Comparison between thermal (left) and UV-NIL (right). During thermal NIL a thermoplastic polymer is heated above its glass transition temperature, imprinted under high pressure, cooled below its glass transition temperature and separated. During UV-NIL a UV curable monomer mixture is imprinted with the stamp using low pressure, exposed to UV light to induce polymerization and separated. Picture taken from [2].

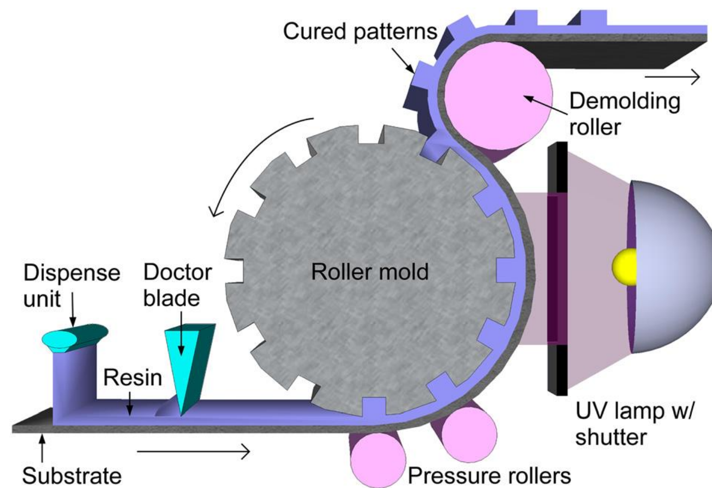

Figure 1.2: The roll-to-roll UV-NIL process basically consists of four steps: coating of a flexible substrate with the liquid monomer mixture, filling of the cavities upon contact with the mold, photopolymerization induced by exposure to UV light and separation of mold and polymer. Picture taken from [3].

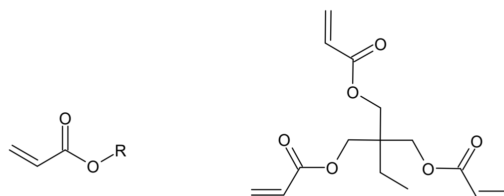

Figure 1.3: Acrylate functional group (left) and a typical multifunctional acrylate monomer (right).

flexible web [14] and demonstrated the capability of large-area imprinting [15] in 2009. In 2012, Dumond et al. reported the fabrication of features down to a size of 50 nm at a web speed of 10 m/min [16]. The R2R process allows a drastically improved throughput and large area patterning while maintaining the nanoscale resolution of conventional NIL. The R2R-NIL process illustrated in Figure 1.2 consists of several steps: (i) coating of a flexible substrate (e.g. PET foil) with the liquid prepolymer mixture (ii) filling of the mold cavities upon contact with the resin (iii) polymerization by exposure to UV light and (iv) separation of mold and resin.

Originally rigid stamps made of quartz glass or silicon were used as stamp material. The R2R process however, requires flexible molds which can be wrapped around the imprint roller. A traditional approach is the use of nickel molds which have high strength and can be replicated by electroforming but their fabrication is expensive. Furthermore, they need a surface treatment to improve their anti-sticking behavior. Another method is the use of polymer stamps. These are negative replicas of a rigid silicon or nickel template fabricated by UV-NIL which can be used as polymer stamp if they provide the required mechanical properties. So once a master template has been fabricated using conventional and expensive techniques like photolithography or electron beam lithography polymer molds can be made from it, proving to be a a very cost effective method. During each imprint the stamp is subject to mechanical stress. Therefore, high demands are put on its mechanical properties because it should be able to faithfully produce replications over as many cycles as possible.

Another key element of the R2R process is the imprint resin as it determines the properties of the final structures and is also responsible for the process throughput. Monomers usually used for this purpose are acrylates because they are well suited for photopolymerizations and offer the possibility to tune the properties of the final polymer over a wide range. The acrylate functional group as well as a typical multifunctional acrylate monomer are depicted in Figure 1.3. However, they have some disadvantages like oxygen inhibition, incomplete conversion, limited curing speed, large polymerization shrinkage, shrinkage induced stress and network inhomogeneity. Thiol-enes, a new class of monomers which have the potential to overcome these drawbacks, have attracted considerable interest. Thiols are organic molecules containing sulfur-hydrogen bonds and the term ene refers to any carbon-carbon double bonds that do not homopolymerize following the notation used in [17]. The addition of thiols to enes (see Figure 1.4) was discovered by Posner in 1905 [18] and they have recently experienced a revival. It is the aim of this work to explore the properties of thiol-enes and how they can be used to improve the imprint resin.

Therefore, Chapter 2 provides the theoretical background about the R2R-process and the requirements it puts on the properties of the imprint as well as the stamp material. Furthermore, the theory of photoinduced polymerization and basic relations between monomer

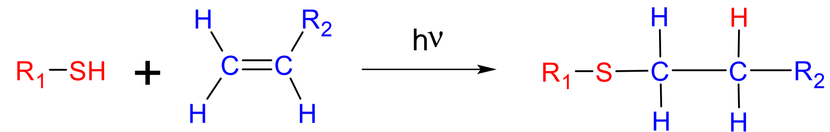

Figure 1.4: Reaction of thiol (R-SH) with an ene (R-C=C).

structure, polymerization characteristics and polymer properties are discussed. Chapter 3 introduces the experimenal methods used in the present work. Finally, the experimental results are presented and discussed.

1.1 Applications of nanoimprint lithography

Before coming to the next section some applications of NIL are presented. Many applications are in the field of biomimetics, i.e. the replication of structures that occur in nature and have interesting properties due to a special surface pattern on the size scale of micro- and nanometers which are reviewed in [19]. A well known example is the lotus effect which provides self-cleaning properties to the leaves of the lotus flower due to a high water repellence (superhydrophobicity). The fabrication of omniphobic (i.e. water and oil repellent) structures by means of NIL was demonstrated in [20]. Another example are anti-reflective coatings which have a great potential in optical applications such as surfaces of lenses, solar cells, light-sensitive detectors, displays and viewing glasses [21]. The direct replication of wings of a cicada was demonstrated by thermal deposition of gold onto the wings which can reduce reflectivity by a factor of ten. This property is due to an array of nanopillars with 400 nm height and 100 nm diameter. The gold template served as a mold in a usual NIL process afterwards. Other interesting properties due to nanopatterned surfaces are drag reduction of shark skin, structural coloration of butterfly wings and the solid-solid adhesion of gecko feet.

NIL has also been applied to fabricate electrical, optical and magnetic devices such as hybrid plastic electronics, organic TFTs and electronics, diffractive optical elements, waveguide polarizers, high resolution OLED pixels, non-linear optic polymer nanostructures , high density quantized magnetic disks, patterned magnetic media and silicon MOSFETs as reviewed in [1].

2 Theoretical background

2.1 Roll-to-roll nanoimprint lithography

In the following R2R-UV-NIL is discussed in further detail and theoretical considerations are presented to understand which requirements are put on the stamp as well as on the imprint material.

2.1.1 Substrate coating

During the first step the PET substrate is coated with the liquid resin by gravure printing which is illustrated in Figure 2.1. The gravure cylinder contains engraved cells that take up the liquid resin from a trough while the cylinder is rotating. Excess resin is removed with a doctor blade. Afterwards, the resin is transferred from the engraved cells to the PET substrate which is pressed against the gravure cylinder with an impression roller. The amount of resin and hence the initial thickness of the resin which is applied to the PET substrate is determined by the size of the engraved cells. This method allows continuous coating of the substrate with a homogeneous and defined layer thickness.

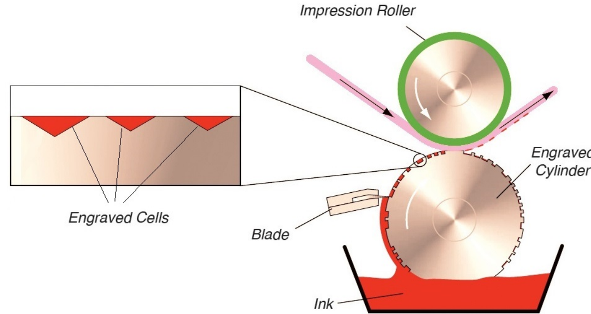

Figure 2.1: Gravure printing is used to coat the PET substrate with the liquid resin. The size of the engraved cells determine the inital thickness of the resin. Picture taken from [22].

2.1.2 Mold filling

In the next step, the resin-coated PET substrate is pressed against the mold which results in filling of the mold cavities. From squeeze flow theory an expression for the filling time t_{fill} can be calculated when a line and space pattern is imprinted (Equation 2.1) as illustrated in Figure 2.2 [23][24]:

$$t_{fill} = \frac{\eta S^2}{2p}\left(\frac{1}{h_f^2} - \frac{1}{h_0^2}\right) \tag{2.1}$$

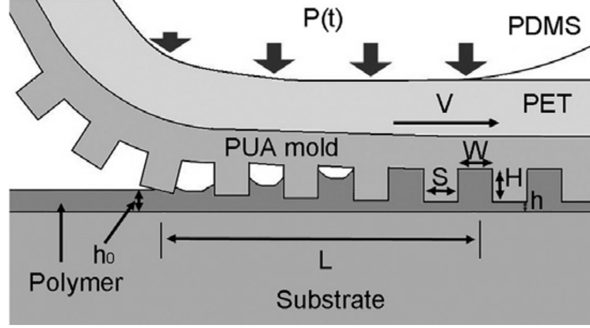

Figure 2.2: Schematic illustration of the cavity filling used to derive Equation 2.1. Picture taken from [23].

The filling time depends on the viscosity η, the intercavity distance S, the applied pressure p, the initial film thickness h_0 and the final film thickness h_f. Of course, it also depends on the cavity geometry (i.e. width W and height H) since the final thickness is connected to these parameters by $h_f = h_0 - \dfrac{WH}{S+W}$ if volume is conserved. The time $t_{contact} = \dfrac{L}{v}$ during which the resin is in contact with the mold is given by the web speed v and the width of the contact zone L. In order to ensure complete filling this time has to be greater than the filling time ,i.e. $t_{contact} \geq t_{fill}$. To achieve high web speed and thus throughput for a given template structure (i.e. given S, H, W) one can increase the pressure or the initial layer thickness. Furthermore, from this equation often the need for liquid resins with viscosity as low as possible is derived.

However, this treatment considers neither capillary forces nor gas which can get entrapped in the mold cavites although both can have a great influence on the filling process. This entrapped gas results in incomplete filling and limits the replication fidelity if it cannot escape. However, the cavities can be further filled by diffusion of the gas through the liquid resin. These effects are discussed in detail in [25]. The importance of the entrapped gas manifests for example in the fact that the initial filling of the cavities is much faster than at the end as the gas pressure increases continuously and impedes further filling at the end. Therefore, it is the gas diffusion and not the viscosity which finally determines the filling time. However, this treatment does not consider the dependance of gas diffusity D on the viscosity η of the liquid. In general, there is an inverse proportionality between the two quantities ($D \propto \frac{1}{\eta}$) [26]. Therefore, it has to be concluded that a lower viscosity decreases the filling time of the mold cavities. Another way to decrease the filling time is a high surface tension of the resin. Furthermore, features with small lateral dimensions get filled faster due to increasing capillary forces but of course deeper features require more time. Due to all these influences a theoretical derivation of the filling time becomes a very complex issue. Gas diffusion through the imprint resin was also investigated in [27]. According to Dumond et al. the overall throughput is not limited by the filling time but by the curing speed when low viscosity resins are used [3]. This might be true for structures in the nanometer scale but the viscosity might be an important parameter for big structures where cavity filling takes much longer time. Furthermore, high-viscosity resins are in general more difficult to handle and problems occur, for example, at the initial coating of the PET substrate when working with high web speeds. Therefore, low-viscosity resins are desirable.

Finally, it should be mentioned that Equation 2.1 predicts an infinite filling time in the case of residual-free (i.e. $h_f = 0$) imprinting. However, Seo et al. argue that below a critical resid-

ual layer thickness spontaneous dewetting takes place which enables residual-free imprinting and that Equation 2.1 is only valid above this critical thickness [23]. When the liquid film approaches a thickness of some hundred nanometers nucleation of a dry patch occurs which subsequently grows at a speed v given by

$$v = \frac{k}{\eta} \frac{S^2}{Eh}, \tag{2.2}$$

where k is a constant, η the viscosity of the liquid resin, S the spreading coefficient, E the elastic modulus of the stamp and h is the film thickness [28][29]. The spreading coefficient is the difference between the interfacial energy of the dry and the wetted contact, respectively and is given by

$$S = \gamma_{SM} - (\gamma_{SR} + \gamma_{MR}), \tag{2.3}$$

where γ_{SM}, γ_{SR} and γ_{MR} are the interfacial energies between substrate and mold, subtrate and resin and mold and resin, respectively. Since the system tries to minimize its interfacial energy, dewetting will only occur when the spreading coefficient is negative. If S is positive, dewetting is not energetically favorable and a nanoscopic film is intercalated between substrate and mold.

Another interesting aspect is the deformation of stamp protrusions when they get covered by the resin because the surface energy induces stress in the material. Using a thermodynamic approach Carillo et al. derived an expression that relates the strain ε (i.e. shape deformation) to the surface energy γ of the liquid resin, the elastic modulus E of the stamp and the initial feature size R_0 [30]. For the sake of simplicity they used cylindrical stamp protrusions with height and radius equal to R_0.

$$\varepsilon \approx \frac{\gamma}{ER_0} \tag{2.4}$$

This equation puts a fundamental limit on the replication fidelity of NIL which gets increasingly important at small size scales. However, this consideration does not put severe restrictions on the choice of materials. Using values of $\gamma = 20\ mJ/m^2$, $E = 200\ MPa$ and $R_0 = 20\ nm$ yields $\varepsilon = 0.5\ \%$. So even with a relatively elastic mold, features down to a size of 20 nm can be reproduced with negligible inaccuracies.

2.1.3 Polymerization

After filling of the cavities the resin is cured upon exposure to UV-light while the resin is in contact to the mold. Depending on the reactivity of the resin a certain amount of time is necessary to reach the final conversion. Therefore, like cavity filling, this step potentially limits the web speed and hence throughput of the process. Volumetric shrinkage induced by polymerization is also an issue as it is expected to reduce the replication fidelity. The origin of polymerization shrinkage and further details about the polymerization mechanism are discussed in Section 2.2.

2.1.4 Demolding

After curing, the resin is separated from the mold. Successfull demolding is crucial because any defects that are created not only decrease the performance of the produced structures but also lead to contaminations of the stamp which will be present in all the following imprints as this is a continuous process. The R2R process is a serious task for the stamp material as

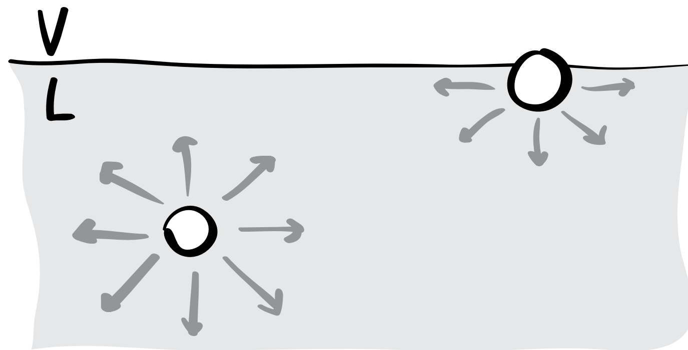

Figure 2.3: Molecules at the surface of a material have missing bonds compared to molecules in the bulk which makes them less energetically favorable. Therefore, surfaces are associated with a specific amount of excess energy, the so-called surface energy. Picture taken from [31].

it should be able to perform almost defect-free imprinting over thousands of imprint cycles requiring excellent mechanical properties. Therefore, it is necessary to enable easy and smooth separation of stamp and cured resin. In order to control the separation process it is important to understand the origin of interactions between resin and stamp. The sticking of the resin to the mold is mainly due to adhesive forces and hence, strongly linked to the concept of surface energy.

To understand surface energy it is instructive to consider the interface between two phases, e.g. a liquid-vapor interface, as depicted in Figure 2.3. Compared to the bulk, surfaces are energetically less favorable for molecules because of missing bonds. Therefore, energy is necessary to increase the surface area and this energy (per unit area) is called surface energy γ. Thermodynamically, it is the derivative of the free energy F with respect to the surface area A at constant temperature T, volume V and particle number n [31].

$$\gamma = \left(\frac{\partial F}{\partial A}\right)_{T,V,n} \tag{2.5}$$

When splitting a liquid into two parts energy is neccessary since two new surfaces are created. This energy, called the cohesive energy per unit area, is given by

$$\frac{W_{coh}}{A} = w_{coh} = 2\gamma. \tag{2.6}$$

The energy neccessary to separate two different materials, as is the case when demolding the resin, is the adhesive energy per unit area which is, according to Berthelot, given by the geometric mean of the cohesive energy per unit area of the two materials:

$$\frac{W_{adh}}{A} = w_{adh} = \sqrt{w_{coh,1}w_{coh,2}} \overset{(Eq.2.6)}{=} 2\sqrt{\gamma_1\gamma_2}. \tag{2.7}$$

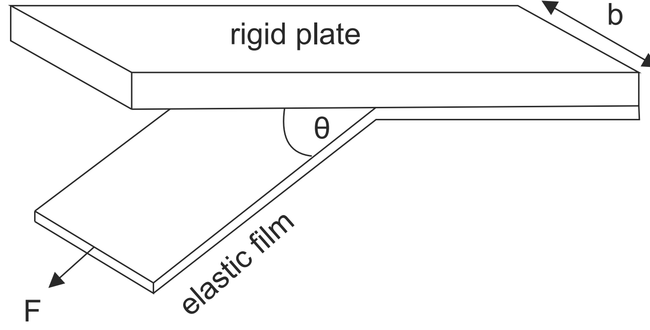

Figure 2.4: Peeling of a thin elastic film adhering to a rigid substrate. Picture modified from [32].

In the R2R-UV-NIL process the cured resin is separated from the mold by peeling as illustrated in Figure 2.4. The energy needed to fracture a unit area of the interface, also called decohesion energy G, is related to the pulling force F via an expression that was originally derived by Rivlin [33][34] (Equation 2.8).

$$G = \frac{F}{b}(1 - \cos\theta) \tag{2.8}$$

where b is the width of the film that is peeled and θ is the peeling angle. This expression can be extended to account for the elasticity of the film, by the Kendall equation [35]:

$$G = \frac{F^2}{b^2}\frac{1}{2Ed} + \frac{F}{b}(1 - cos\theta), \tag{2.9}$$

where E is the elastic modulus and d is the thickness of the peeled film. Another interesting factor has been investigated by Kendall, namely the influence of stress on the adhesive strength [36]. In the case of peeling at an angle of 90° it was found that the force necessary to peel an elastic film from its substrate is lowered if it is pre-strained before separation and can be calculated by

$$\frac{F}{b} = G - \frac{dE\varepsilon^2}{2}, \tag{2.10}$$

where ε is the strain of the elastic film. In order to separate stamp and mold the decohesion energy needs to be larger than the adhesion energy w_{adh}. However, the challenge is not to provide sufficient G since one can simply increase the force as much as necessary. In practice there are two other problems that might impede clean separation.

The first problem is that the resin might stick to the mold instead of sticking to the substrate. To avoid this the adhesion energy between substrate and resin (W_{SR}) has to be higher than the adhesion energy between mold and resin (W_{MR}).

$$W_{SR} \geq W_{MR} \tag{2.11}$$

One should also keep in mind that the surface area of the mold is greatly increased due to the pattern, which further increases the adhesion between mold and resin. Therefore, Relation 2.11 becomes

$$w_{SR} \cdot A_{substrate} \geq w_{MR} \cdot A_{mold}. \tag{2.12}$$

$$w_{SR} \geq w_{MR} \frac{A_{mold}}{A_{substrate}} \tag{2.13}$$

Consider, for example, a pattern of lines and spaces with width w, height h and length l. The ratio between the surface areas of the flat substrate and the patterned mold is then

$$\frac{A_{mold}}{A_{substrate}} = \frac{2wl + 2hl}{2wl} = 1 + \frac{h}{w}. \tag{2.14}$$

Substituting this into Relation 2.13 yields

$$w_{SR} \geq w_{MR}(1 + \frac{h}{w}). \tag{2.15}$$

This means that the adhesion to the mold increases linearly with the aspect ratio h/w of the mold pattern. This is due to the increasing contribution of the sidewall area to adhesion. Furthermore, adhesion is independent of the size scale of the pattern if the aspect ratio is kept constant. Nevertheless, denser structures will lead to increased adhesion. This has been found experimentally by Nishino et al.[37] but without giving the Relation above. Of course, Relation 2.15 looks different for other mold geometries but can be easily adapted.

Besides the surface area also surface energy is important for adhesion as can be seen when substituting Equation 2.7 into Relation 2.13:

$$\gamma_S \geq \gamma_M \left(\frac{A_{mold}}{A_{substrate}} \right)^2 \tag{2.16}$$

So, in order to make sure that the resin sticks to the substrate and not to the mold, the surface energy of the substrate should be high whereas that of the mold should be sufficiently low. Another possibility would be to roughen the substrate to increase its surface area [38]. The surface energy of the resin does not play a role in preventing this adhesive failure, i.e. sticking to the mold instead of the substrate.

Adhesion is not the only mechanism that complicates demolding. Also friction forces acting on the sidewalls of the features have a significant contribution [39][40]. This can have surprising effects. Shrinkage should make separation easier as it already leads to detachment of the resin. In the application of UV coatings it is well known that shrinkage reduces the adhesion to the substrate [41]. In contrast, it was found that shrinkage can actually increase the force necessary for demolding in NIL. It is argued that due to global shrinkage of the resin there is pressure acting against the sidewalls which increases friction and therefore, makes separation more difficult [42]. Furthermore, atmospheric pressure can be an issue as it tries to prevent the formation of voids in the case of high aspect ratio features. However, it has been shown that both friction and the influence of atmospheric pressure can be significantly reduced by inclining the sidewalls with angles as low as 5° [5].

The second problem beside sticking to the mold instead of the substrate that might hinder successful demolding is that the imprinted features might break before the separation force is high enough to achieve demolding. An additional difficulty is that the stress acting on the imprinted features is not distributed homogeneously but rather concentrated at the corners of the features which therefore are the weakest point [43]. To avoid fracture it has to be ensured that the resin has sufficient strength to withstand the demolding stresses. Mechanical properties and their correlation to molecular structure are discussed further in Section 2.2.6. Furthermore, the resin should have a low surface energy to decrease adhesion to the mold. Easy

demolding is especially important for features with high aspect ratio where the big sidewall area increases both adhesion and friction. As indicated by Equation 2.15, demolding is independent of the size scale of the pattern. Since it is the aim of NIL to go to features sizes beyond the photolithographic resolution, it is encouraging that demolding does not get more difficult at small size scales.

2.1.5 Summary of material requirements

From the considerations made so far a variety of requirements can be derived that have to be fulfilled by the imprint and the stamp material. The stamp should have high mechanical strength and durability to guarantee defect-free imprinting over many imprint cycles and yet enough flexibility to be wrapped around the imprint roller. To allow for easy separation of the imprinted features a low surface energy is necessary. To enable a high-throughput process the imprint resin should fill in the mold cavities quickly and completely, and should exhibit high reactivity to allow for fast curing. To ensure defect-free demolding the resin should have a low surface energy and sufficient mechanical strength. Nevertheless, it has to adhere well to its substrate to prevent adhesive failure. Therefore, the substrate should have a high surface area and surface energy. Furthermore, a low viscosity is desirable. Both the imprint and the stamp should exhibit low shrinkage induced by polymerization to guarantee a faithful replication of the template. Depending on the application of the final strucutres further demands are put on the imprint resin e.g. thermal or chemical resistance, weatherability, etch resistance or certain optical properties.

2.2 Photopolymerization

As mentioned before, polymerization is achieved by exposure to UV light. Photoinduced polymerization is widely applied due to its benefits, e.g. it is economical and offers spatial and temporal control [44][45]. Acrylate functional groups are well suited for photopolymerization due to their comparably high reactivity and because they can be incorporated into oligomers with a huge variety of backbone chemistries to tune the properties of the final polymer [46]. As discussed in Section 2 there is a series of material requirements to meet for the R2R-UV-NIL process. Therefore, it is important to know how the monomer structure and the polymerization mechanism and kinetics influence the final polymer properties which is discussed in the following.

2.2.1 Initiation

The polymerization of acrylates proceeds via a free-radical chain-growth mechanism. The first step is the absorption of light by photinitiators which subsequently generate the radicals that are necessary to start the polymerization. Photoinitiators are necessary because acrylate functional groups interact with light very weakly. Initiation proceeds in several steps as illustrated in Figure 2.5. Upon absorption of light the photoinitiator molecule is excited into a higher sin-

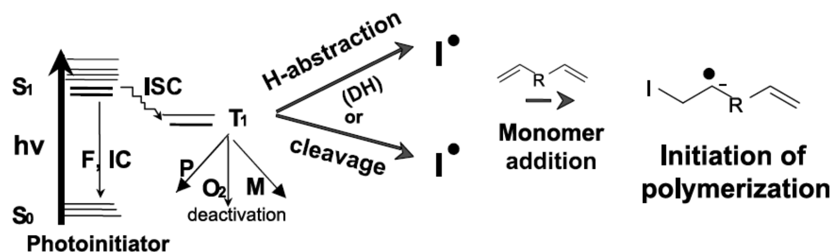

Figure 2.5: Schematic illustration of the initiation process of free-radical photopolymerizations. Upon absorption of a photon with energy $h\nu$ the photoinitiator is excited from the ground state S_0 to an excited singlet state S_1. An inter-system crossing (ISC) creates excited triplet states T_1 which lead to the generation of radicals $I^\bullet$. Loss mechanisms are fluorescence (F), non-radiative decay by internal conversion (IC), phosphorescence (P) and quenching by oxygen O_2 or monomer (M) molecules. Picture taken from [41].

glet state. First, this state can decay into the ground state by non-radiative internal conversion or fluorescence or, second, be converted to an excited triplet state by inter-system crossing. Radicals are rather produced from triplet states where unpaired electrons are present than from singlet states. The excited triplet state can, first, be deactivated by phosphorescence or oxygen quenching or, second, react with monomers leading to the desired radicals. The quantum yield of initiation defined as the number of growing chains per photon absorbed is thus dependant on a number of processes. Depending on the type of the photoinitiator molecule different mechanisms lead to the formation of radicals. Norrish type I initiators, usually aromatic carbonyl compounds, produce radicals via photofragmentation as depicted in Figure 2.6. One or both fragments may contribute to the initiation process. Norrish type II initiators, typically aromitc ketones, abstract hydrogens from donor molecules. A typical example is benzophenone as depicted in Figure 2.7. The resulting ketyl radical is relatively stable and does not initiate

the polymerization but can terminate other radicals. Oxygen quenching of triplet states is not important for type I initiators due to the short lifetime but plays a role in the case of type II initiators where triplet state lifetime is significantly longer.

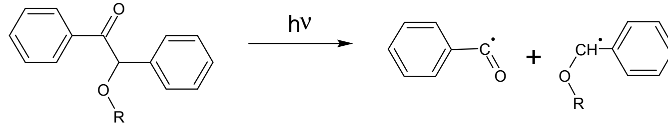

Figure 2.6: Photofragmentation of a Norrish type I initiator.

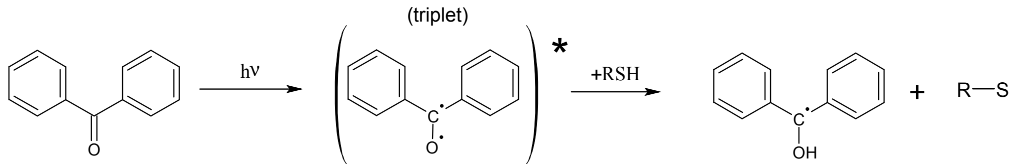

Figure 2.7: Triplet formation and subsequent hydrogen abstraction of a Norrish type II initiator.

2.2.2 Chain-growth polymerization

After the initial radicals are formed by the reaction of a photoinitiator radical $I^\bullet$ with a monomer M the created radicals can again react with another monomer. This leads to a growing polymer chain $M_i^\bullet$ the radical being transferred to the chain end at each step which is called propagation. Finally, when two active polymer chains react with each other the chain growth is terminated leading to the final polymer chain P_{x+y}.

$$I^\bullet + M \rightarrow M_1^\bullet \tag{2.17}$$

$$M_n^\bullet + M \overset{k_p}{\rightarrow} M_{n+1}^\bullet \tag{2.18}$$

$$M_x^\bullet + M_y^\bullet \overset{k_t}{\rightarrow} P_{x+y} \tag{2.19}$$

Based on this scheme rate equations can be written that describe the concentration of each species throughout the polymerization. In photopolymerizations the rate of initiation R_i (i.e. the number of radicals created per time) is given by the intensity I_a of the absorbed light and the initiator efficiency ϕ.

$$R_i = 2\phi I_a \tag{2.20}$$

The optional factor two is because each initiator molecule produces two radicals (might be different for other initiators). Based on the Beer-Lambert law the absorbed light intensity at a certain depth d can be expressed as [47][48]

$$I_a = 2.3\varepsilon c \cdot I_0 e^{-2.3\varepsilon c d} \cdot \frac{\lambda}{N_A h c} \tag{2.21}$$

where I_0 is the initial light intensity, ε the molar extinction coefficient and c the concentration of photoinitiators. The factor consisting of the wavelength λ, Avogadro constant N_A, Planck

constant h and the speed of c converts the incoming light intensity into number of photons per unit area. For very thin films the absorbed light intensity is approximately independent of the depth and one can write

$$I_a = 2.3\varepsilon c I_0 \frac{\lambda}{N_A hc} \tag{2.22}$$

Assuming termination is by biomolecular combination only which is valid for acrylate polymerization the rate of termination R_t (i.e. the number of radicals consumed per time) is given by

$$R_t = -2k_t[M^\bullet]^2 \tag{2.23}$$

where k_t is the termination rate constant and $[M^\bullet]$ the radical concentration. The change of radical concentration is given by R_i and R_t.

$$\frac{d[M^\bullet]}{dt} = R_i + R_t \tag{2.24}$$

The rate of polymerization (i.e. the rate of monomer disappearance) is given by the rate of propagation R_p and the rate of initiation. However, the latter is normally negligible at low initiator concentrations. Therefore,

$$-\frac{d[M]}{dt} = R_p = k_p[M][M^\bullet] \tag{2.25}$$

where k_p is the propagation rate constant and $[M]$ the monomer concentration. The degree of conversion DC is defined as the fraction of monomers that have reacted after a certain time t and is given by

$$DC(t) = 1 - \frac{[M](t)}{[M](0)}, \tag{2.26}$$

where $[M](t)$ is the monomer concentration at time t and $[M](0)$ is the initial monomer concentration.

2.2.3 Network development

The scheme presented so far is, however, oversimplistic and in reality a number of complexities arise during polymerization which will be discussed in the following [44][45][49][50][51]. The chain-growth nature of acrlyate polymerizations leads to a fast increase in molecular weight meaning that relatively long chains are created at early stages of the polymerization which are mainly surrounded by unreacted monomers. Due to their large size their mobility is very limited and as termination is a bimolecular reaction between two radicals the termination rate greatly decreases. In cross-linking polymers the radical mobility is restricted so much that they are more mobile due to propagation than due to diffusion. The propagation reaction is unaffected because the unreacted monomers keep their mobility and can easily diffuse to the radicals. The decreased termination rate leads to an increase of the radical concentration and hence, to a greatly increased polymerization rate at relatively low conversions (known as Trommersdorf effect or autoacceleration). Furthermore, the termination rate depends on the initiation rate. Higher initiation rates lead to shorter kinetic chains (at equal conversions) which means they are more mobile and terminate faster.

Another complexity which happens in the case of multifunctional monomers is the formation of microgels at the early stages of polymerization (Figure 2.8). When multifunctional

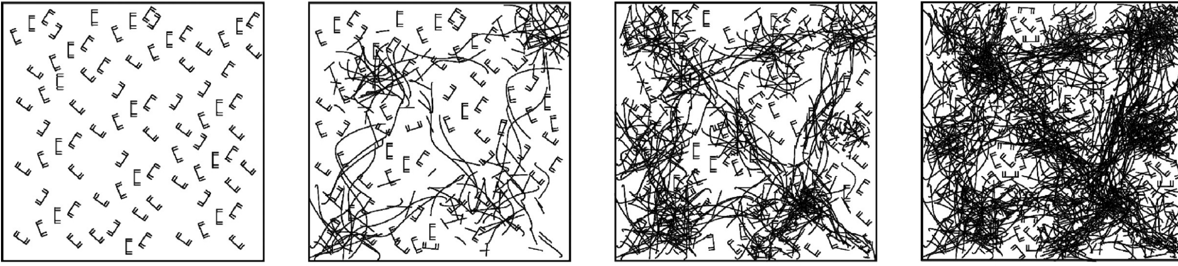

Figure 2.8: Schematic illustration of network evolution (from left to right). The polymerization of multifunctional monomers via chain-growth mechanism leads to the formation of locally highly cross-linked regions (called microgels). With ongoing reaction these microgels join together which eventually leads to a heterogenous network and in the case of polymers with high glass transition temperature to incomplete reactions. Picture taken from [53].

monomers are connected, a chain builds up that contains pendant double bonds. They react more easily compared to monomeric double bonds because of their vicinity to the radical sites. This intramolecular cross-linking (or primary cyclization) leads to the formation of so-called microgels - compact molecules, inside a liquid matrix and is the reason for the inhomogeneity of the final network that can significantly reduce its mechanical strength. They are sometimes called wasted cross-links as they do not contribute to the mechanical strength of the polymer. As the polyermization proceeds the microgels join together building a macroscopic gel - a stage called gel-point that typically occurs below 10 % conversion. From this point on the polymer starts to develop a modulus and the glass transition temperature T_g (see section ref) rises continuously. When a dense network builds up the propagation reaction also becomes diffusion controlled as the diffusion of unreacted monomers to radicals becomes more difficult. This leads to a continuously decreasing polymerization rate with ongoing reaction (known as autodecceleration). If T_g becomes greater than the ambient temperature the polymer vitrifies and is in the glassy state. At this stage the network heterogeneity is inverted as there are microscopic regions of unreacted monomers in an otherwise cross-linked network. Often, there are no initiator molecules in these monomeric pools which therefore, remain unreacted although initiation continues. Also radicals can be trapped in the network and have been shown to be stable over long time periods. For polymers with T_g much higher than the temperature during polymerization the reaction is therefore limited to conversions which can be as low as 60 %. However, other than frequently stated, the reaction does not stop after vitrification as shown by Kloosterboer et al. [52]. The reaction rate drops far below 1 % of the maximum rate, but as long as initiation continues the reaction (albeit at a steadily decreasing rate) proceeds until a topological limit is reached. The polymerization is still going on although as expected from the applied light dose (see section 2.2.1) the initiator concentration should be negligibly small. This is because the initiator efficiency continously decreases during polymerization and therefore, even after long irradation times initiator molecules exist [45][52]. From a practical point of view the reaction stops soon after the glass transition temperature passes the curing temperature because conversion does not increase anymore at reasonable time scales.

Another complexity arises due to the fact that the polymer shrinks during polymerization (which will be further discussed in section 2.2.4). This is because long ranged van der Waals bonds are replaced by shorter covalent bonds thereby generating free volume that is subse-

quently transformed into overall shrinkage. In principle, shrinkage should be proportional to the extent of reaction. As most of the polymerization occurs after gelation the gel has to move as a whole to convert this free volume into overall shrinkage. This macroscopic motion is inherently slower than the diffusion of small molecules and therefore, shrinkage lags behind monomer conversion as shown by Kloosterboer [49]. Some researchers propose (Kloosterboer et al. [54], Anseth et al. [55]) that due to the generation of free volume the molecules are more mobile and therefore higher final conversions can be achieved at high light intensities where a greater part of the reaction takes places in the unrelaxed state. However, Kloosterboer et al. corrected their former work [52][49] and showed that when equal light doses are applied equal conversions are obtained. In fact, lower light intensities lead to slighty higher conversions which the authors explain by the increased kinetic chain length decreasing the termination rat. Their previous results were due to experimental inaccuracies (DSC is not able to detect very slow reactions, the conversion measured for different light intensities was obtained at unequal light doses.)

These findings are valid for the rather low light intensities used in their investigation (2 mW/cm^2). At much higher light intensities conversion depends on the light intensity which has however another reason. As discussed before, the glass transition temperature rises with ongoing reaction but it cannot exceed the curing temperature by a certain limit at practical time scales because the monomer diffusion gets increasingly restricted in a densely cross-linked network. If T_g reaches this limit the reaction essentially stops. Since polymerization of acrylates is an exothermic reaction the temperature of the samples increases during polymerization which is especially pronounced at high light intensities where the reaction proceeds faster, hence producing more heat at the same time. For example the maximum temperature of an urethane diacrylate polymerization has been found to be $40°C$ at 10 mW/cm^2 but $90°C$ at 80 mW/cm^2 [41]. This elevated temperature is the reason for the increased conversion obtained at higher light intensities and also makes it possible to achieve glass transition temperatures much higher than room temperature. In a computational study it was found that the temperature increase is negligibly small during the SFIL process due to fast heat transfer to the mold and the substrate [56]. However, this is mainly because of the high thermal conductivity of the mold and the substrate consisting of fused silica and silicon, respectively and because of the relatively low light intensity below 100 mW/cm^2. In the R2R-process used in the present work the resin is between a substrate and mold, which are both polymers having a much lower thermal conductivity than fused silica. Furthermore, the UV-lamp employed here has a much higher intensity of up to 2.2 W/cm^2 which probably leads to significant heating of the resin during polymerization.

2.2.4 Polymerization shrinkage

As already mentioned volumetric shrinkage occurs during polymerization. Shrinkage defined by Equation 2.27 is typically about 15 % in the case of acrlyates [57]. Therefore, it has the potential to significantly reduce the replication fidelity of the NIL process as illustrated on the left of Figure 2.9 as the resin (blue) does not maintain the shape of the master (black) during polymerization.

$$Shrinkage := \frac{V_{monomer} - V_{polymer}}{V_{monomer}} = \frac{\Delta V}{V} \tag{2.27}$$

To improve the pattern fidelity it is tried to reduce this value by developing low-shrinkage resins. Therefore, it is neccessary to understand the relationship between the molecular struc-

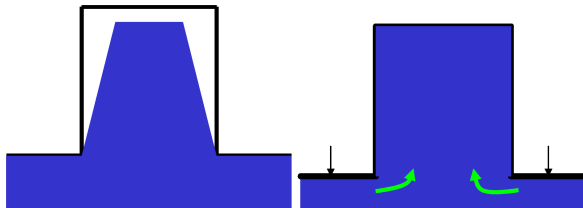

Figure 2.9: Polymerization shrinkage leads to a decreased shape replication fidelity (left). Thiol-enes reduce this effect by liquid flow into the mold cavities due to their delayed gel-point thereby reducing the residual layer thickness (right). Picture modified from [58]

ture and the final shrinkage. As generally accepted, the reason for polymerization shrinkage is the replacement of long-ranged van der Waals bonds by short-ranged covalent bonds [59]. A semi-empirical relationship can be derived [60][61] when considering that each double bond contributes a constant amount of shrinkage when polymerizing, which is given by so called shrinkage factor S. The volumetric shrinkage is, therefore, given by the shrinkage factor times the initial concentration $[RG]$ of reactive groups:

$$\frac{\Delta V}{V} = S \cdot DC \cdot [RG] \tag{2.28}$$

Of course, the degree of conversion DC also needs to be included, because unreacted monomers do not contribute to shrinkage. Since $[RG]$ is given by the reciprocal molar volume V_M times the functionality f of the monomer one can write

$$[RG] = \frac{f}{V_M} = \frac{f\rho}{M}, \tag{2.29}$$

where ρ is the density and M the molar mass of the monomer. This expression can be extented to the case when a mixture of monomers is polymerized:

$$[RG] = \frac{\sum_i f_i \chi_i}{\sum_i M_i \chi_i} \rho_{mix}, \tag{2.30}$$

where χ_i is the mole fraction of monomer i and ρ_{mix} is the density of the monomer mixture. This equation allows to calculate the shrinkage from basic properties of a molecule when the shrinkage factor S is known. It is generally believed that the shrinkage factor is solely determined by the functional group chemistry and is independent of the molecular structure, i.e. all acrylates should exhibit the same shrinkage factor. Therefore, once the shrinkage factor has been determined shrinkage can be calculated for every molecule with the same functional groups. Patel et al. investigated the shrinkage of a variety of methacrylates in 1987 and found a constant shrinkage factor of $S = 22.5\ cm^3/mol$ [62]. According to Jian et al. acrylates exhibit a shrinkage factor of $S = 24\ cm^3/mol$ [63].

Regarding the above expression the volumetric shrinkage can be reduced by simply increasing the molar mass of the monomer but this usually goes hand in hand with a great increase of viscosity which is unwanted as well. Furthermore, this would reduce the cross-link density and mechanical strength as is the case when decreasing the functionality of the monomer. However, the mechanical strength does not only depend on the cross-link density but also on the glass

transition temperature which in turn is rather influenced by the stiffness of the monomers and less by its molecular weight (i.e. size). Therefore, it is possible to produce polymers with low-shrinkage (due to the relatively large size of the monomers) but still high glass transition temperature (due to their stiffness) [62].

Note that the relation above is only valid when a linear relationship betwenn shrinkage and conversion is assumed. This is true for some polymers and shrinkage has been used to measure conversion in some cases, e.g. in [55]. In general, shrinkage is however not a measure of conversion [49]. It was shown by de Boer et al. that after vitrification shrinkage does not increase linearly with conversion anymore and free volume will finally be frozen in, not being converted into overall shrinkage [64].

2.2.5 Step-growth polymerization

Although acrylates have found a wide range of applications they also suffer from some disadvantes such as oxygen inhibition, incomplete conversion, slow reaction, large polymerization shrinkage, shrinkage induced stress and network inhomogeneity. Thiol-enes have the potential to overcome these limitations which is why they have attracted consiberable interest and a lot of research has been done in this area which is reviewed in several papers [65][66][67][68][69]. The basic reaction mechanism was presented by Kharasch et al. in 1938 [70].

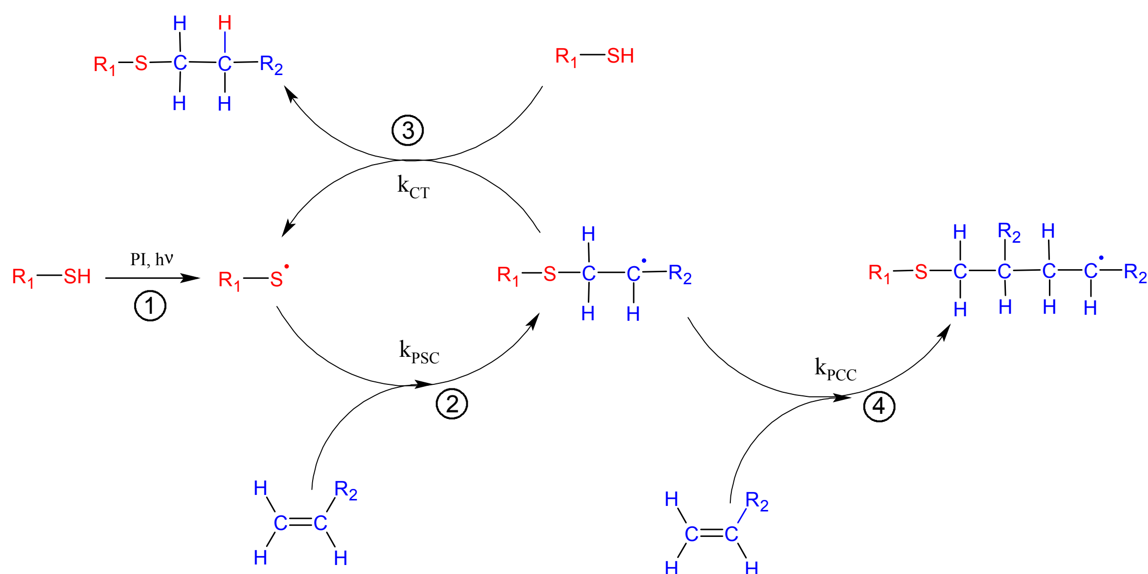

Figure 2.10: General process of thiol-ene polymerisation.

The reaction of thiol-enes is fundamentally different from the chain growth mechanism of acrylates and proceeds via a step-growth mechanism as depicted in Figure 2.10. The ideal thiol-ene reaction basically consists of alternating propagation (2) and chain-transfer (3) reactions that continuously cycle. In the initiation step (1), the radical that was produced via UV light, abstracts a hydrogen from a thiol creating a thiyl radical. This radical propagates through a carbon-carbon double bond (2) leading to a carbon radical which in turn abstracts a hydrogen from a thiol, thereby regenerating the thiyl radical and building the final product (3). Termination (which is not shown in Figure 2.10) occurs also by biomolecular combination, however, other than in chain growth polymerization, three possibilities exist: combination be-

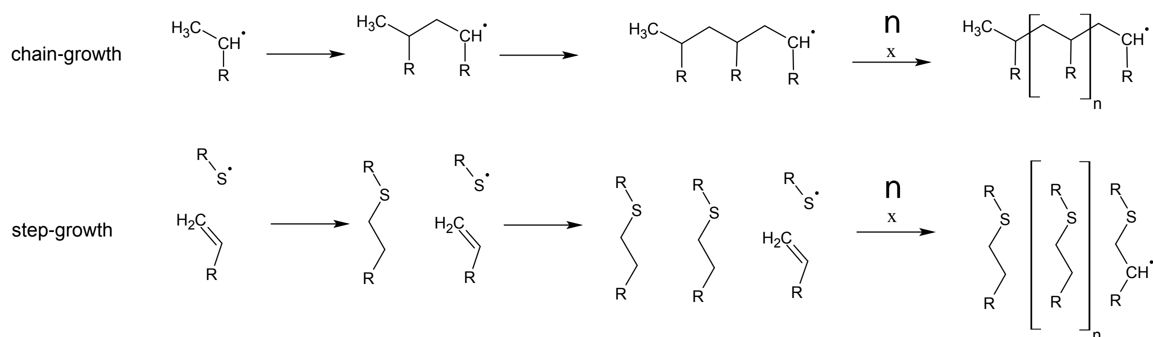

Figure 2.11: Molecular weight evolution in chain- and step-growth polymerizations.

tween (i) two thiyl radicals, (ii) two carbon radicals or (iii) a thiyl and a carbon radical. This scheme is the reaction mechanism of an ideal thiol-ene reaction where only heteropolymerization takes place leading to pure step-growth. However, the carbon radical that was created during the propagation step has a second possibility (4): it can undergo homopolymerization and react with another carbon-carbon double bond, i.e. following a chain-growth mechanism. This leads to an ene conversion greater than the thiol conversion. Usually, little to no homopolymerization occurs depending on the ene functional group chemistry. However, it is very pronounced in the polymerization of thiol-acrylates in which a mixed step-chain growth mechanism occurs. To distinguish between the two cases double bonds that are able to homopolymerize are termed vinyls whereas enes refer to double bonds that undergo little to no homopolymerization, following the notation used in [17].

Cramer et al. presented a model describing the kinetics of thiol-ene systems [71]. An interesting factor is how the monomer structure influences the reactivity. They found that either chain-transfer or the propagation reaction can be the rate limiting step. Specifically, they proposed that the chain-transfer reaction mainly depends on the carbon radical stability and the thyil radical propagation depends on the electron density of the double bonds. The fastest ene functionalities are norbornenes, followed by vinyl ethers, acrylates and allyl ethers. Allyl ethers lead to relatively stable radicals explaining their slow polymerization. The high reactivity of norbornenes is due to the alleviation of ring stress. Similarly, the most reactive thiols are thiol glycolates and thiol propionates. In general, the thiol-ene polymerization rate is at least as high as for acrylates and the addition of thiol to acrylates increases the polymerization rate. This is of special interest regarding the throughput of the R2R-NIL process.

One characteristic feature of the step-growth mechanism is the relatively slow increase of molecular weight with respect to conversion as depicted in Figure 2.11. When polymerizing monofunctional monomers after n propagation steps a chain with n repeating units has built up with a chain-growth mechanism, whereas n single adducts are created in a step-growth polymerization. In many cases almost no monomers are present when the average polymer chain contains only about ten repeating units [47]. In contrast, in chain-growth polymerizations long chains already build up at relatively low conversions, but monomers are still present in the later stages of polymerization. On the one hand the step-growth leads to a greatly increased network homogeneity as the formation of microgels is avoided and on the other hand gelation takes place at much higher conversions. The conversion DC_{gel} at which gelation occurs can be

calculated by the following expression [47]:

$$DC_{gel} = \frac{1}{\sqrt{r(f_1-1)(f_2-1)}} \tag{2.31}$$

where f_1 and f_2 are the average functionalities of the thiol and ene monomers, respectively. The stoichiometric imbalance $r \leq 1$ is given by

$$r = \frac{n_1 f_1}{n_2 f_2}, \tag{2.32}$$

where n_1 and n_2 are the number of thiol and ene molecules, respectively. For example, if both monomers have functionality three and are mixed stoichiometrically (i.e. $r = 1$) the gel-point will occur at 50 % conversion. The delayed gelation also leads to decreased stress of the final polymer since a large part of shrinkage can be accomodated by liquid flow.

Figure 2.11 also illustrates the differences in cross-link density of the two polymerization mechanisms. Monofunctional monomers lead to long chains in a chain-growth mechanism, whereas in a step-growth reaction only single adducts are created. Similarly, difunctional monomers proceeding via chain-growth already lead to cross-linked polymers but yield linear polymers in the case of step-growth. Only monomers with an average functionality greater than two lead to cross-linked polymers using a step-growth mechanism. The reason for this behavior is that in a thiol-ene reaction each ene forms a single bond with a thiol group whereas in the polymerization of acrylates each functional group is attached to two other acrylates [68]. Reddy et al. developed a general model describing the network development of ternary thiol-vinyl-vinyl systems exhibiting a mixed step-chain-growth polymerization that also contains thiol-acrylate and thiol-ene systems [72].

This leads to another important difference between thiol-enes and acrylates. The shrinkage factor (the amount of shrinkage associated to each functional group) is significantly reduced for thiol-enes ($S = 12 - 15\ cm^3 mol^{-1}$ [61][73]) compared to acrylates ($S = 24\ cm^3 mol^{-1}$). Therefore, thiol-enes have a reduced overall shrinkage which is one of their biggest advantages especially regarding the NIL process because pattern fidelity is decreased by shrinkage as already discussed. Furthermore, thiol-enes exhibit a second mechanism to reduce the replication error during imprinting: they can accomodate a large part of the shrinkage by liquid flow due to their delayed gel-point [74], thereby reducing the residual layer thickness as depicted on the right of Figure 2.9. This is only possible if the initial layer thickness is thick enough. Acrylates are not able to accomodate shrinkage in this way due to their early gelation [74].

Another benefit of thiol-enes is their reduced oxygen-inhibition. As shown in Figure 2.12 carbon radicals that are created during the polymerization react with oxygen, leading to peroxy radicals. These radicals are relatively stable and in the case of acrylate homopolymerization are not able to react with another carbon-carbon double bond and therefore, the polymerization is inhibited. However, the peroxy radical is able to abstract a hydrogen from a thiol and therefore, the thiol-ene reaction can proceed further. Oxygen inhibition is, however, only important until all of the dissolved oxygen is consumed and afterwards the reaction can proceed undisturbed. Oxygen diffusion from air into the sample is slow compared to usual polymerization reactions and therefore only plays a role at thin surface layers ($0.1 - 10\ \mu m$) [41]. When polymerizing thick acrylates in the presence of oxygen only the surface will stay liquid but the bulk is cured.

A major drawback of thiol-enes is their limited shelf-life stability, i.e. they react even in the absence of photinitiators or light and gelation usually occurs in time periods ranging from

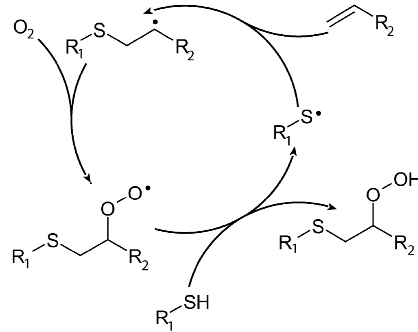

Figure 2.12: Reduced oxygen inhibition of thiol-ene polymerization: the peroxy radical that is formed by the reaction of a carbon radical with oxygen cannot react with another double bond but is sufficiently reactive to abstract a hydrogen from a thiol group. Picture taken from [68]

a few minutes to several weeks. One way to cirumvent this is the use of stabilizers that capture radicals [75][76]. Secondary thiol monomers have been shown to increase the shelf-life stability as well without decreasing the polymerization rate severely [77]. Furthermore, storage at reduced temperature significantly increases the lifetime. Anyway, their limited stability is not a severe hindrance as one could simply store the thiol and ene components separately and only mix them immediately before their usage.

2.2.6 Mechanical properties of polymers

As discussed in Section 2 the mechanical properties of the polymers play an important role in the NIL process. To understand how to adjust the mechanical properties the relationship between molecular structure and mechanical properties is discussed based on the the work of Heijboer [78]. The behavior of polymers which are subjected to a tensile force is illustrated in Figure 2.13 showing the stress σ in dependance of the strain ε during loading. At the beginning the polymer is deformed elastically which corresponds to the linear part of the curve. If the load is released in this regime the sample will fully recover its orignal shape. After the yield point that characterizes the end of the elastic part plastic deformation sets in which can not be recovered after unloading. Further increasing the stress eventually leads to breakage. Mechanical behavior of polymers is mainly described by two factors, stiffness and strength. The stiffness is characterized by the elastic modulus E of the sample which is given by the slope of the linear part of the stress-strain curve.

$$E = \frac{\sigma}{\varepsilon} \tag{2.33}$$

The yield strength is the stress at the yield point, describing the maximum force per cross-sectional area that can be applied to the sample that allows full recovery after unloading. This is a very important quantity for the NIL process because the yield strength of the cured imprint resin has to be at least as high as the stresses induced during demolding to ensure defect-free demolding. The ultimate tensile strength is the maximum stress that can be applied to the sample. The toughness of the material describes the total amount of energy that can be applied to it before breakage and is given by the area under the stress-strain curve. The upper curve in Figure 2.13 corresponds to glassy polymers with high modulus and stiffness

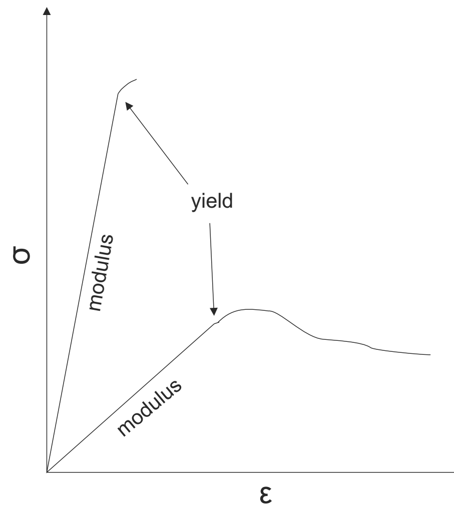

Figure 2.13: Stress σ in dependance of strain ε of polymers subjected to tensile forces. The upper and lower curves correspond to polymers in the glassy and in the rubber state, respectively. The elastic modulus is given by the slope of the linear part of the stress-strain curve. The end of the linear part defines the yield point and break happens at the end of the curves. Picture modified from [79].

that break after small elongations but can withstand high forces. They break immediately after the elastic regime due to their brittle nature. The other curve corresponds to polymers in the rubber state which show a low stiffness and higher elongations.

The general temperature dependence of the modulus of polymers is shown in Figure 2.14. There are regions of high (glassy state) and low (rubbery state) modulus at low and high temperatures, respectively, the transition between the two occuring at the glass transition temperature T_g. For non cross-linked polymers also a flow region exists. When heated above the glass transition temperature the modulus can drop by a factor of about one thousand for lightly cross-linked polymers. For polymers in the glassy state Fakirov et al. [80] and Bartolomeo et al. [81] found a linear relationship between T_g and hardness ($H \propto T_g$). Hardness determines the resistance to local deformations at the surface and can be measured by indentation experiments. It is correlated to the yield strength of a material [80].

This means a high glass-transition temperature is beneficial for both hardness and modulus. The glass transition temperature describes the temperature at which small chain segments become able to move making the polymer appear less stiff. One way to achieve high glass transition temperatures is to generate polymers with high cross-link densities as this hinders chain movement. The increase of T_g with the cross-link density is illustrated in Figure 2.14. This also causes the modulus in the rubber region to increase. In fact, there is a direct proportionality between the modulus in the rubber region and the cross-link density ($E_R \propto \nu$) [82]. However, a high cross-link density can only be realized by high reactive group concentrations which implies high polymerization shrinkage as discussed in Section 2.2.4. Fortunately, the glass transition temperature is not only determined by the cross-link density but also by the molecular geometry. Long or flexible chains between succesive cross-links lead to low T_g because they make chain movement easy, but short or stiff chains lead to high T_g (incorporating ring structures is one possibilty). Therefore, high T_g and yet low shrinkage polymers can be

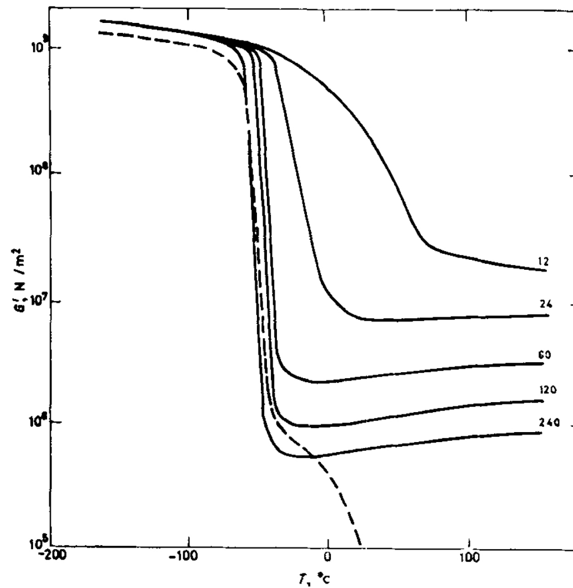

Figure 2.14: Temperature dependence of modulus for polymers with different cross-link densities. The numbers indicate the numbers of atoms between successive cross-links. So small numbers correspond to high cross-link densities and vice versa. The dashed line corresponds to a non-cross-linked polymer. Picture taken from [78].

synthesized [62]. Because of its influence on both the cross-link density and the glass transition temperature, the molecular structure offers a huge potential for tuning the mechanical properties.

Hill presented simple equations for calculating the cross-link density of networks [83] formed by step-growth. The cross-link density ν is defined as the number of elastically active network chains per unit volume, which are chains connecting junctions (i.e. atoms having three or more paths leading to the infinite network [84]). Examples for elastically inactive network chains would be dangling bonds, loops and unreacted monomers. If complete conversion is assumed the cross-link density is given by

$$\nu = \frac{1}{2} \frac{\sum_{i,f \geq 3} f_i \chi_i}{\sum_i M_i \chi_i} \rho \tag{2.34}$$

which is about one half of the reactive group concentration (see Equation 2.30). However, ρ in this case denotes the polymer and not the monomer density. Note that the sum in the numerator only considers monomers with functionality greater than two because difunctional monomers do not form junctions (in other words: using difunctional thiol-enes only, cross-link density would be zero because they only lead to formation of chains as stated before). This Equation does not apply to acrylates. As explained in the previous section for an ideal acrylate network the cross-link density would be twice as high. However, due to the inhomogeneity of the network and the limited final conversion the value is decreased. Calculating the cross-link density of acrylates has been discussed (among others) by Miller et al. [84] but is rather complex and beyond the scope of this thesis.

3 Experimental

3.1 Materials

The molecular structures of the acrylates, photoinitiators and thiol-enes used in the present work are depicted in Figure 3.1, Figure 3.2 and Figure 3.3, respectively. In Tables 3.1 and 3.2 the molar weight, density, viscosity and reactive group concentration of acrylates, thiols and enes are listed. If not stated otherwise all resins contain 97 $wt\%$ of the monomer mixture and 3 $wt\%$ KL200 as photoinitiator. For all NIL experiments where easy separation of mold and resin is crucial 0.25 $wt\%$ of a perfluoropolyether methacrylate (MD700) is added to reduce the surface energy.

Table 3.1: Molar weight M, density ρ and viscosity η of acrylate monomers used in this work taken from data sheets. The reactive group concentration $[RG]$ is calculated according to Equation 2.29.

monomer	M $[g/mol]$	ρ $[g/cm^3]$	η $[mPas]$	$[RG]$ $[mmol/cm^3]$
HDDA	226	1.02	9	9
TMPTA	296	1.1	120	11
$TMP(EO)_9TA$	692	1.11	130	4.8
$TMP(EO)_{15}TA$	956	1.11	150	3.5
PETTA	352	1.19	600-1000	13.5
DPHA	525	1.12	5000-9000	13.2

Table 3.2: Molar weight M, density ρ and viscosity η of thiol and ene monomers used in this work taken from data sheets. The reactive group concentration $[RG]$ is calculated according to Equation 2.29

monomer	M $[g/mol]$	ρ $[g/cm^3]$	η $[mPas]$	$[RG]$ $[mmol/cm^3]$
GDMP	238.3	1.19	10	10
TMPMP	398.6	1.21	150	9.1
Karenz	544.8	1.2	1200	8.8
TEMPIC	525.6	1.333	8000	7.6
TVCH	162	0.836	1.2	15.5
CHDMDVE	196	0.919	4.41	9.4
TAC	249	1.234 ($25°C$)	13 ($30°C$)	14.9
TAICROS	249	1.152 ($30°C$)	90 ($30°C$)	13.9

Hexandioldiacrylat (HDDA), Trimethylolpropantriacrylat (TMPTA) and the urethane acrylates Ebecryl8210 and Ebecryl4820 were donated by Allnex. 9-ethoxylated trimethylolpropanetriacrylate (TMPEO_9TA, trade name Miramer3190), 15-ethoxylated trimethylolpropanetriacrylate (TMPEO_{15}TA, trade name Miramer3150), pentaerythritoltetraacrylat (PETTA, trade name M420), dipentaerythritolhexaaacrylat (DPHA, trade name M600) were donated by Miwon. Cyclohexanedimethanoldivinyl ether (CHDMDVE) was donated by BASF. Glykoldimercaptopropionat (GDMP), tri- methylolpropantrimercaptopropionat (TMPMP), Trismercaptopropionyloxyethylisocyanurate (TEMPIC) were donated by Bruno Bock. Pentrythrioltetrakismercaptobutanoate (Karenz) was donated by Showa Denko. Trivinylcyclohexane (TVCH), triallylcyanurate (TAC) and triallyltriazinetrione (TATATO, trade name TAICROS) were donated by Evonik. Hydroxymethylphenylpropanone (trade name KL200) was donated by Lamberdi. Ethyltrimethylbenzoylphenylphosphinate (trade name TPO-L) and bistrimethylbenzoylphenylphosphineoxide (trade name I819) were donated by BASF. Dimethoxyphenylacetophenone (DMPA, trade name BDK) and Diethylthioxanthone (DETX) were donated by Rahn. The perfluoropolyether(PFPE)-urethane dimethacrylates Fluorolink MD700 and MD40 were donated by Solvay. The PFPE-urethane acrylate LR2000 was donated by Miwon. The structures of the PFPE resins are not completely known due to proprietary reasons but are similar to the one indicated in Figure 3.1 for MD700. Optool DSX was donated by Daikin Industries. Tridecafluorooctylphosphonic acid was donated by Specific Polymers. All substances are used as received without further purification.

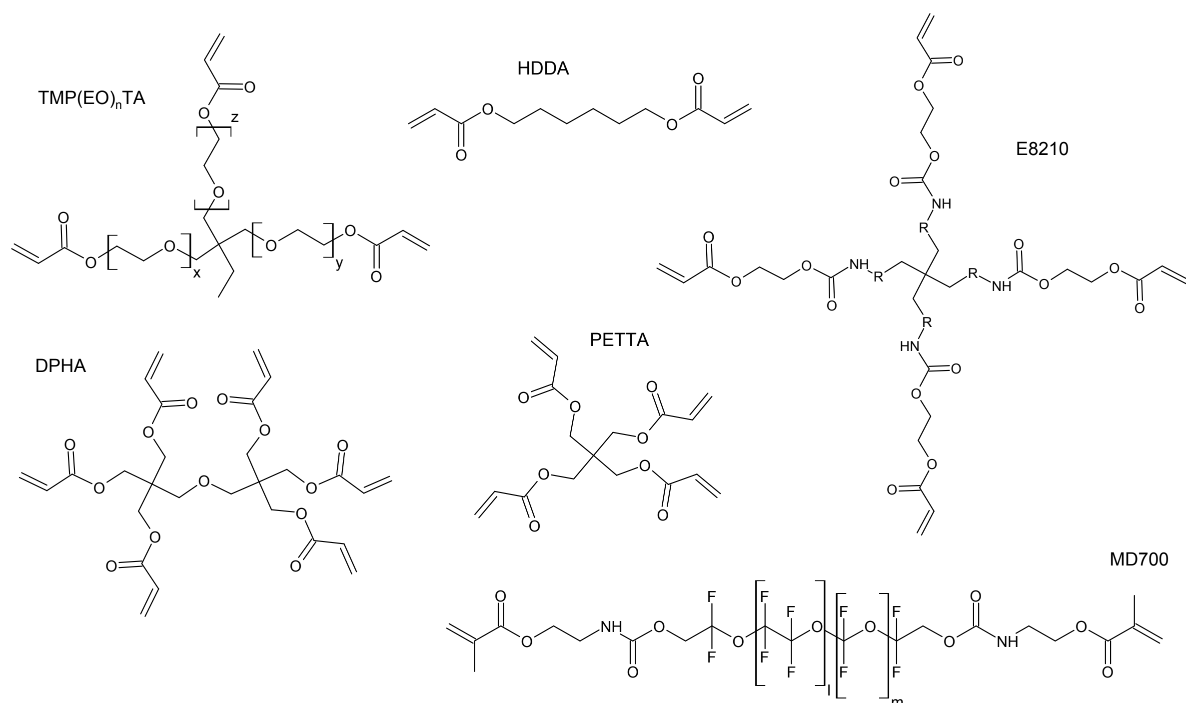

Figure 3.1: Molecular structures of acrylates used in this work (n=x+y+z, TMPTA=TMP(EO)$_0$TA).

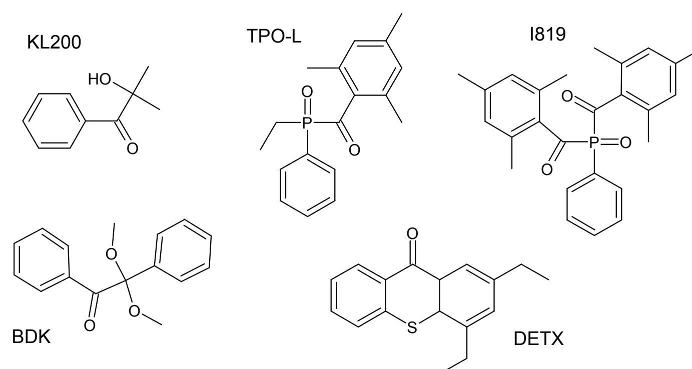

Figure 3.2: Molecular structures of photoinitiators used in this work.

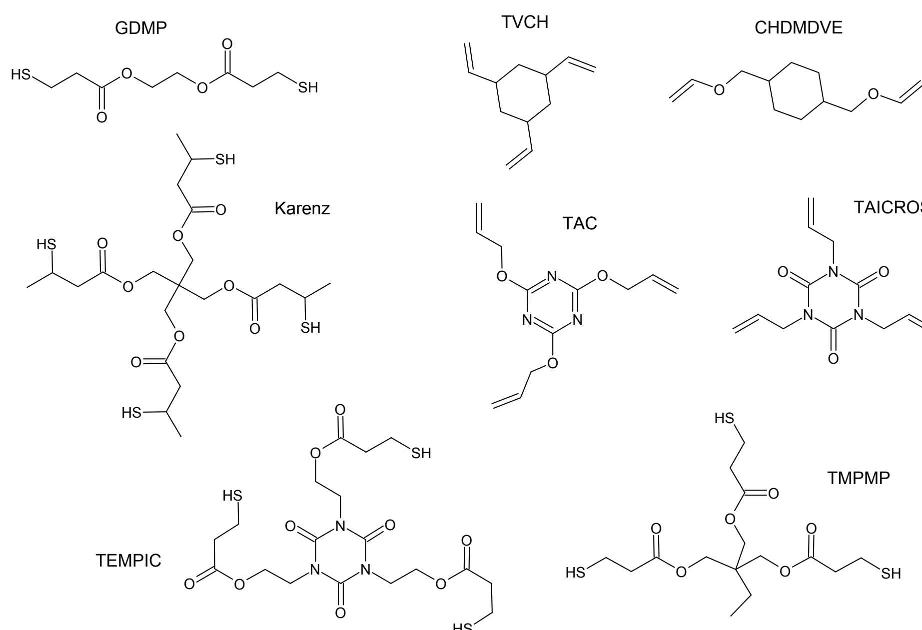

Figure 3.3: Molecular structures of thiols and enes used in this work.

3.2 Methodology

3.2.1 Surface energy - contact angle measurement

To measure the surface energy contact angle measurement is employed which is reviewed, for example in [85][86] which the following discussion is based on. The measurements are evaluated according to the Owens-Wendt-Rabel-Kaelble (OWRK) method. When a drop of a liquid is deposited on a solid surface there is a contact angle θ between the two phases. According to the well known Young equation (Equation 3.1) it depends on the surface energy of the liquid and solid, γ_l and γ_s, respectively, as well as on the energy associated with their interface γ_{sl}:

$$\gamma_s = \gamma_{sl} + \gamma_l cos\theta \tag{3.1}$$

With this equation the surface energy of the solid can be calculated when using a liquid with known surface energy and measuring the contact angle. However, γ_{sl} remains unknown, which is why additional assumptions have to be made. The basic idea is that it depends on the surface energies of the liquid and the solid and can, therefore, be calculated from them. Different relations between these three quantities have been suggested in literature, the first being the Berthelot hypothesis (Equation 2.7). Together with the Dupre equation,

$$w_{adh} = \gamma_s + \gamma_l - \gamma_{sl}, \tag{3.2}$$

which represents the fact that the energy necessary to separate the liquid from the solid is the energy required to create the two new surface minus the interfacial energy which is released, the Berthelot hypothesis yields the following form

$$\gamma_{sl} = \gamma_s + \gamma_l - 2\sqrt{\gamma_s \gamma_l}, \tag{3.3}$$

which allows to calculate the surface energy of the solid according to Equation 3.1. Owens and Wendt extended this relation by considering that the interactions between the solid and the liquid comprise dispersive and polar interactions [87]. The dispersive component is due to London forces (i.e. spontaneous induced dipole interactions) while the polar component comprises the remaining van der Waals forces (Keesom and Debye) and hydrogen bonds, for example. Therefore, they used the following relation:

$$\gamma_{sl} = \gamma_s + \gamma_l - 2\sqrt{\gamma_s^d \gamma_l^d} - 2\sqrt{\gamma_s^p \gamma_l^p}, \tag{3.4}$$

where γ_s^d, γ_s^p, γ_l^d and γ_l^p are the dispersive and polar components of the solid and liquid surface energy, respectively. Because there are now two unknown quantities, γ_s^d and γ_s^p, the contact angle has to be measured with two liquids of known surface energy which yields a system of two equations with two unknowns.

In the present work, a Krüss DSA100 drop shape analyzer is used to measure contact angles and to calculate surface energies. The system consists of a sample stage that is illuminated by a lamp and recorded by a video camera and a dosing system to deposit the liquid drops on the solid sample. The setup is controlled with the proprietary software DSA4 which also allows to evaluate the measurements automatically. To measure the surface energy of a sample the needle through which the liquid is applied is filled such that there is a pendant drop hanging from it. The sample stage is then driven upwards until it touches the pendant drop and slowly driven downwards again to pull of the drop from the needle. The shape and baseline of the drop resting on the solid surface is then analyzed by the software which subsequently extracts the contact angle. This is performed three times with each of the two liquids and from the average contact angles the surface energy is calculated with the OWRK method described above. Water ($\gamma_W^d = 21.8\ mJ/m^2$ and $\gamma_W^p = 51.0\ mJ/m^2$) and diodomethane ($\gamma_D^d = 48.5\ mJ/m^2$ and $\gamma_D^p = 2.3\ mJ/m^2$) are employed as measuring liquids.

3.2.2 Viscosity - rheometry

Viscosity is a measure of the resistance of fluids against flow. Low-viscosity fluids flow faster than highly viscous fluids when the same force is applied. When two parallel flat layers of a fluid with area A, separated by a distance dx, are moving laterally with different velocities v_1 and v_2 a force F is necessary to maintain the difference in speed because the internal friction

of the fluid would slow down the movement as depicted in Figure 3.4 [88]. This force is related to the velocity gradient dv/dx via the following equation originally given by Newton.

$$\frac{F}{A} = \eta \frac{dv}{dx} \tag{3.5}$$

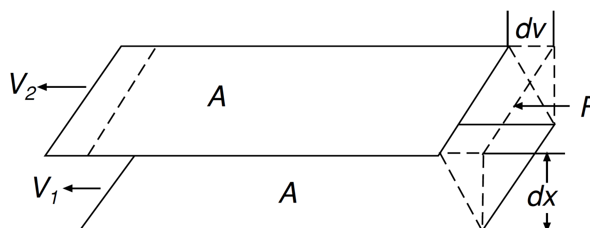

Figure 3.4: When two parallel flat layers with area A of a fluid, separated by a distance dx, are moving laterally with different velocities v_1 and v_2 a force F is necessary to maintain the difference in speed due to the internal friction of the fluid. Picture taken from [88].

The force per area is also known as shear stress $\tau = F/A$ and the velocity gradient as shear rate $\dot{\gamma} = dv/dx$. From the equation given above it is evident that the viscosity of a fluid can be determined by subjecting it to a defined shear rate and measuring the shear stress.

The Brookfield DV-III Ultra Rheometer which is employed in the present work measures the torque necessary to rotate a spindle immersed in the test liquid [89]. The spindle of defined geometry (cylinder capped with a cone) is placed inside a coaxial cylindrical container and driven by a motor through a spring. The viscous drag of the fluid acting on the spindle is measured by the spring deflection detected by a rotary transducer. Since viscosities are usually temperature-dependent the resin is maintained at $21°C$ for all measurements with a circulating constant-temperature water bath. To measure the viscosity of a fluid it is filled into the container with a piston-driven micropipette taking care that no air bubbles are introduced into the liquid which would cause wrong values. The amount of liquid is chosen so that the spindle is immersed up to the middle of its shaft as recommended in the manual. The spindle is then immersed in the liquid and the the container is mounted onto the Rheometer and connected to a thermometer. Then the measurement is conducted using the proprietary software Rheocalc.

3.2.3 Degree of conversion - Fourier-Transform Infrared Spectroscopy

Theoretical background

To investigate the conversion of polymerized resins attenuated total reflectance Fourier transform infrared spectroscopy (ATR-FTIR) is employed. FTIR is reviewed for example in [90],[91] and [92] which the following discussion is based on. This technique is based on the measurement of the spectral (i.e. wavelength-dependent) absorption of infrared light penetrating into the sample[93]. To achieve this the sample is brought in contact with an optical denser material, the internal reflection element (IRE), as depticted in Figure 3.5. Infrared light is then introduced into the IRE under a certain angle such that total internal reflection occurs at the interface to the sample. Finally it is collected by a detector. Despite total internal reflection

the electric field amplitude decays exponentially with distance from the interface which means that this evanescent wave penetrates a short distance into the sample and may be absorbed. If absorption takes place the reflected wave gets attenuated (hence the name ATR) and thereby an absorption spectrum can be obtained.

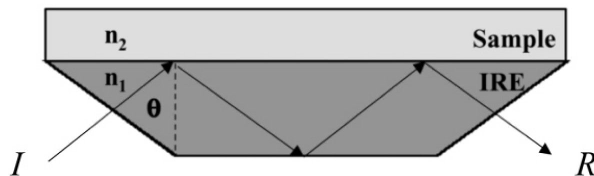

Figure 3.5: Schematic illustration of the internal total reflection occuring at the interface between sample and IRE. Picture taken from [93].

The physical origin of the infrared spectrum of a molecule are electronic excitations at energies that correspond to the vibration of specific atoms or atom groups connected by chemical bonds. Considering the model of a harmonic oscillator the frequency of a specific vibration depends on the mass of the molecular fragments involved and the force constant, i.e. strength of the covalent bond. Hence, from the presence or absence of certain infrared peaks conclusions can be drawn on the composition of the molecule. It should be mentioned that not every molecular vibration needs to be represented in the spectrum because for to be infrared active a change in dipole moment is neccessary during the vibration. Furthermore, a quantitative analysis is possible, since "the area under the infrared peak at a given wavelength is directly proportional to the number of chemical bonds excited at that wavelength" (Kane et al. [94]) as the measured absorbance a is given by

$$a = -log\frac{I}{I_0} = \varepsilon cd, \tag{3.6}$$

where I and I_0 are the incident and reflected light intensities, respectively, ε is the molar absorptivity, c the concentration and d the penetration depth of the evanescent wave. Therefore, the degree of conversion DC can be measured by monitoring the area of the corresponding infrared peak with respect to time. Then the following expression holds:

$$DC(t) = 1 - \frac{A_{norm}(t)}{A_{norm}(t=0)}, \tag{3.7}$$

where $A_{norm}(t)$ is the area of the absorption maximum A_{DB} normalized to the area of an internal reference peak A_{ref}:

$$A_{norm}(t) = \frac{A_{DB}(t)}{A_{ref}(t)} \tag{3.8}$$

Normalization is neccessary since the area of the reference peak which should be unaffected by polymerization does not stay constant. Explanations might be densification (shrinkage) of the sample leading to an increased concentration of the respective molecule fragments [95], increase of the penetration depth due to a higher refractive index and nonlinearities of the measuring equipment.

A typical infrared spectrum is depicted in Figure 3.6. As common the frequency is given in units of wavenumbers (cm^{-1}). In general, an infrared spectrum can be divided into several

regions [92]. The vibrations between $4000-2500\ cm^{-1}$ are due to O-H, N-H or C-H stretching. Triple-bond stretching absorptions are found in the $2500-2000\ cm^{-1}$ region. The bands between $2000-1500\ cm^{-1}$ are associated with double bond stretching, e.g. C=C or C=O stretching. The region between $1500-500\ cm^{-1}$ is referred to as fingerprint region because it is different for every molecule and the position of peaks corresponding to certain vibrations can shift over large ranges even for rather similar molecules. Specific absorption maxima can be assigned to certain vibrations using literature references [90][91]. The inset shows the decreasing area of the carbon-carbon double bond peak with ongoing conversion. Peaks corresponding to double bonds can be found around 810 cm^{-1} (C=C-H out of plane bending), 1630 cm^{-1} (C=C stretching) and 3050 cm^{-1} (C=C-H stretching). The peak at 2575 cm^{-1} corresponding to the S-H stretching is not very pronounced which is why thiol conversion could not be measured accurately. The carbon-oxygen (C=O stretching) peak at about 1730 cm^{-1} is used as internal reference.

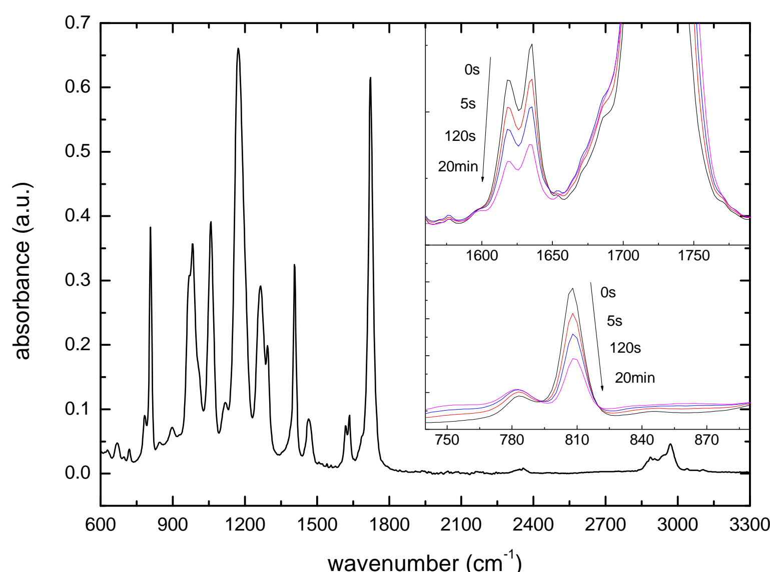

Figure 3.6: Infrared spectrum of TMPTA. The insets show the peaks associated to carbon-carbon double bonds decreasing with exposure to UV light.

Experimental procedure

To measure the conversion of a liquid resin, one drop of it is deposited on the diamond (IRE) with a glass Pasteur pipette. Spectra are collected every 1.5 s (wich is the highest rate possible) with the Tensor 27 spectrometer of Bruker Optics using the proprietary software OPUS. The spectral resolution is 4 cm^{-1}. The integration time for each spectrum is 1 s and the background measured at the beginning is automatically subtracted. Exposure is started manually immediately after the first spectrum is collected. To obtain the area of the peaks of interest the data are processed using the Origin 8Pro software. Since usually several peaks are overlapping a deconvolution technique is employed and the data are fitted according to

an appropriate number of Gaussian functions after a linear baseline is substracted. Since this procedure is time consuming not all of the spectra are evaluated (during 10 *min* about 400 spectra are collected) but only until a reasonable number of data points is obtained. The degree of conversion can then be calculated using Equations 3.7 and 3.8.

The experimental data are fitted according to the following equation:

$$DC(t) = c\left(1 - exp\left(-\frac{t - t_0}{\tau}\right)^{\beta}\right), \tag{3.9}$$

which will be explained in the following. From Equations 2.20-2.25 an expression for the degree of conversion DC can be derived [59]. In a steady-state assumption the number of radicals remains constant throughout the polymerization, hence,

$$R_i + R_t = 0. \tag{3.10}$$

Substituting Equations 2.20 and 2.23 into this yields

$$[M^{\bullet}] = \left(\frac{R_i}{2k_t}\right)^{0.5} \tag{3.11}$$

With this Equation 2.25 becomes (for the sake of simplicity a time constant τ may be defined)

$$-\frac{d[M]}{dt} = k_p[M]\left(\frac{R_i}{2k_t}\right)^{0.5} = \frac{[M]}{\tau} \tag{3.12}$$

which can be solved by integration by separation of variables:

$$\int \frac{d[M]}{[M]} = \int -\frac{1}{\tau}dt \tag{3.13}$$

$$ln\frac{[M](t)}{[M](0)} = -\frac{t}{\tau} \tag{3.14}$$

$$\frac{[M](t)}{[M](0)} = exp\left(-\frac{t}{\tau}\right) \tag{3.15}$$

Substituting this into Equation 2.26 gives the time-dependence of the degree of conversion.

$$DC(t) = 1 - exp\left(-\frac{t}{\tau}\right) \tag{3.16}$$

This expression is valid when a steady-state assumption is made (Equation 3.10) and shrinkage is proportional to the degree of conversion. However, this is not true for the polymerization of multifunctional acrlyates as discussed in Section 2.2.3. Many relaxation effects occuring in vitrified polymers can be described by the Kohlrausch–Williams–Watts function (Equation 3.17) in an empirical way where the parameter β accounts for the width of the relaxation spectrum [49][59].

$$DC(t) = 1 - exp\left(-\frac{t}{\tau}\right)^{\beta} \tag{3.17}$$

This equation is further modified to account for two additional effects. The parameter c in Equation 3.9 is introduced to account for conversions below 100 %. Furthermore, it has to be considered that the UV illumination is started manually and that the UV-lamp needs a small amount of time to reach its full intensity after being started which means that the polymerizations do not start exactly at $t = 0$. This is why the parameter t_0 is introduced.

3.2.4 Shrinkage - hydrostatic balance

As mentioned before, polymerization shrinkage has the potential to decrease the replication fidelity of NIL and thiol-enes are candidates to reduce this effect. To better understand the relationship of molecular structure and final shrinkage a series of molecules has been investigated regarding shrinkage. Several methods for measuring polymerization shrinkage have been used in literature, e.g. linear displacement in narrow tubes [61], laser displacement sensors [96] [63] [97], optical methods (drop shape analysis) [98], different kinds of water displacement methods (water dilatometer [99], pycnometry [100], hydrostatic weighing [62]) and a device called a linometer [101].

In the present work hydrostatic weighing is used to determine the polymer density for several reasons: simple and low-cost equipment and yet high precision even when using only small amounts of substances (in the order $0.1 - 0.5$ g), easy and fast measurement and evaluation, no special requirements regarding the sample shape and the ability of measuring the total (not only post-gel) shrinkage. Compared to more advanced techniques it is not possible to simultaneously measure shrinkage and conversion. The principle of a hydrostatic balance is depicted in Figure 3.7 [102]. When a container of a certain volume is suspended in water the balance will show a weight increase w that corresponds to the weight of the water displaced. This can be understood when imagining an empty container that is immersed in water. A force, called the buoyancy force, has to be applied to push it beneath the water surface and this force is detected by the balance. According to Archimede's principle this force equals the weight of the displaced water. From this the volume of the displaced water (which equals the container volume) can be easily calculated by $V = w/\rho_{water}$ if the density is known. If the sample is additionally weighed in air to determine its mass m the density of the sample can be calculated by $\rho = m/V$.

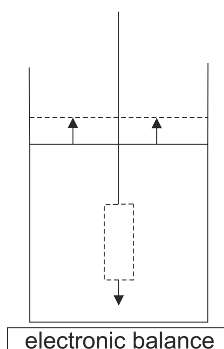

Figure 3.7: When a container is suspended in water the buoyancy force is detected by the electronic balance. According to Archimede's principle this force equals the weight of the displaced water from which its volume can be easily calculated. Picture modified from [102].

Once the monomer density ρ_m and the polymer density ρ_p are known shrinkage can be calculated according to Equation 2.27 considering the definition of density $\rho = mV^{-1}$:

$$\frac{\Delta V}{V} = 1 - \frac{V_p}{V_m} = 1 - \frac{\rho_m}{\rho_p} \tag{3.18}$$

The monomer density was taken from data sheets and if not available measured by pycnometry.

In practice, the pycnometer is weighed empty and filled with water which together with the known water density yields its volume. Afterwards it is weighed containing the liquid monomer - hence, mass and volume of the monomer are known and the density can be calculated. Filling is performed with a piston-driven air displacement micropipette taking care not to produce any air bubbles and the pycnometer is cleaned with cleanroom wipes before to ensure only monomer inside the pycnometer is weighed. Before each measurement the pycnometer is carefully cleaned with acetone and isopropanol to remove any residual monomer. All measurements are performed at room temperature.

To measure the polymer density samples are prepared by filling some liquid in a form prepared from aluminium foil which allows easy separation after curing. The samples are flat to achieve a uniform light intensity throughout the sample. Polymerization is performed by exposure to UV light ($I = 0.5\ mWcm^{-2}$, $\lambda = 365\ nm$) for 20 min to ensure complete conversion. Afterwards, the samples are separated from the aluminium foil and weighed dry to give their mass and weighed using the hydrostatic balance to give their volume. Hydrostatic weighing was performed over a time period of 60 s and repeated without sample for the same duration to determine and correct water evaporation.

3.2.5 Mechanical properties - microindentation

Theoretical background

Hardness H and Youngs modulus E are determined by microindentation and analyzed using the Oliver-Pharr method which is described in the following [103][104]. An extensive discussion of indentation is given in [105]. During the experiment an indenter with a given geometry is pressed into the solid sample while continuously measuring load P and displacement h. A schematic depiction of the measured data is shown in Figure 3.8. During loading the solid is deformed both elastically and plastically, whereas it is assumed that during unloading only the elastic part recovers and a permanent indent is left in the solid. If the solid were purely elastic, the loading and unloading part would coincide.

There are three quantities that are obtained from the measurement and from which hardness and modulus can be calculated: the maximum load P_{max}, the maximum displacement h_{max} and the elastic unloading stiffness $S = dP/dh$, which is the slope of the initial part of the unloading curve. Using the Oliver-Pharr method the unloading curves are approximated by a power law relation

$$P = \alpha(h - h_f)^m, \tag{3.19}$$

where α and m are fitting constants. This describes the experimental data much better, than the previously used linear approximation. Hardness is defined as the maximum load divided by the projected area of contact A.

$$H := \frac{P_{max}}{A} \tag{3.20}$$

Originally A was measured optically with a microscope. However, if the geometry of the indenter is known the contact area A can be calculated from the the displacement h as well which is the approach of the Oliver-Pharr method. This has the advantage of enabling to measure indents even in the submicron range and avoiding the time-consuming optical observations. To account for nonidealities of the indenter geometry it has to be carefully calibrated before the actual measurement. The elastic modulus E is related to the unloading stiffness S and the

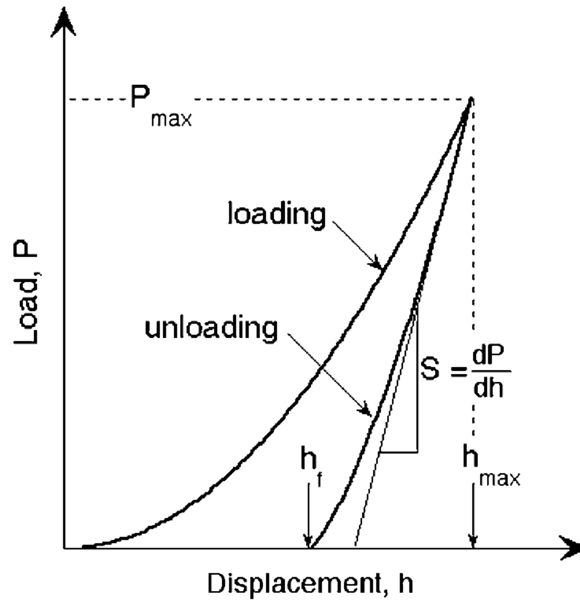

Figure 3.8: Schematic illustration of a typical force-displacement curve of an indentation experiment. Picture taken from [103].

projected contact area A via

$$S = \beta \frac{2}{\sqrt{\pi}} E^* \sqrt{A} \tag{3.21}$$

where β is a constant that accounts for nonidealities (e.g. lack of axial symmetry of the indenter) and the effective (also called reduced) modulus E^* is used to account for the displacement of the indenter

$$\frac{1}{E^*} = \frac{1-\nu^2}{E} + \frac{1-\nu_i^2}{E_i} \tag{3.22}$$

where E (E_i) and ν (ν_i) are the elastic modulus and Poisson's ratio of the sample (indenter).

Experimental procedure

All the measurements were conducted with an Anton Paar microscratcher and analysed with the proprietary software Indentation 6.2.8. To get reproducible samples thin films are prepared on microscopy slides by Meyer rod coating. The low thickness also helps to achieve uniform light intensity and network properties throughout the samples. Three drops of the monomer solution are deposited onto the glass slides with a glass Pasteur pipette and a Meyer rod is slowly pulled over the slide manually which results in thin films with a uniform thickness of 100 μm which is confirmed by an electronic micrometer gauge. Then the samples are irradiated by UV light (0.5 mW/cm^2,$\lambda = 365$ nm) for 20 minutes to ensure complete curing. The indentation is done with a loading rate of 50 mN/min until a maximum load of 50 mN is reached which is held for 30 s before unloading with a rate of 50 mN/min. The holding time is introduced to decrease the influence of creep. For every sample the measurement was performed three times, the indentations having a separation of 100 μm and the values presented in Section 3.3.5 represent the average of the three measurements.

3.2.6 Pattern replication by nanoimprint lithography

3.2.6.1 Batch process

To replicate a mold pattern in a batch process a sufficient amount of liquid (depending on the area of the pattern) is deposited onto the mold with a glass Pasteur pipette and covered with a PET foil. The resin spreads due to capillary forces which is more versatile for low-viscosity resins. After the resin covered the desired area it is exposed to UV-light for a specified amount of time using a Biostep USDT-20ML-8R UV-lamp. Afterwards, the PET substrate which the resin adheres to is separated manually from the mold in a peeling fashion as depicted in Figure 2.4. Figure 3.9 shows the spectrum of the UV-light source used during the batch processes in the present work. The spectrum consists of one peak centered at $\lambda = 365\ nm$. The light intensity obtained by numerical integration is $0.5\ mW/cm^2$. The transmission spectrum of PET is depicted as well as the UV-light is transmitted through the PET substrate. As discussed in Section 2.2.2 the rate of initiation, hence the polymerization rate depends on the absorption of the photoinitiator as well. The extinction coefficient of KL200 is $61.5\ ml/gcm$ at $\lambda = 365\ nm$ ($567\ ml/gcm$ at $\lambda = 313\ nm$). The spectrum as well as the absolute intensity of the UV lamp was measured by placing it in front of an integrating sphere which is connected to a CAS 140CT spectrometer by an optical fiber waveguide (whole system from Instrument Systems).

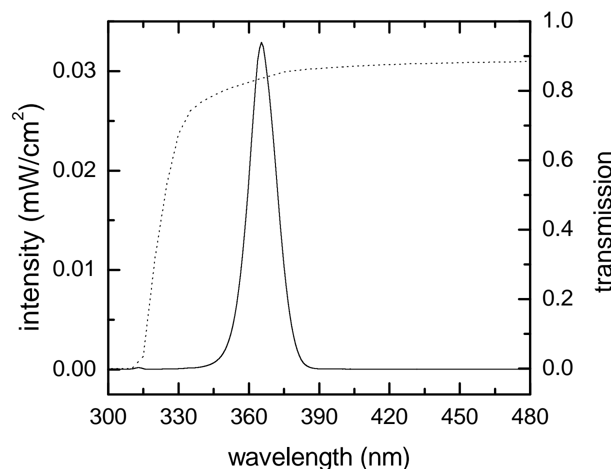

Figure 3.9: Spectrum of the UV-light source used during the batch processes (line). The dotted line shows the transmission spectrum of PET.

3.2.6.2 Residue-free imprinting

To obtain imprints with near-zero residual layer thickness micromolding in capillaries (MIMIC) is used which is described in [106] and illustrated schematically in Figure 3.10. First, the mold is pressed onto the PET substrate using clamps. Then, liquid resin is deposited in direct vicinity to the mold with a glass Pasteur pipette and subsequently fills the mold cavities driven by capillary forces. After UV-light exposure, the mold is removed and the imprinted features remain on the substrate without residual layer.

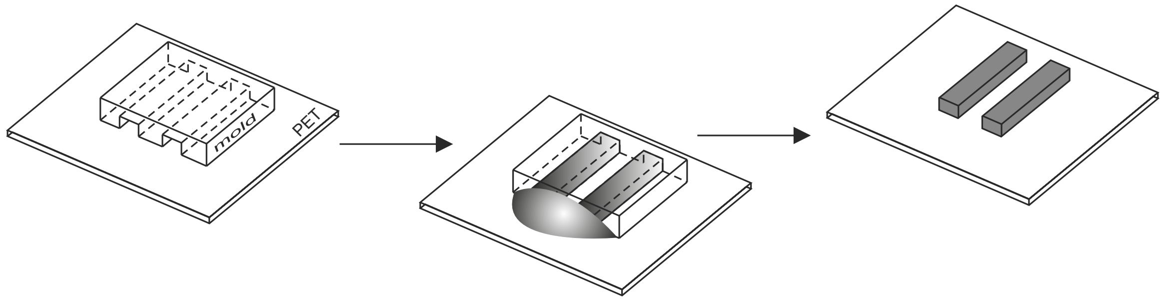

Figure 3.10: Schematic illustration of the process to obtain replicated structures without residual layer.

3.2.6.3 Roll-to-roll process

To replicate a pattern of a silicon master in a roll-to-roll process, first of all a polymer stamp is fabricated in a batch process from the master. The polymer stamp is then attached to the imprint roller of the R2R machine with double-sided adhesive tape to be illuminated with the high-intensity UV lamp. This was done for ten minutes while the cylinder was rotating at a speed of 0.5 m/min to ensure complete conversion of the polymer stamp. Afterwards, to perform the actual R2R impring, the PET substrate is coated with the liquid imprint resin by gravure printing as discussed in Section 2. As there is a certain distance between the coating and the imprinting stage the uncoated part of the PET substrate has direct contact with the polymer stamp attached to the imprint roller until the coated part arrives. This direct contact can cause scratches at the polymer stamp and in order to prevent this a protecting PET foil is attached to the polymer stamp with an adhesive tape which is removed when the coated part of the PET substrate arrives. Then, scratching is not an issue anymore as the liquid resin acts as a lubricant. Parameters that can be adjusted in order to optimize the process comprise web tension and speed, illumination intensity and pressure during imprinting applied by the pressure roller.

3.2.6.4 Anti-adhesive coating

Since the silicon masters used in this work have a relatively high surface energy which causes good adhesion to the imprinted features a low surface energy coating is applied. A usual approach is to apply a fluorinated self-assembled monolayer to the mold surface which leads to surface energies as low as 10 mJ/m^2 [4][107]. They can be covalently bonded to the mold surface and therefore, stick to the mold while providing small adhesion to the imprinted features. Furthermore, they have a low thickness, therefore not distorting the feature shape and can be easily removed and renewed without damaging the master. To apply a new anti-sticking layer to a contaminated silicon master a procedure is followed that is described in [107]. The first step is to clean the mold in a piranha solution (mixture of H_2SO_4 and H_2O_2) which also leads to the formation of Si-OH bonds at the silicon surface. Afterwards the mold is rinsed with deionized water and dried with nitrogen. Then the mold is put into a Optool DSX solution (1 $wt\%$ in perfluorhexane) for one minute which leads to physisorption of the fluorinated molecules at the silicon surface as depicted in Figure 3.11. The structure of Optool DSX is not completely known due to proprietary reasons but in principle is a perfluoropolyether molecule similar to

the one depicted in Figure 3.11. Then the master is put into a water-saturated environment at 65°C for one hour. The water reacts with the fluorinated precursor molecules and terminal -Si-(OH_3) groups are formed which react with the Si-OH bonds of the mold surface to form a covalent Si-O-Si bond between the mold and the anti-sticking layer. Finally, the mold is rinsed in perfluorhexane for ten minutes to remove residual non-bonded molecules and dried with nitrogen.

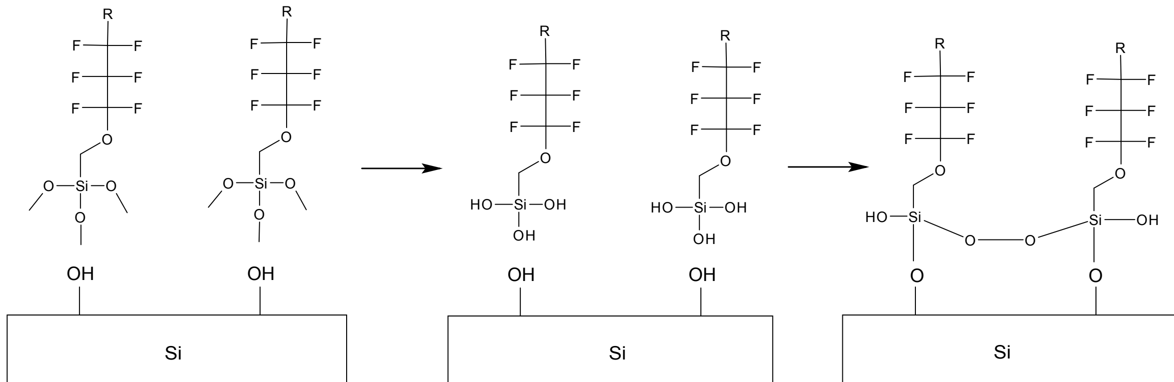

Figure 3.11: First the molecules are physisorbed to the oxidized surface (left). Then water reacts with the precursor molecules to form terminal -Si-(OH_3) groups (middle). Finally, the molecules are covalently bonded to the mold surface (right). Picture modified from [107].

Nickel masters are treated in a different way which is described in the following. In the first step, the mold is cleaned in a mixture of potassium hydroxide and hydrogen peroxide because a piranha solution would attack the metal mold itself. Afterwards, the mold is rinsed with deionized water and isopropanol. Then it is put in a solution of tridecafluorooctylphosphonic acid (2 $mmol/l$ in isopropanol) for one hour and rinsed again with water and isopropanol. Finally, it is annealed at 150°C for ten minutes in an oven.

3.2.7 Evaluation of replication fidelity

3.2.7.1 Atomic Force Microscopy

To measure the shape of micro- and nanoscale features atomic force microscopy (AFM) is employed which has been reviewed, for example in [108][109]. Basically, the system consists of cantilever with a sharp tip attached to a piezoelectric actuator (Figure 3.12). A laser beam is reflected from the backside of the cantilever and detected by a position sensitive photo detector. The measurement principle is to scan the tip over the sample surface, so it changes its height according to the surface topography which is registered by the photo detector. There are several modes of operating an AFM and in the present work the so-called tapping mode is used which allows to measure soft samples which is difficult in contact mode AFM. In tapping mode the tip oscillates near its resonant frequency with a certain amplitude driven by the piezoelectric actuator. When the distance between tip and sample changes because of the surface topography the forces acting between tip and sample cause a change of the oscillation amplitude, i.e. the amplitude increases (decreases) when the distance increases (decreases). A feedback loop adjusts the height of the tip so it regains its original oscillation amplitude. This

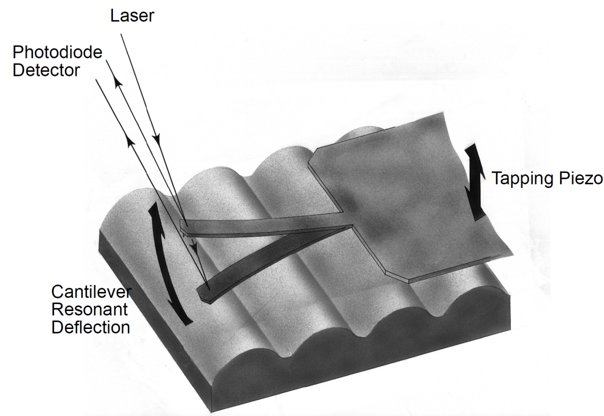

Figure 3.12: Schematic illustration of an AFM setup and measurement. Picture taken from [110].

information as a function of the tip position represents the surface topography of the sample. If the scan speed is too high the feedback loop cannot react quickly enough which results in blurring of the image. In this case the forward and backward direction of a single line (called trace and retrace), which in general are both measured, do not match exactly. Therefore, the scan speed of the tip is always adjusted such that trace and retrace are almost identical for all the measurements performed in this work.

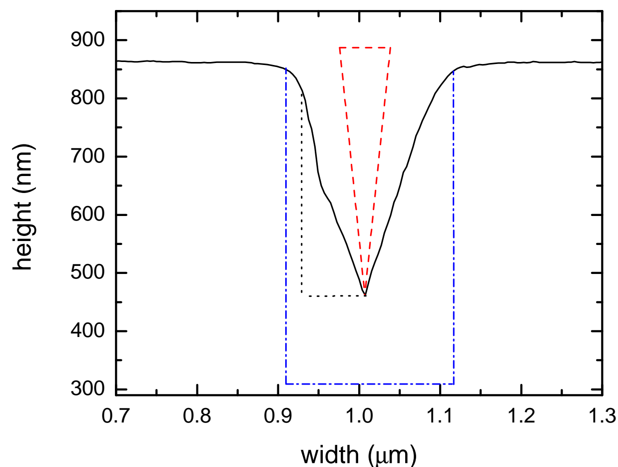

Figure 3.13: The shape of the AFM tip (black line) is obtained by measuring a 200 nm trench (blue dash dotted line). The measured half-angle (black dotted line) is significantly larger then the half-anlge as given by the product specification (red dashed line).

On flat surfaces AFM is capable of atomic resolution imaging, but the lateral resolution is significantly reduced when measuring deep rectangular structures (as common in NIL) due to the lateral dimensions of the tip. To estimate the influence of the tip shape and size, a line and space pattern with a width of 200 nm is measured as depicted in Figure 3.13. The same silicon wafer also has line and space patterns on it with a width of 1600 nm and AFM measurements

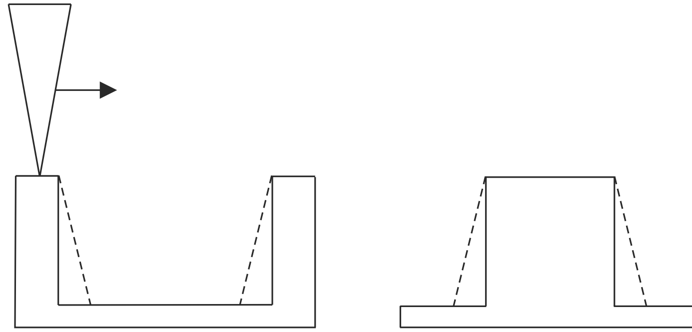

Figure 3.14: Due to the tip influence cavities appear narrower but protrusions appear wider than they actually are. This can lead to imprinted features appearing bigger than the actual mold cavities.

show that the height is approximately 550 nm. The blue lines (dash dot) indicate the real shape of the pattern if the same height is assumed for the 200 nm line-spaces and if vertical sidewalls are assumed. Apparently, the lateral dimensions of the tip make it impossible to touch the bottom of the structures. Therefore, if vertical sidewalls are assumed the measured data actually represent the shape of the tip. From this the half angle of the tip (indicated by the black dotted line) can be calculated and is $\alpha = 12.5°$ which is larger than the product specification of $\alpha = 5 \pm 1°$ (indicated by the red dashed line). Note that the tip has different influences on cavities and protrusions of the pattern. As depicted in Figure 3.14 cavities appear narrower but protrusions appear wider than they actually are. Therefore, it can happen that the AFM profiles suggest that imprinted features are bigger than the actual mold cavities although the imprint itself works well.

3.2.7.2 Profilometry

Samples that are to big to be investigated with AFM (limited to 5 μm height) are examined by profilometry. The profilometer system consists of a stylus with a diamond tip that makes direct mechanical contact with the sample and is mechanically coupled to a precise displacement sensor. The measurement principle is to move the sample stage with a specified scan length, speed and force and simultaneously measure the height displacement of the stylus thereby generating a height profile of the sample surface. Usually single lines are recorded but two-dimensional mapping is possible as well. The Veeco Dektak 150 surface profiler which is used in this work is capable of measuring heights with resolutions below 1 nm [111] but like in the case of AFM the lateral resolution is limited by the tip size (in this work the tip radius is 0.7 μm) when rectangular patterns are investigated. The scans are performed with a scan speed of 10 $\mu m/s$ and a force of 3 mg unless stated otherwise.

3.2.7.3 Scanning Electron Microscopy

Besides AFM, also scanning electron microscopy (SEM) is employed to investigate the nanopatterns [112][113]. SEM uses electron beams to image the sample. Compared to light microscopy much higher resolutions can be achieved due to the lower wavelength of accelerated electrons (in the range of picometers). To image the sample electrons are emitted from a cathode (e.g. by thermionic or cold emission), accelerated towards the surface and focused and controlled with electromagnetic lenses to form a narrrow beam which is scanned along the surface. As the primary electrons penetrate into the sample a variety of interactions occur including (back)scattering and generation of secondary electrons, x-rays and auger electrons which can be detected by several detectors that are in the specimen chamber. Using secondary electrons for image generation gives mainly topographic contrast (whereas backscattered electrons give mainly material contrast) and they are used in this work to investigate the shape of nanostructures. In contrast to backscattered electrons which can originate from higher depths, secondary electrons can only escape from a thin surface layer (1 nm) due to their low energy. This means that at inclined areas more secondary electrons can get out of the sample and be collected by the detector because a greater part of the secondary electrons is generated near the surface (Figure 3.15). Therefore, inclined areas and especially edges appear brighter than flat areas that are perpendicular to the incident electron beam. Deep notches on the other hand can appear darker because the electrons might not be collected by the detector.

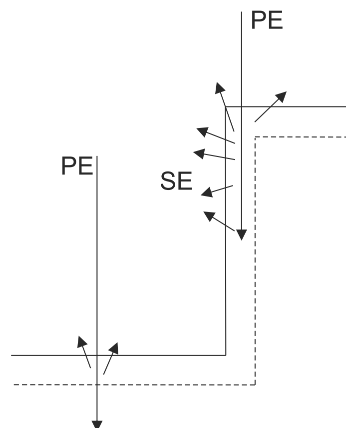

Figure 3.15: Secondary electrons (SE) that are generated by the interaction between primary electrons (PE) and the sample mainly lead to topographic contrast. As SE can only escape from a very thin surface layer (dashed line) more electrons leave the sample at edges and inclined areas which therefore appear brighter.

3.3 Results and discussion

The theory of thiol-ene and acrylate polymerizations and the associated properties were discussed in Section 2.2. This chapter is dedicated to the experimental investigation. To examine the properties of thiol-enes a variety of thiol and ene monomers with varying size, molecular stiffness, viscosity, degree of functionality and functional group chemistry are used. Ene functionalities in this work comprise vinyl, vinyl ether, allyl ether and allyl isocyanurate and allyl triazine groups. Among the thiols there is one secondary thiol (Karenz) which is promising regarding shelf-life stability, the rest being primary thiols. To better understand the effect of thiol chemistry a thiol-acrylate system is also studied in which the thiol content is gradually increased. This should go hand in hand with a gradual transition from pure chain-growth to a mixed step-chain-growth in which the step-growth mechanism gets increasingly pronounced. A mixture of TMPTA and TMPMP is chosen as the thiol-acrylate system because these molecules have similar structures (except the functional groups) and differences observed in any properties can be assigned to the thiol chemistry which might be difficult if the thiol and acrylate monomers had very different structures. Due to their step-growth thiol-enes have to be mixed stoichiometrically if maximum conversion is desired so that the number of ene functional groups equals the number of thiol functional groups (though there might be applications for non-stiochiometric mixtures). The thiol-acrylate system is therefore also based on molar ratios and not weight ratios, e.g. a ratio of TMPTA:TMPMP=4:1 means the number of acrylate functional groups is four times the number of thiol functional groups.

3.3.1 Surface energy

As already mentioned, MD700 is added as a perfluoropolyether surfactant to the imprint and stamp resins to reduce their surface energy when nanoimprint lithography is performed. This reduces adhesion and therefore, facilitates demolding of the imprinted structures. Table 3.3 shows that this surfactant can reduce the surface energy of the resin from about 50 mJ/m^2 to about 10 mJ/m^2. John et al. reported the use of perfluoropolyether (PFPE) acrylates as mold materials and demonstrated high fidelity imprinting of line and space patterns with a width of 230 nm and a height of 500 nm over 300 imprinting cylces in 2013 [114]. PFPE acrylate has a surface tension of about 16 mJ/m^2 but has low elastic modulus (45 MPa). Adding crosslinkers can improve the mechanical properties but this goes at the expense of surface tension [115]. The surfactant used in this work is not only superior regarding the surface energy, but moreover works at concentrations as low as 0.1 $wt\%$, hence has no influence on other properties of the material. This allows to adjust the surface energy completely independently from the elastic modulus, for example, which allows for polymer stamps with high strength and yet low surface energy. The adjustment of surface energy was investigated in greater detail in [116] and it was found that the surface energy of the imprinted resin depends on the adjacent phase during curing. This is because the fluorinated surfactant molecules will only accumulate at the interface if the adjacent phase itself has a low surface energy. However, as shown in Table 3.3, the surface energy is also significantly reduced if the adjacent phase is not air, but a silicon wafer with a fluorinated self-assembled monolayer or a polymer with this surfactant.

Table 3.3: Surface energy γ of TMPMP+CHDMDVE with MD700 at a concentration c cured while in contact to different environments and contact angles of water θ_W and diodomethane θ_D.

c [%]	adjacent phase	γ [mJ/m^2]	θ_W [°]	θ_D [°]
0	air	48.3	80	26
0.1	air	9.8	111	103
0.1	silicon with fluorinated SAM	11.2	108	99
0.1	polymer with 0.1 $wt\%$ MD700	20.4	102	77

3.3.2 Degree of conversion

As discussed in Section 2.2.5 thiol-enes exhibit fast polymerization rates and the addtion of thiols to acrylates should increase the reactivity. Therefore, they offer the potential to increase the throughput of the R2R-UV-NIL process. To investigate this the conversion of TMPTA with varying content of TMPMP is measured. The results are summarized in Figure 3.16 showing the degree of double bond conversion over time. Symbols indicate experimental values the lines are fittings according to Equation 3.17. Increasing the thiol-content has apparently two effects: (i) acceleration of the polymerization and (ii) increasing the final conversion. Reddy et al.

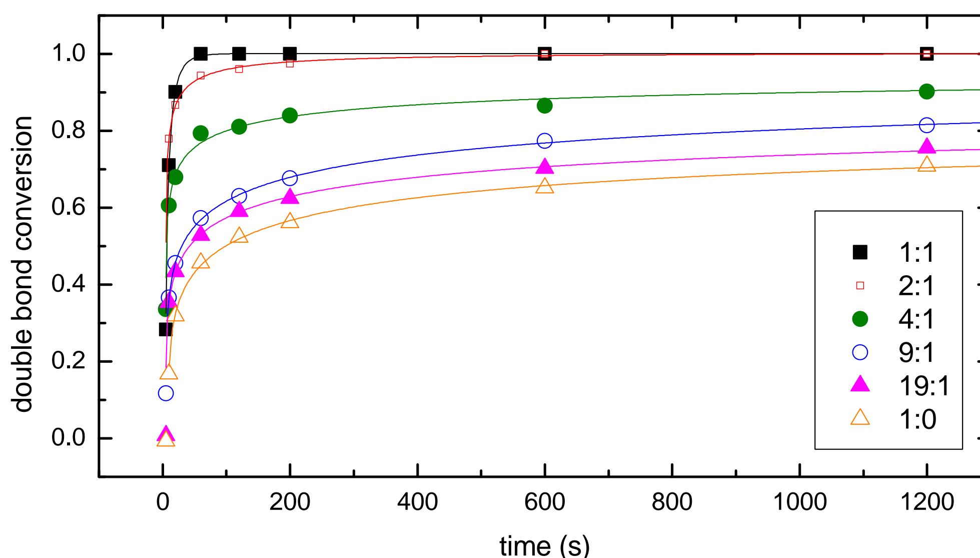

Figure 3.16: Degree of double bond conversion over time for different molar ratios n(TMPTA):n(TMPMP). Symbols indicate experimental values. The lines are fittings according to Equation 3.9.

have shown that the rate constant for the reaction of a thyil radical with an acrylic double bond is much higher than the homopolymerization of the acrylate [118][71]. Therefore, the polymerization proceeds faster with increasing initial thiol content which is beneficial regarding the process throughput. Nevertheless, the thiol conversion is significantly lower than the double bond conversion due to homopolymerization of the acrylate, which gets more pronounced for

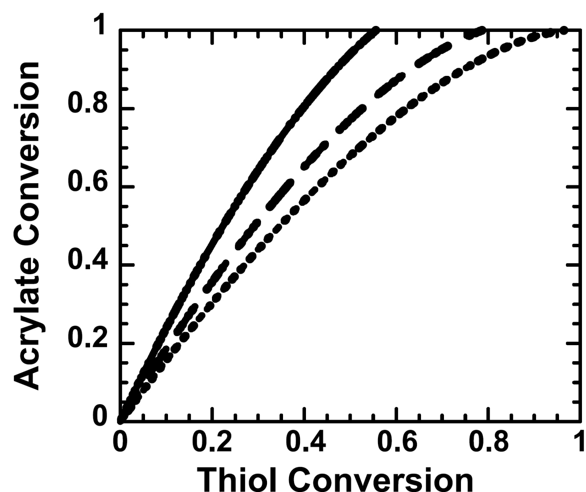

Figure 3.17: Model predictions of acrylate conversion as a function of thiol conversion for several stoichiometric ratios n(acrylate):n(thiol): 1:1(line), 7:3(dashed), 9:1(dotted). Picture taken from [117].

increasing intital thiol content (see Figure 3.17). For example in the case of a stoichiometric mixture (1 : 1) $DC_{C=C}$ = 100 % but $DC_{SH} \approx$ 55 %. As explained in Section 2.2 the final conversion is limited if the polymer vitrifies at conversions well below 100 %. In the thiol-acrylate system the residual thiols lead to a lower glass transition temperature which together with the reduced cross-link density associated with the step-growth mechanism is the reason for the higher final conversion. Regarding the final conversion the optimal composition would be a molar ratio of TMPTA:TMPMP=2:1 because the acrylate and thiol conversion is about 100 % and 80 %, respectively and any change might increase the conversion of one component but would decrease the conversion of the other component at the same time. However, using the R2R UV lamp TMPTA:TMPMP=4:1 reaches almost 100 % conversion (batch process only 90 %) corresponding to a thiol conversion of about 90 % and is therefore, the best choice regarding final conversion. Furthermore, the reactivity is much higher than for lower thiol contents, being beneficial for the process throughput but the shelf-life stability (see Section 3.3.3) is still reasonable. The conversion obtained during the R2R process is generally higher than in the batch process. This is because due to the high light intensity of up to 2.2 W/cm^2 a much higher dose is applied to the samples. Furthermore, the increased intensity leads to elevated temperatures which also lead to higher conversions as discussed in Section 2.2.3.

The conversion of several thiol-enes is depicted in Figure 3.18. For comparison, also TMPTA:TMPMP=2:1 is depicted. To compare the reactivity of several enes they are all mixed with the same thiol, TMPMP. As can be seen CHDMDVE is the ene with the highest reactivity, followed by TAC and TAICROS which are similar. The slowest ene is TVCH which needs about 100 s to reach full conversion, whereas the other enes only need about 10 s. It has been proposed by Cramer et. al that the reactivity of enes depends on the electron density of the carbon-carbon double bond and on the stability of the carbon radical [71]. The electron density controls the propagation step (reaction of a thiyl radical with a double bond) with higher values leading to faster propagation and the carbon radical stability controls the chain-transfer step (i.e. hydrogen abstraction) with more stable radicals reacting more slowly.

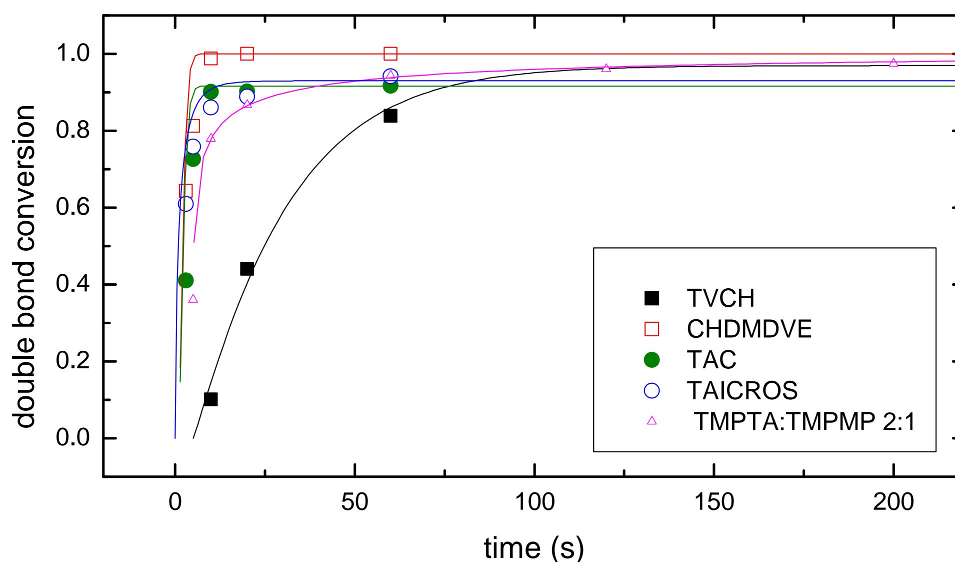

Figure 3.18: Degree of double bond conversion over time of different thiol-enes. To compare the reactivity of different enes they were all mixed with the same thiol, TMPMP. For comparison, also TMPTA:TMPMP=2:1 is depicted. Symbols indicate experimental values. The lines are fittings according to Equation 3.9.

It has been found experimentally that the reactivity of enes follows roughly the following order (beginning with the highest reactivity): vinyl ether > alkene > allyl triazine ≈ allyl isocyanurate > acrylate > methacrylate [71][65]. So the experimental values presented here represent this order quite well except TVCH.

Another factor influencing the reactivity is the choice of the photoinitiator molecule which also determines the thickness of samples that can be cured [119]. Figure 3.19 shows the conversion of TMPMP+TVCH with five different photoinitiators at a molar concentration of 5.3 $mol\%$ which corresponds to 3 $wt\%$ in the case of KL200. If the photoinitiators were added according to weight this would result in different numbers of photoinitiator molecules which would make their comparison difficult. To achieve equal numbers of photoinitiator molecules 119 mg of TPO-L, but 62 mg of KL200 have to be used, for example, because the molecular weight of TPO-L (316 g/mol) is almost twice that of KL200 (164 g/mol). The different initiation rates of the photoinitiators can be explained in terms of initiation efficiency ϕ (see Equation 2.20), molar extinction coefficient ε and the number of produced radicals per initiator molecule. The fragmentation of type I photoinitiators and their reaction with acrylates has been discussed in detail in [120]. As illustrated in Figures 3.20-3.23 the photoinitiators create different numbers of radicals. KL200 and BDK produce two, TPO-L and I819 four radicals. Nevertheless, BDK is similar to I819 and leads to a higher initiation rate than TPO-L. This shows that not only the number of produced radicals is important but also absorption and initiation efficiency play a role. It would be questionable to conclude from these measurements that TPO-L is a better initiator than KL200 because it is the number of produced radicals that puts a maximum on the amount of photoinitiator that can be used. One could simply use

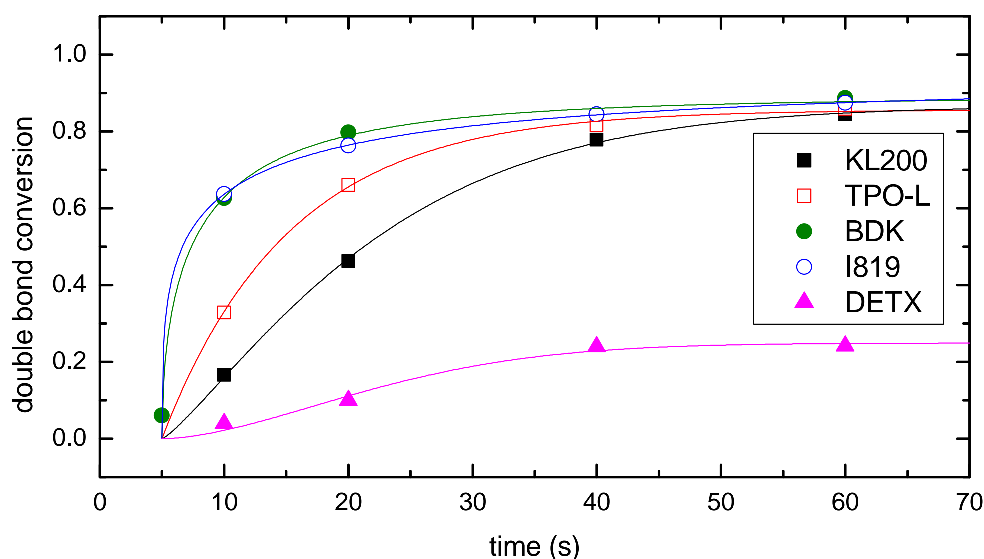

Figure 3.19: Degree of double bond conversion over time of TMPMP+TVCH with different photoinitiators, all at a molar concentration of 5.3 *mol*%. Symbols indicate experimental values. The lines are fittings according to Equation 3.9.

twice the amount of KL200 which would then lead to the same number of radicals as TPO-L. BDK seems to be the most efficient photoinitiator, as it exhibits the highest initiation rates while only producing two radicals per molecule. BDK which is commonly termed DMPA in literature is known to be an excellent photoinitiator [121]. The performance of I819 could not be clearyl identified as it did not dissolve completely in the resin used. DETX is a poor photoinitiator which is probably due to the fact that it is a type II initiator. These type of photoinitiators are usually less efficient because the quantum yield ϕ is lower than for type I initiators [65]. It should be mentioned that BDK, I819 and DETX are powders which makes their handling more difficult. In contrast, KL200 and TPO-L are liquids making their use more convenient.

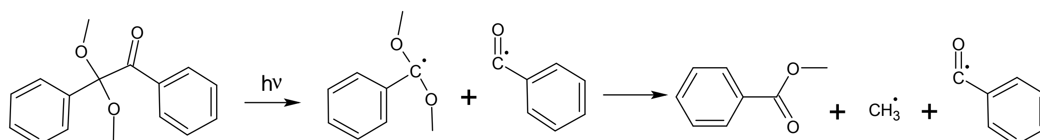

Figure 3.20: Photofragmentation of BDK. Picture modified from [120] and [65].

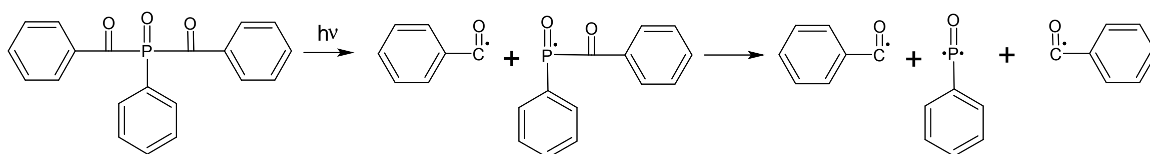

Figure 3.21: Photofragmentation of I819. Picture modified from [120].

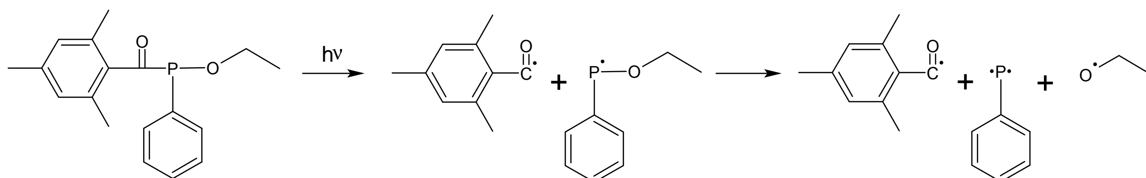

Figure 3.22: Photofragmentation of TPO-L.

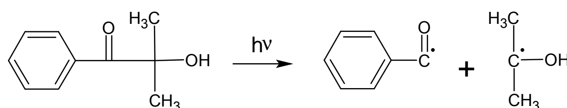

Figure 3.23: Photofragmentation of KL200.

3.3.3 Shelf-life stability

As discussed in Section 2.2.5 thiol-enes have a limited shelf-life stability. To investigate this, samples of thiol-enes and of the TMPTA:TMPMP system are prepared and stored in the dark at room temperature. Table 3.4 shows that the stability of TMPTA:TMPMP decreases strongly for higher thiol contents. TMPTA:TMPTMP=4:1 which was identified as the most promising mixture regarding final conversion has a reasonable shelf-life stability of one month, which can be further increased by storing it below room temperature which would lead to several months of shelf-life stability. TMPTA:TMPTMP=9:1 and TMPTA:TMPTMP=19:1 were still liquid after five months but their viscosity increased compared to the initial value demonstrating that they also react although this happens at a very slow rate. It has been found experimentally, that the shelf-life stability of thiol-acrylate mixtures is inversely proportional to the average acrylate functionality [65]. So, using HDDA instead of TMPTA might be a way to improve the shelf-life stability.

Table 3.5 shows that the stability of some thiol-enes demonstrating that they are limited in this respect. The good stability of Karenz+TAICROS is probably because Karenz is a secondary thiol as already mentioned in Section 2.2.5. Using other thiols results in mixtures with viscosities that strongly increase in a relatively short time (usually a few days). There are several well known mechanisms causing the limited shelf-life stability of thiol-enes such as: (i) the decomposition of peroxide impurities which initiate a thermal free-radical polymerization, (ii) the reaction of hydroperoxide impurities which create thyil radicals and (iii) a base-catalyzed nucleophilic addition of thiols to enes [75]. Interestingly, it was found that TMPMP+TVCH showed an increased shelf-life stability when BDK is used as photoinitiator

Table 3.4: Initial viscosity η_0 and shelf-life stability of samples with varying molar ratios of TMPTA and TMPMP stored at room temperature and in the dark.

n(TMPTA):n(TMPMP)	$\eta_0 [mPas]$	stability
1:0	112	stable
19:1	119	$\eta = 184$ $mPas$ after 5 months
9:1	121	$\eta = 286$ $mPas$ after 5 months
4:1	124	gelled after 1 month
2:1	127	gelled after 5 days
1:1	127	gelled after 2 days

Table 3.5: Shelf-life stability of thiole-enes stored at room temperature and in the dark.

thiol+ene	stability
GDMP+TVCH	gelled after 18 days
Karenz+TAICROS	still viscous after 5 weeks
TEMPIC+TAC	gelled after 8 days
TMPMP+CHDMDVE	gelled after 18 days
GDMP+CHDMDVE	gelled in a few minutes

compared to the other initiators used in this work. Apparently, the photoinitiator influences the shelf-life stability as well. One way to improve the stability is storage at low temperatures. Another possibility is to use stabilizers, many of which are mentioned in [65]. Esfandiari et al. found that the combination of acidic compounds (that should avoid the nucleophilic addition) and the radical stabilizer pyrogallol (that should prevent the other mechanisms) are very efficient [75]. In the present work, it has been found that pyrogallol significantly slows down the polymerization rate when used at concentrations as low as 0.25 $wt\%$ (photoinitiator concentration: 3 $wt\%$ KL200). No significant slowdown was observed at a concentration of 0.01 $wt\%$ although still improving shelf-life stability. However, shelf-life stability is not a severe barrier towards the application of thiol-enes because they can be used as two-component systems, i.e. stored separately and only mixed immediately before usage. Therefore, no special emphasis is put on shelf-life stability in the present work.

3.3.4 Volumetric shrinkage of bulk samples

Volumetric shrinkage induced by polymerization has the potential to reduce the size of the imprinted features during NIL, thereby reducing the replication fidelity of the process. Therefore, it seems desirable to develop an imprint resin with low volumetric shrinkage. To achieve a better understanding of the effect of monomer structure on the overall shrinkage first of all some acrylate monomers are investigated. Table 3.6 shows their experimental shrinkage values. In order to interpret these results also the the degree of conversion DC measured by FTIR and the reactive group concentration $[RG]$ are listed. From these data the shrinkage factor SF is calculated according to Equation 2.28. From a comparison of TMPTA, TMP(EO)$_9$TA and TMP(EO)$_{15}$TA it can be seen that introducing long and flexbile chains between the reactive groups (see Figure 3.1) leads to a strong decrease of shrinkage because the reactive group concentration is much smaller. However, the effect is not as pronounced as would be expected

Table 3.6: Volumetric shrinkage $\Delta V/V$ of several acrylates of functionality f with the respective degree of conversion DC, reactive group concentration $[RG]$ and shrinkage factor S calculated according to Equation 2.28.

acrylate	f	$\Delta V/V$ [%]	DC [%]	$[RG]$ $[mmol/cm^3]$	S $[cm^3/mol]$
HDDA	2	14.7	78	9.0	21.0
TMTPA	3	13.7	71	11.1	17.4
$TMP(EO)_9TA$	3	7.8	100	4.8	16.1
$TMP(EO)_{15}TA$	3	6.2	100	3.5	17.7
PETTA	4	10.3	50	13.5	15.3
DPHA	6	12.4	40	13.2	23.5

Table 3.7: Volumetric shrinkage $\Delta V/V$ of the TMPTA:TMPMP system with the respective degree of conversion DC, reactive group concentration $[RG]$ and shrinkage factor S calculated according to Equation 2.28.

n(TMPTA):n(TMPMP)	$\Delta V/V$ [%]	DC [%]	$[RG]$ $[mmol/cm^3]$	S $[cm^3/mol]$
1:0	13.7	71	11.1	17.4
19:1	13.4	76	11.0	16.1
9:1	12.3	82	10.9	13.8
4:1	12.3	90	10.6	12.8
2:1	11.7	100	10.3	11.4
1:1	8.6	100	9.9	8.7

from the reactive group concentrations because also the final conversion increases from 70 % to 100 % which is because $TMP(EO)_9TA$ and $TMP(EO)_{15}TA$ do not vitrify during polymerization. Comparing HDDA ($f = 2$), TMPTA ($f = 3$), M420 ($f = 4$) and M600 ($f = 6$) shows that, by trend, increasing the functionality (and thereby reactive group concentration) leads to lower shrinkage. At a first glance this contradicts Equation 2.30 but can be explained by the reduced degree of conversion of highly functional monomers.

As discussed in Section 2.2.4 thiol-enes have a lower overall shrinkage and also the addition of thiols to acrylates should reduce shrinkage. Table 3.7 shows the experimental results of the TMPTA:TMPMP system. Increasing the thiol content leads to a decreased shrinkage as expected. However, this is not due to a lower reactive group concentration (more or less unchanged) which is the conventional way to influence shrinkage but mostly due to the decreasing shrinkage factor. All in all the reduction of shrinkage is not very pronounced as the difference between pure TMPTA and TMPTA:TMPMP=2:1 is only 2 %. This is because the shrinkage reduction is compensated to some extent by an increased degree of conversion for higher thiol contents. The low shrinkage of the TMPTA:TMPMP=1:1 mixture is mainly because large parts of thiol monomers remain unreacted as depicted in Figure 3.17. So, on the one hand adding thiols to acrylates with limited conversion is not an effective way to decrease shrinkage, but on the other hand thiols offer the possibility to increase the final conversion without leading to higher shrinkage at the same time. However, if the acrylate itself already reaches full conversion as in the case of $TMP(EO)_9TA$, for example, the addition of thiol would lead to a stronger decrease of shrinkage.

Finally, Table 3.8 summarizes the shrinkage data of some true thiol-enes. As expected

Table 3.8: Volumetric shrinkage $\Delta V/V$ of several thiol-enes with the respective degree of conversion DC, reactive group concentration $[RG]$ and shrinkage factor S calculated according to Equation 2.28.

thiol+ene	$\Delta V/V$ [%]	DC [%]	$[RG]$ $[mmol/cm^3]$	S $[cm^3/mol]$
GDMP+TVCH	11.1	100	13.5	8.2
Karenz+TAICROS	8.3	96	10.4	8.2
TEMPIC+TAC	7.1	88	9.9	8.2
TMPMP+CHDMDVE	8.4	100	9.1	9.2

they all have relatively low shrinkage values and high conversions compared to conventional acrylates and as mentioned before their low shrinkage is mostly not due to a low reactive group concentration but rather because of their low shrinkage factors. This can be seen quite nicely by comparing TMPMP+CHDMDVE with TMP(EO)$_9$TA: both have similar shrinkage and conversion although the reactive group concentration of the thiol-ene is about twice as high. The reason for the similar shrinkage is that the shrinkage factor is only about one-half compared to the acrylate. This is because of the step-growth mechanism of thiol-enes as discussed in Section 2.2.5. Each ene forms a single bond with a thiol whereas in the polymerization of acrylates each functional group is attached to two other acrylates. Apart from that, the trends are same same as for acrylates. Increasing the reactive group concentration leads to higher shrinkage, whereas incomplete conversion reduces the shrinkage.

3.3.5 Mechanical properties

As discussed in Section 2 the mechanical properties play an important role in the NIL process. Table 3.9 shows the reduced modulus E^* and the hardness H for several acrylates measured by microindentation. Comparing TMPTA, TMP(EO)$_9$TA and TMP(EO)$_{15}$TA shows that introducing longer chains reduces both Young's modulus and hardness. This is because longer chains both reduce the cross-link density and add flexibility which reduces the glass transition temperature. The other acrylates have rather similar moduli despite different functionality, the reason being differences in final conversion. Higher functionalities increase the polymer hardness by trend.

The mechanical properties of the TMPTA-TMPMP system are shown in Figure 3.24. For comparison also values of TMP(EO)$_3$TA-TMPMP are given which have been measured by nanoindentation and were taken from [116]. Due to the longer chains the values that correspond to TMP(EO)$_3$TA are generally lower compared to TMPTA. This comparison indicates that it is better to mix TMPTA with TMPMP than replacing it by TMP(EO)$_3$TA. Both will increase the double bond conversion, but adding thiol does not reduce the mechanical properties as much. Increasing the thiol content shows an interesting development that has not been explained in [116]: for TMPMP content up to 20 % there is a rather moderate decrease in Youngs modulus but for higher thiol content a drastic descent occurs. The reason for this might be the decrease of T_g with increasing TMPMP content. Up to 20 % thiol content the polymers are in the glassy state and therefore, the change in modulus is rather small. This is also because the effect of the reduced cross-link density upon addition of thiol due to the step-growth mechanism is reduced by an increased double bond conversion. At higher thiol concentrations T_g falls below room temperature which is associated with a drastic decline of the modulus as depicted in

Table 3.9: Reduced modulus E^* and hardness H of several acrylates.

acrylate	E^* $[MPa]$	H $[MPa]$
HDDA	5891	286
TMPTA	5328	401
TMP(EO)$_9$TA	1250	183
TMP(EO)$_{15}$TA	808	141
PETTA	5478	538
DPHA	5386	461

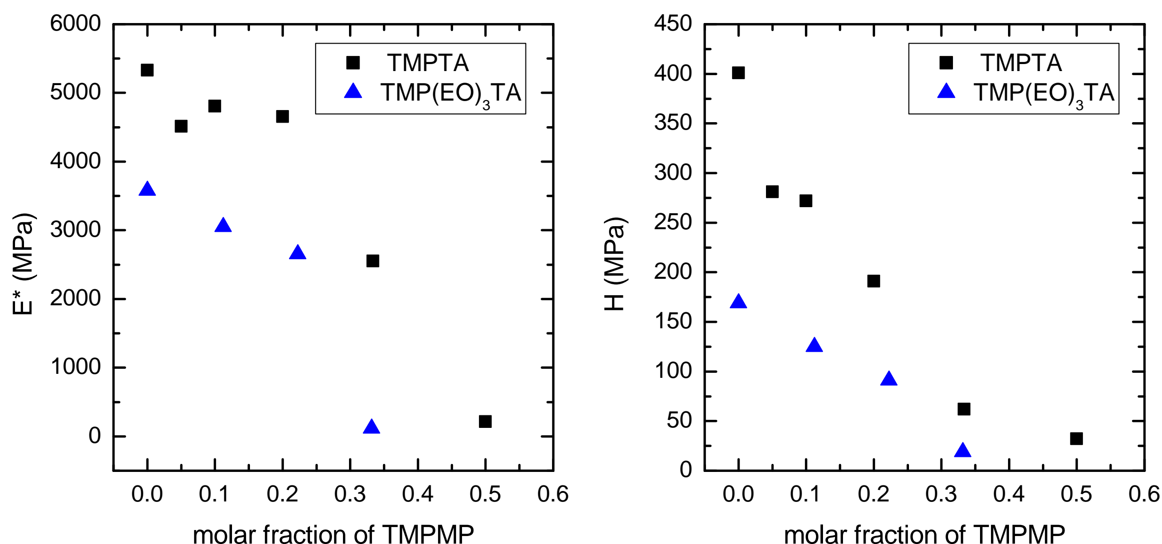

Figure 3.24: Reduced modulus (left) and hardness (right) for acrylate resins (TMPTA, TMP(EO)$_3$TA) with different thiol (TMPMP) contents. Values corresponding to TMP(EO)$_3$TA were taken from [116].

Figure 2.14. In contrast to the modulus, hardness decreases linearly when increasing the thiol content. The effect of thiol content on modulus and glass transition temperature has also been investigated by Cramer et al., the results being depicted in Figure 3.25 for comparison [122]. Increasing the thiol content has two effects: first, the modulus in the rubber region decreases due to the lower cross-link density and second, T_g decreases. Cramer et al. also found that the glass transition temperature decreases linearly with the thiol content as shown on the right of Figure 3.25. Since hardness is proportional to T_g as discussed in Section 2.2.6 this explains the linear decrease of hardness.

Table 3.10 shows the mechanical properties of some thiol-enes. Hardness as well as Youngs modulus are relatively small compared to acrylates which is due to their reduced cross-link density (shrinkage factor) as discussed in Section 2.2.4. An exception is Karenz+TAICROS and this might be explained by the fact that it is in the glassy state because of the high functionality of Karenz ($f = 4$) and the stiffness of TAICROS whereas the others are in the rubber state. In an attempt to produce high T_g thiol-ene polymers Carioscia et al. synthesized several norbornene monomers which lead to stiff polymer backbones due to the ring structure

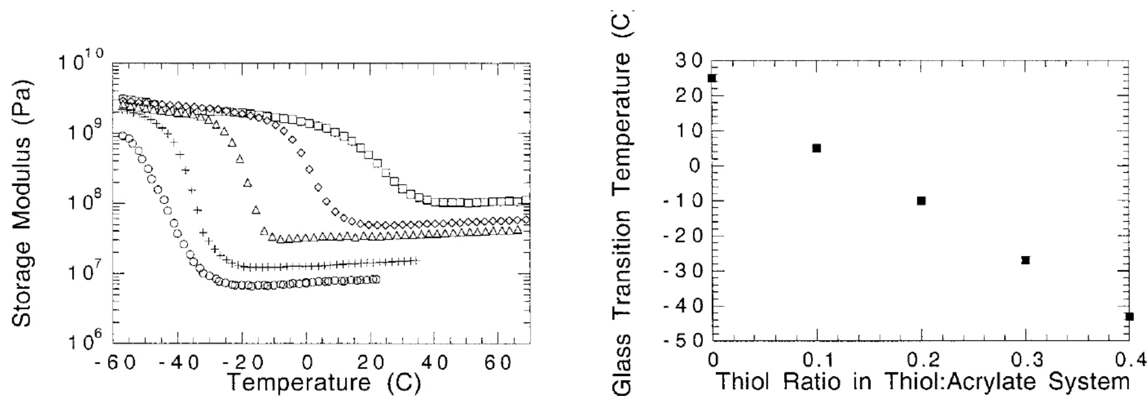

Figure 3.25: Modulus of a acrylate:thiol system with molar ratios of 1:0(□), 10:1(◊), 10:2(△), 10:3(+) and 10:4(∘) (left) and dependancy of glass transition temperature on thiol content (right). Picture taken from [122].

Table 3.10: Reduced modulus E^* and hardness H of several thiol-enes.

thiol+ene	E^* $[MPa]$	H $[MPa]$
GDMP+TVCH	294	27
Karenz+TAICROS	6859	88
TEMPIC+TAC	338	79
TMPMP+CHDMDVE	327	87

of the norbornene functionality. They achieved glass transition temperatures up to $90°C$ but at the expense of high viscosities of 1500 $mPas$ and beyond. So, norbornenes are not really well suited for UV-NIL. They also examined a combination similar to Karenz+TAICROS, namely PETMP+TAICROS (PETMP has functionality four as well) with $T_g = 63°C$ and $\eta = 280$ $mPas$ which looks more promising (but low shelf-life stability of one day). So, despite their smaller cross-link density thiol-enes are not restricted to low moduli. In fact, PETMP+TAICROS has the highest glass-transition temperature among commercially available thiol-enes [17]. Imprinting of 100 nm line and space patterns (50 nm height) in an SFIL-process has been demonstrated with this thiol-ene [123]. So, one might conclude that thiol-enes can have high elastic moduli when stiff monomers are chosen, but there hardness remains limited compared to acrylates. Another point to mention is that thiol-enes, due to their step-growth mechanism, exhibit higher network homogeneity compared to chain-growth polymers (as acrylates). Furthermore, they develop much less stress during polymerization which makes them less brittle. Both is beneficial for their mechanical properties and gives them outstanding performance as emphasized in [65]. For example, TMPMP+TAICROS shows extremely high impact resistance.

One should keep in mind that the measured values of hardness and elastic modulus are obtained by applying compressive stress to the material. When the stamp and the imprint are separated they are rather subjected to tensile stresses. It is therefore not sure what the measurements imply for the demolding step and one should be careful when interpreting hardness and modulus measured by indentation. It has been shown that hardness is correlated to

the ultimate tensile strength (by the well known Tabor relation) and to the yield strength of metals [124][125]. This applies to semi-crystalline polymers as well [126] but it is questionable if it is generally true for polymers [127][128]. The ultimate tensile strength correlates also with the elastic modulus [129]. In a number of publications Berry demonstrated that the Griffith theory which has originally been introduced for metals also applies to polymers in the glassy state [129][130][131][132][133]. According to the Griffith theory the tensile strength is proportional to the tensile modulus of elasticity. Therefore, increasing the elastic modulus should be beneficial as it increases the tensile strength.

3.3.6 Nanoimprint lithography

The replication fidelity is probably the most important aspect of NIL as the performance of the fabricated structures might suffer if accuracy is not sufficient. Major factors that might cause inaccurate replications are mechanical defects introduced during demolding and polymerization-induced shrinkage. Both will be discussed in the following.

3.3.6.1 Evaluation of demolding

As discussed in the previous section, high elastic moduli resulting in high tensile strength might be beneficial for demolding since mechanical failure of the imprinted structures is prevented in this way. However, demolding is more complex than a tensile test of the material. Therefore, simply increasing the elastic modulus as much as possible is not the best way to achieve successful demolding. In a computational study Amirsadeghi et al. investigated the stress evolution throughout the imprinted features and found that increasing the cross-link density, hence elastic modulus and tensile strength more and more does not improve demolding endlessly and can even become detrimental at some point which means there is an optimal cross-link density [134]. This is because an increased cross-link density has two opposing effects. On the one hand it increases the tensile strength but on the other hand it leads to higher stresses during demolding as explained in the following. First, the adhesion force is higher for higher elastic moduli. According to Pollock et al. the adhesion force F_{adh} between two flat, elastic, cylindrical solids in contact with each other is given by

$$F_{adh} = \sqrt{\frac{3}{2}\pi\gamma K R^3}, \tag{3.23}$$

where R is the radius of the interface, $\gamma = \gamma_1 + \gamma_2 - \gamma_{12}$ where γ_1, γ_2 and γ_{12} are the surface energy of the stamp, of the imprint and the interface energy, respectively and K is given by

$$\frac{1}{K} = 0.75\left(\frac{1-\nu_1^2}{E_1} + \frac{1-\nu_2^2}{E_2}\right), \tag{3.24}$$

where E_1 (E_2) and ν_1 (ν_2) are elastic modulus and Poisson's ratio of the stamp (imprint) material [135]. This means that decreasing the elastic modulus of the stamp or the imprint can decrease the demolding force as is the case for low surface energies. It was shown experimentally by Amirsadeghi et al. that polymers with a lower modulus require smaller demolding forces [136]. Jiang et al. and Ye et al. showed that partial curing of the resin reduces the demolding force due to a lower elastic modulus [137][138]. Furthermore, it was shown experimentally, that this reduced force results indeed in an improved demolding. Amirsadeghi et al. showed that, despite lower modulus, a mixture of poly(propylene glycol diacrylate):TMPTA=7:3 exhibits

better demolding properties than a 1:1 mixture. However, pure poly(propylene glycol diacrylate) is even worse because the tensile strength is not high enough to tolerate the demolding stresses. The existence of an optimum elastic modulus was also shown by Jiang et al. and Ye et al. who investigated demolding for varying degree of conversions, hence elastic moduli (controlled by the applied UV light dose) [137][138]. Both a too low and a too high curing time was detrimental for demolding and the best results were achieved with intermediate curing.

Furthermore, stress is not only induced by the demolding force but also by the polymerization itself. This is because the polymers develop stiffness which impedes shrinkage. This gets more pronounced for higher cross-link densities (Equation 3.25) leading to both higher modulus E and shrinkage-induced strain ε [139][140]. The polymerization-induced stress σ can be calculated by

$$\sigma = \int E \, d\varepsilon. \tag{3.25}$$

Lu et al. showed that thiol-enes develop much lower stress during the polymerization compared to conventional acrylate systems [61]. First, this is due to their lower overall shrinkage and second, this is because of their delayed gel-point since stress only starts to build up after the gel-point because shrinkage can be accommodated by liquid flow before.

From the discussion above, it might be expected that, due to their low stress, thiol-enes exhibit better demolding characteristics than acrylates. However, experiments show that acrylates are usually easy to separate from the mold leading to defect-free replications in most cases. In contrast, thiol-enes generally adhere well to the polymeric stamps and relatively high forces have to be applied to separate them. Therefore, replications often have a bad quality exhibiting many missing features. In some cases, the PET substrate is peeled off while the imprint resins stick to the mold. In fact, the good adhesion properties of thiol-enes are well known and are due to the low stress build-up during polymerization [65]. The reason is that the strength of an adhesive joint is reduced if it exhibits shrinkage stresses [36] as indicated by Equation 2.10. When the imprint resin is pre-strained this effectively lowers the force necessary for demolding [34] which is why separation is easier for acrylates.

In an attempt to achieve successful demolding with thiol-enes, imprints have been made from of a polymeric stamp (E8210:HDDA=1:1, 3 $wt\%$ KL200, 0.5 $wt\%$ HFPO) with three different enes (CHDMDVE, TVCH, TAC) and TMPMP as thiol. The polymer stamp pattern consists of simple test structures such as lines and spaces with aspect ratios ranging from 0.3 to 2.5 (0.5 μm height, 1.6 μm – 0.2 μm width). The first peculiar finding is that TMPMP+CHDMDVE required the lowest and TMPMP+TAC the highest demolding force. This might be explained with Equation 3.23 since TMPMP+CHDMDVE and TMPMP+TAC have the lowest and highest elastic modulus, respectively. However, with both materials rather poor-quality replications were obtained. The best results were obtained with TMPMP+TVCH which has an intermediate elastic modulus although the imprint was not defect free either. Interestingly, partial curing (to about 60 % conversion) or heating of the imprint with a hot plate facilitated demolding, probably due to a lower elastic modulus. To further improve demolding several perfluoropolyether (meth)acrylates (MD700, MD40, LR2000) have been tested as mold materials since they are well known for their low surface energy and low adhesion. Defect-free demolding was achieved using LR200 as mold and TMPMP+TVCH as imprint material. Demolding was, however, not successful wit TMPMP+CHDMDVE or TMPMP+TAC as imprint material.

From the discussion above it seems that there are several factors governing the demolding step. On the one hand, high cross-link densities increases the strength of the material but on

the other hand increase the demolding force as well. According to Equation 3.23 high-modulus acrylates should require a high demolding force. However, this seems to be compensated by the large stress they develop during polymerization which lowers the demolding force according to Equation 2.10. In extreme cases, peeling can even occur spontaneously without external force. Thiol-enes, however, generally are more difficult to demold successfully and the surface energy and elastic modulus of both stamp and imprint material have to be tuned carefully to achieve defect-free demolding. All in all, demolding is a complex issue which has been investigated, for example, in [37][40][43] but is not understood completely so far.

3.3.6.2 Evaluation of shrinkage

As mentioned before, shrinkage is another major cause why the shape of imprinted features might not exactly match that of the mold features. To investigate the effect of shrinkage on the replication fidelity simple line and space patterns (0.5 μm height, 10 μm width) are replicated from a silicon template. The low aspect ratio of 0.05 allows successful demolding with all imprint materials. The profile of both the master and the replicas are measured using atomic force microscopy. The results are presented in Figures 3.26-3.28. Imprint protrusions appear slightly wider than the mold cavities due to the tip influence of AFM measurements as discussed in Section 3.2.7.1. The most striking feature, however, is that apparently no shrinkage occurs although the very same resins exhibit bulk shrinkage values ranging from 6 % to 15 %. This seems to be quite general, since the experimental finding is the same for a range of monomers with different structures, functional group chemistries, reaction rates, polymerization mechanisms and mechanical properties.

To support this experimental finding electron microscopic images of riblet structures are recorded.[1] The way that is usually presented in literature is to separate mold and imprint after curing and investigate them independently with electron microscopy. Here, a different approach is used in which both are viewed while still in intimate contact with each other. This has the advantage that exactly the same position of stamp and imprint are investigated and allows easy observation of shrinkage. For this purpose an imprint is made from a polymeric stamp and both are cut with a microtome, followed by a thin metal coating (applied via evaporation). The resulting cross-sectional SEM image is depicted in Figure 3.29 showing the mold and imprint between their corresponding PET substrates. No contrast between mold and imprinted structures is visible because both are still in intimate contact with each other. Apparently, no signifacant shrinkage occurred although the resin used (TMPTA) has a bulk shrinkage of 14 % which should have lead to a gap between polymer stamp and replication. However, at some other locations of the same mold-imprint arrangement separation already set in and Figure 3.30 shows the lack of shrinkage in the NIL process even after separation. Hence, the electron microscopic investigation corroborates the AFM results.

In literature there is no consensus about the presence of shrinkage during the NIL process. It was concluded that "no clear result has yet been obtained [and] there exists a discrepancy between experimental results and results of simulation" (Hiroshima et al. [141]). Unfortunately, in many studies about pattern fidelity the authors do not discuss shrinkage explicitly. High fidelity is often concluded without giving quantitative results and it is not clear whether polymerization shrinkage had an effect on the imprinted feature shape in these studies. In an investigation of pillar structures Campos et al. found good fidelity for low aspect ratio

[1] I want to thank Dr.^{in} Maria Belegratis for recording the SEM images.

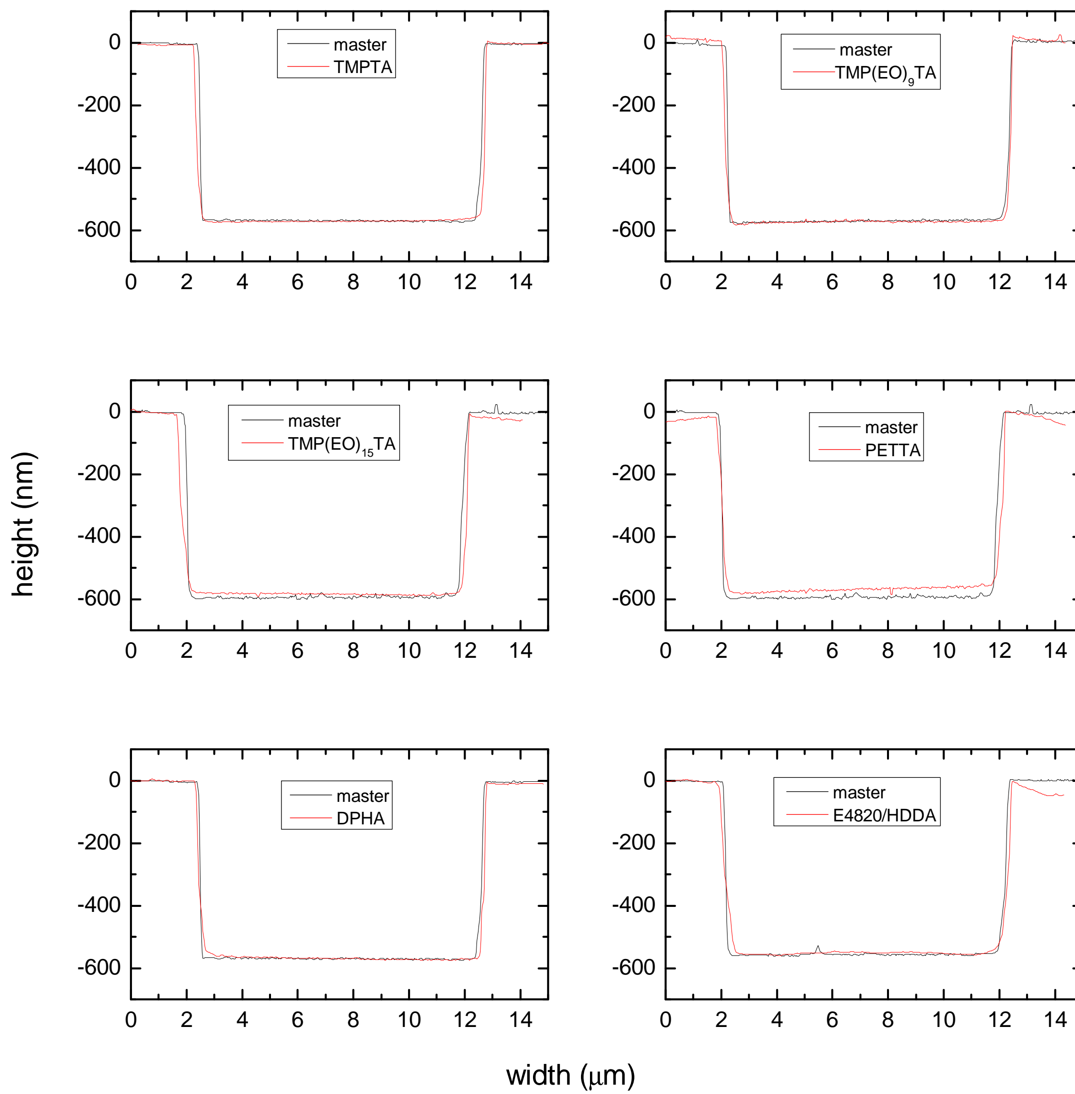

Figure 3.26: Height profiles of the silicon master and imprinted features for several acrylates.

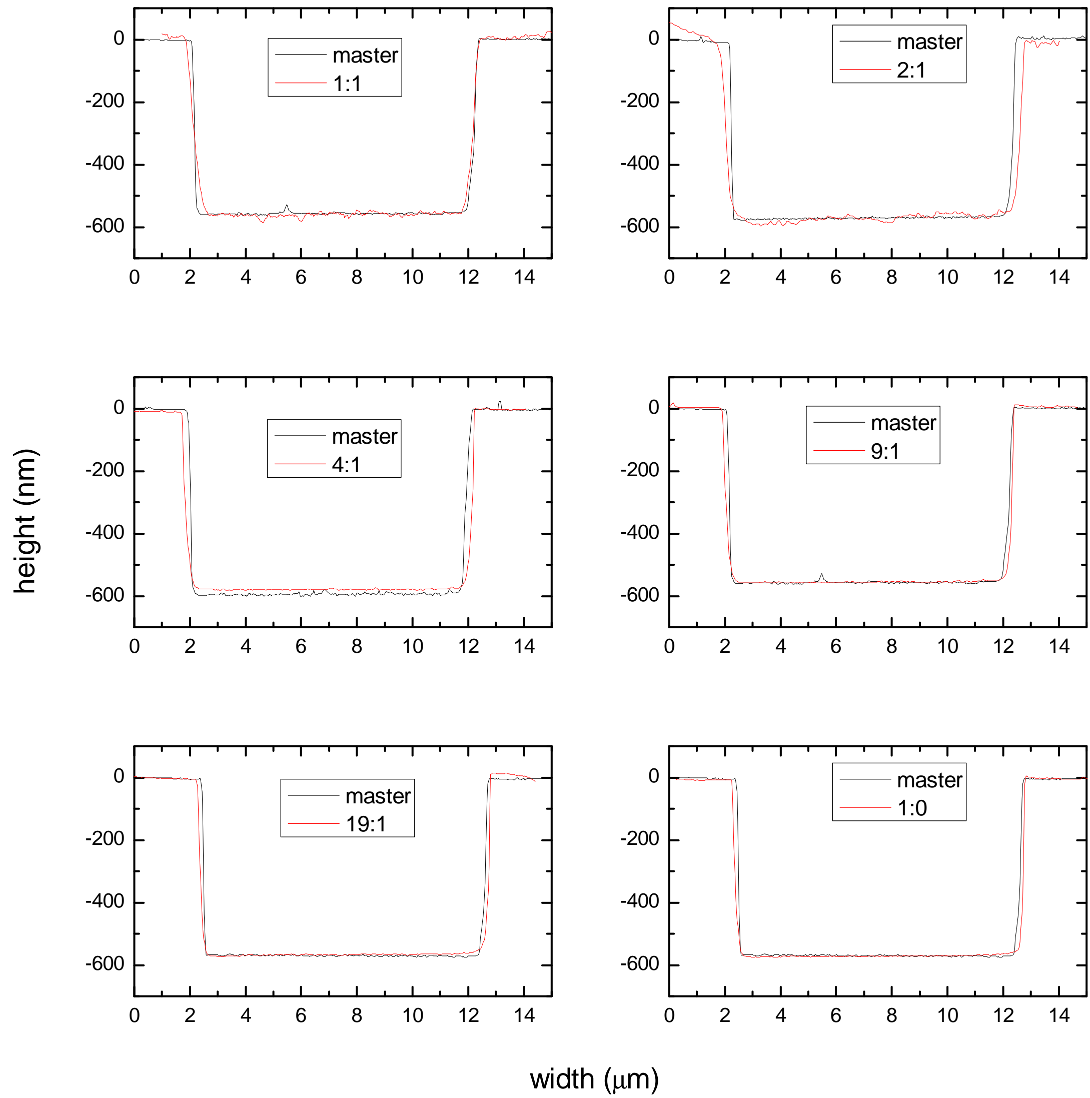

Figure 3.27: Height profiles of the silicon master and imprinted features for different molar ratios n(TMPTA):n(TMPMP).

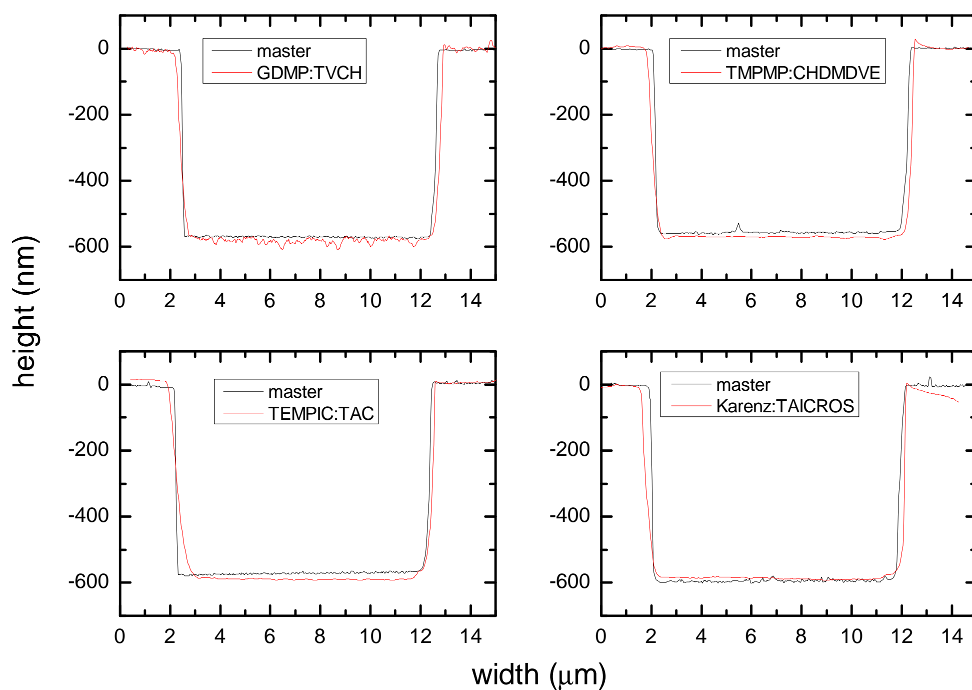

Figure 3.28: Height profiles of the silicon master and imprinted features for several thiol-enes.

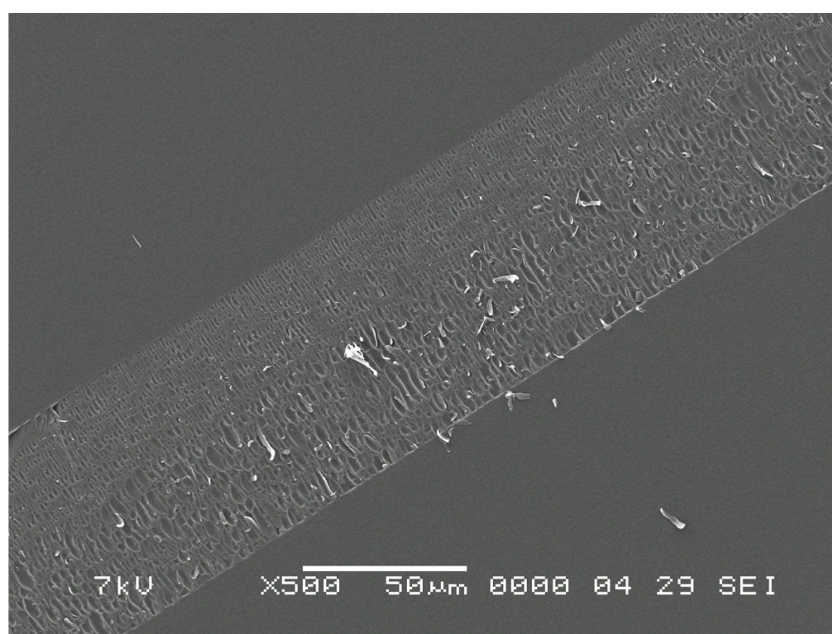

Figure 3.29: SEM image of riblets structures replicated from a polymer stamp (both made of TMPTA). Both cannot be distinguished because they are still in intimate contact with each other which demonstrates the lack of shrinkage.

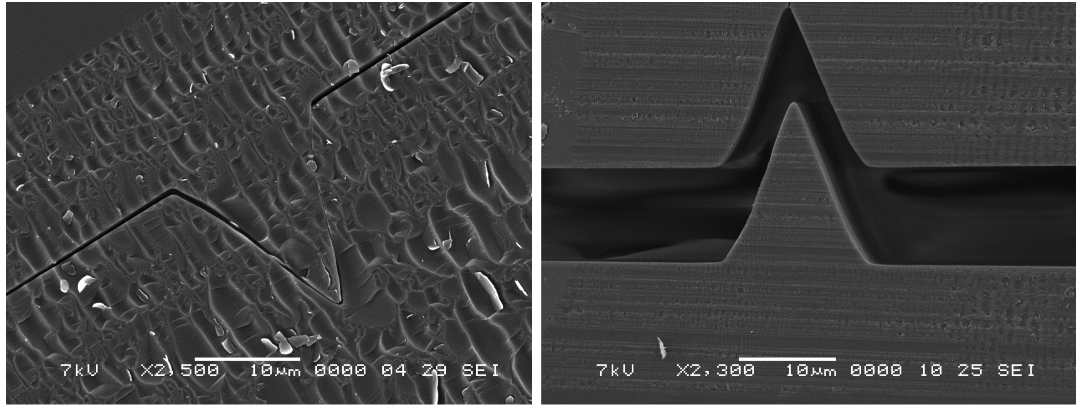

Figure 3.30: SEM image of riblets structures replicated from a polymer stamp (both made of TMPTA). Even after separation the stamp and imprint features match exactly although the resin exhibits a bulk shrinkage of 14 %.

features but bad fidelity for high aspect ratios, but the reason is probably rather collapse of the high aspect ratio features due to their low stiffness [142]. The imprints are termed 'high fidelity' despite differences in height as large as 20 %. John et al. found an excellent pattern replication during a large area roll-to-roll process [114]. However, the authors mainly focused on the lateral dimensions of the pattern although shrinkage is predicted to occur mainly in the vertical direction as detailed later on. Hagberg et al. discovered that low modulus materials can severely reduce the pattern fidelity [143] but simulations using finite element methods (FEM) predict that modulus may affect the separation but does not affect the feature profiles during polymerization [144]. The same simulations also predict that densification of monomers significantly affects the vertical shrinkage but there is little effect on lateral dimensions because the lateral movement of the resin is constrained due to adhesion to the substrate. In a combined experimental and computational study using FEM simulations Johnson et al. found that shrinkage decreases the feature size and that this happens mainly in vertical direction [145]. This height reduction of approximately 20 % was also mentioned in a review later on [12]. Interestingly, some of these authors presented contradicting results one year earlier [58]. They performed both mesoscale and FEM simulations that predict the occurance of shrinkage. In the experimental part, however, they imprinted 100 *nm* line spaces with resins that exhibit bulk shrinkage values between 5 % and 15 %. SEM images showed that the imprinted features had nearly identical size and shape as the template structures which was surprising for the authors. They proposed two explanations that are illustrated in Figure 3.31: (i) density fluctuations inside the imprinted features or (ii) accomodation of shrinkage by flow thereby reducing the residual layer thickness. Concerning the second case, it was shown by Jin et al. that this mechanism occurs in the case of thiol-enes due to their delayed gel-point (however, only if the residual layer is thick enough to provide enough volume) but is not possible for acrylates [74].

To elucidate the influence of the residual layer residue-free imprinting is performed using TMPTA as resin which has a bulk shrinkage of 14 %. If the lack of shrinkage would be due to mass transfer from the residual layer the imprinted features should exhibit shrinkage if there is no residual layer at the beginning. In this case, their height should be reduced compared to imprints where a residual layer is present. Figures 3.32 and 3.33 show height

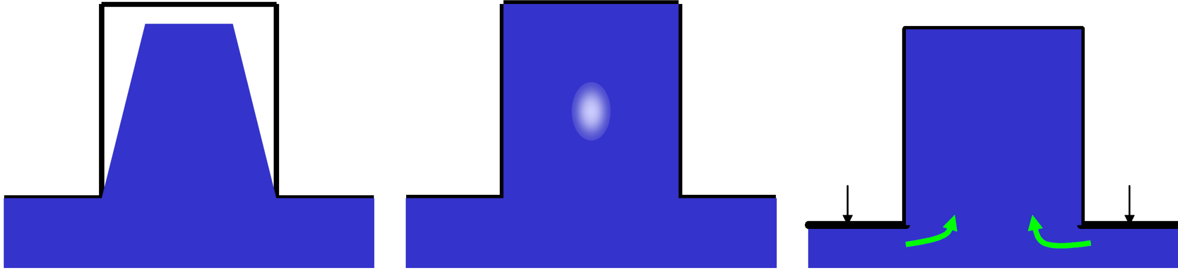

Figure 3.31: Shrinkage as expected from bulk measurements should decreases the replication fidelity (left). Reasons for the lack of shrinkage during NIL might be density fluctuations inside the sample (middle) or mass transfer from the residual layer into the mold cavities. Picture taken from [58].

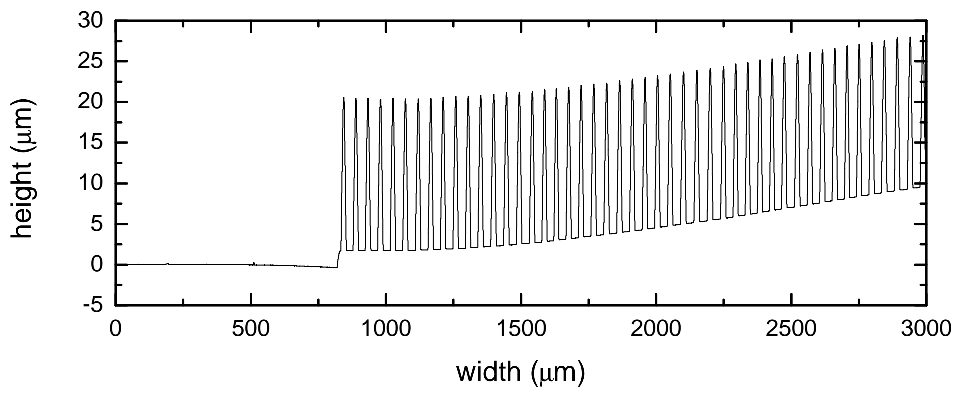

Figure 3.32: Height profile of riblet structures that were imprinted with residual layer. The step that is visible at the point where the stylus changed from the PET substrate to the riblets indicates the presence of a residual layer.

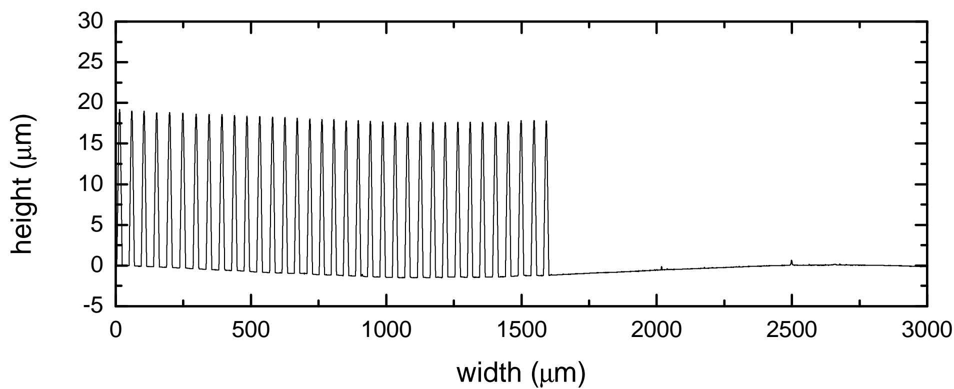

Figure 3.33: Height profile of riblet structures that were imprinted without residual layer. There is no height difference between the bottom of the riblets and the PET substrate.

profiles measured by profilometry of replicated riblet structures imprinted with and without residual-layer, respectively. The profilometer scan was started at the PET substrate the stylus moving towards the imprinted features. When the stylus arrived at the imprint a step occurred indicating the residual layer as depicted in Figure 3.32. This step is not present in in Figure 3.33 indicating that residual-free imprinting was performed successfully. The average heights (measured over ten riblets) of features imprinted with and without residual layer are $18948 \pm 122\ nm$ and $18911 \pm 89\ nm$, respectively, although shrinkage should have caused a height reduction of almost 3 μm. This shows that the lack of shrinkage cannot be explained with the presence of a residual layer.

Attempt to explain the lack of shrinkage

The difference between bulk shrinkage and shrinkage during NIL is that the former is measured at samples that are essentially free to move during polymerization whereas in the latter case the resin is bonded to the mold cavities and the PET substrate and is therefore, not allowed to move freely. It was stated that when the resin "is bonded on all sides to rigid structures, bulk contraction cannot occur" (Davidson et al. [146]) and shrinkage might be compensated by an increased porosity. Gilbert et al. investigated polymerization shrinkage in bone cement and found that samples that are constrained develop porosity [147]. However, these are studies on macroscopic samples. Burns et al. performed mesoscale simulations and calculated the shrinkage during NIL for different interactions strengths between resin and template [58]. These simulations predict that in the case of weak interactions NIL shrinkage is equal to the bulk shrinkage values but as the interactions with the template walls approach the van der Waals interaction of the resin molecules, NIL shrinkage is strongly decreased. This consideration also reflects the fact that a resin which is bonded on all sides is not allowed to shrink which might be the explanation for the lack of shrinkage observed. Coming from these results it would actually be surprising if shrinkage occurred during NIL. However, the imprint material and the mold surfaces are treated to have low surface energies so that they exhibit low adhesion to each other. Therefore, the question remains why interactions between template and resin should be so strong that no shrinkage is observed.

An explanation might be that the strong resin-template interactions are caused by the drastically increased surface to volume ratio of a nanopatterned template compared to a bulk polymer. It is well known that at small size scales surface effects become increasingly important. As explained in Section 2.1.2 surface tension can even lead to the deformation of stamp protrusions (see Equation 2.4), but this is only pronounced for very small features when the surface to volume ratio is sufficiently high. The situation during curing (when shrinkage occurs) is illustrated in Figure 3.34. When two molecules react and replace their van der Waals distance by shorter covalent bonds some kind of volume generation has to occur. The resin molecules either (i) increase the distance to the template (external shrinkage) or (ii) they adhere to the template and increase their mutual distance in the bulk (internal shrinkage). Assuming that shrinkage will be accomodated by an increase of the intermolecular distance (internal shrinkage), this will afford a certain amount of energy because work has to be done against the attractive forces acting between the molecules. This energy will increase with the number of bulk molecules. In the case of external shrinkage work has to be done to separate the resin molecules from the template surface. This energy will increase with the number of surface molecules. Therefore, if the numbers of surface molecules compared to bulk molecules (i.e. the surface/volume ratio) exceeds a certain value, internal shrinkage will be energetically

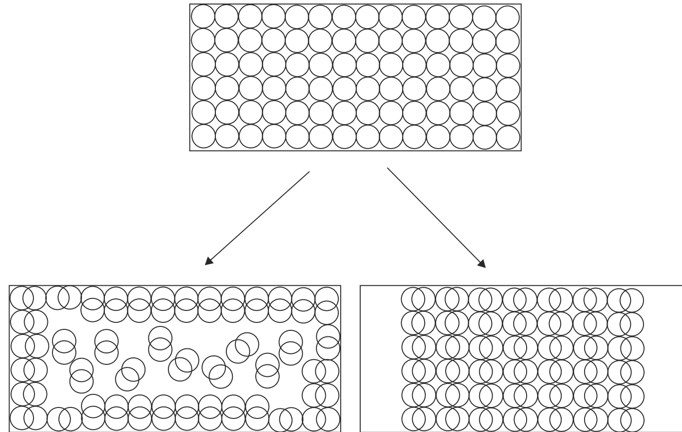

Figure 3.34: Due to polymerization shrinkage some kind of volume generation has to occur: either development of internal voids (left) or overall contraction of the polymer (right).

favorable over external shrinkage. However, this is not expected to play a role for structures in the micrometer-regime which also were shown to exhibit no significant shrinkage. Therefore, the reason for the lack of shrinkage is not understood completely.

3.3.7 Roll-to-roll imprinting

3.3.7.1 Evaluation of shrinkage

After having explored the basic relationships between monomer structure and polymerization rate, final conversion, shrinkage and mechanical properties as well as the behavior during the batch process, R2R-imprinting is investigated. In the following, AFM profiles of the silicon master, the polymer stamp and the imprint will be compared to investigate the effect of shrinkage. It is important to recognize that it is the resin that shrinks which means that protrusions get smaller and cavities grow. This can be confusing because the polymer stamp is a negative replication of the master and therefore, protrusions of the stamp represent cavities of the master and vice versa. It is the same for the imprints, which are a negative replications of the polymer stamp. As depicted in Figure 3.35 it is the narrower features of the stamp but the wider features of the imprint that are prone to shrinkage. To avoid confusion, AFM profiles of master, stamp and imprint are depicted analogously to Figure 3.35. Furthermore, cavities appear narrower and protrusions appear wider than they actually are due to the tip influence of AFM measurements as discussed in Section 3.2.7.1.

Figure 3.36 shows the AFM profile of R2R-imprinted line and space patterns for an acrylate resin (TMP(EO)$_9$TA) which is also used as stamp material in this case. AFM profiles of the stamp and the silicon master are depicted as well. During the R2R process a number of imprints are fabricated and Figure 3.36 shows the first imprint and the stamp after six imprints. As discussed in Section 3.3.6.2 the polymer stamp which is fabricated in a batch process does not suffer from shrinkage and its shape is almost identical to the silicon master. The R2R-imprint height, however, is reduced by about 5 % compared to the master whereas the lateral dimensions match exactly (small deviations due to tip influence). This is already

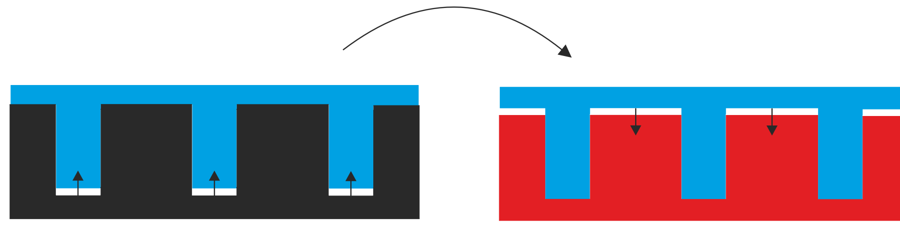

Figure 3.35: When interpreting AFM profiles on has to keep in mind that it is the resin that shrinks. In the illustration above the narrower features are prone to shrinkage during the replication of the master (black) to fabricate the polymer stamp (blue). However, when replicating the stamp to get the imprints (red) the wieder features are prone to shrinkage.

quite good, but coming from the results of the batch process the height reduction of the R2R imprint is unexpected and the question remains the reason for that is. Figure 3.36 also shows that the bottom of the imprinted features is not even but has a small tail. This defect is probably a distortion generated during the separation process because of the low strength of TMP(EO)$_9$TA. Also a deformation of the stamp is visible at one location for the same reason.

In addition to the acrylate, R2R-imprinting is performed with a thiol-ene, Karenz-TVCH as imprint material. It is chosen because of its low viscosity ($\eta = 52\ mPas$ as measured by rheometry), relatively good mechanical properties as the monomers have three and four functional groups, respectively and a good shelf-life stability due to Karenz. The stamp is made of E8210/HDDA. The result is the same as before as depicted in Figure 3.37. The shape of the polymer stamp matches the silicon master whereas the R2R-imprint height is reduced by about 5 %, similar to TMP(EO)$_9$TA. Both exhibit similar bulk shrinkage values but Karenz-TVCH should be able to further reduce the effect of shrinkage due to its delayed gel-point at $DC = 41$ % which, apparently, does not happen. The reasons for this will be discussed in more detail later on. Defects as they occurred in the case of the TMP(EO)$_9$TA-imprint are not visible and the feature bottoms are even indicating that Karenz-TVCH is better suited than TMP(EO)$_9$TA.

The height reduction of features imprinted in the R2R process is unexpected since all imprints performed in the batch process showed no shrinkage. Therefore, the question arises if it is really shrinkage induced by polymerization that causes the height reduction. To clarify this, R2R imprinting is performed with TMPTA as imprint resin which has a bulk shrinkage of 14 %. Therefore, the height reduction should be more pronounced than for TMP(EO)$_9$TA and Karenz-TVCH. Figure 3.38 shows, however, that it is about 4 % which is similar to the other two resins and well below the bulk shrinkage of TMPTA. This finding indicates that bulk polymerization shrinkage has no influence on the height reduction. To further elucidate this a polymer stamp is replicated in a batch process but using the R2R-UV lamp as illumination source. The stamp is made of E8210/HDDA and the imprint material is TMP(EO)$_9$TA. The illumination time and intensity is the same as in the R2R process. Figure 3.39 shows that the height of the imprinted features equals that of the polymer stamp (small tails at the feature bottoms generated due to demolding), so no significant shrinkage occured. The width of the imprinted features are a bit wider than the stamp cavities which, again, is due to the AFM tip influence. The result is the same for resins other than TMP(EO)$_9$TA. First of all, this

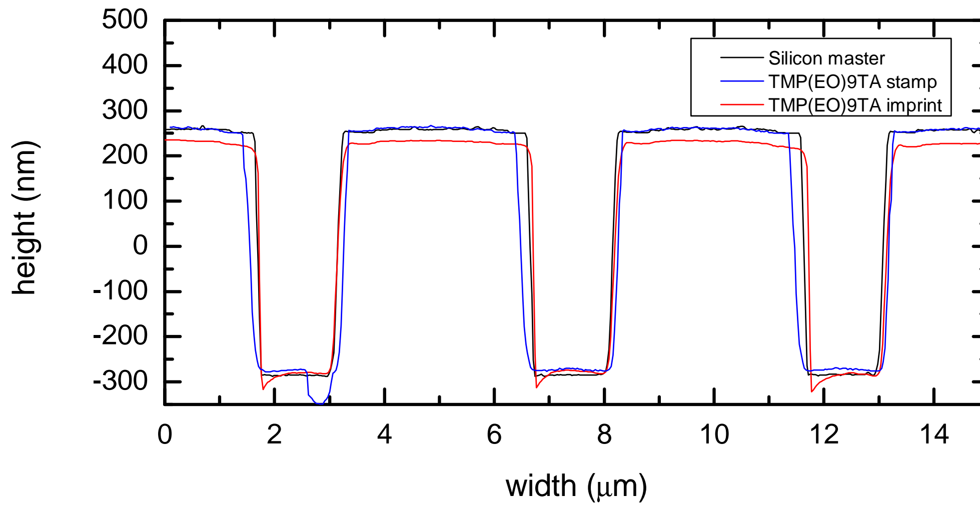

Figure 3.36: AFM profiles of R2R-imprinted line and space patterns with $TMP(EO)_9TA$ as imprint and stamp material. In contrast to the polymer stamp that was produced in a batch process the height of the imprinted features is reduced (5 %) compared to the silicon master.

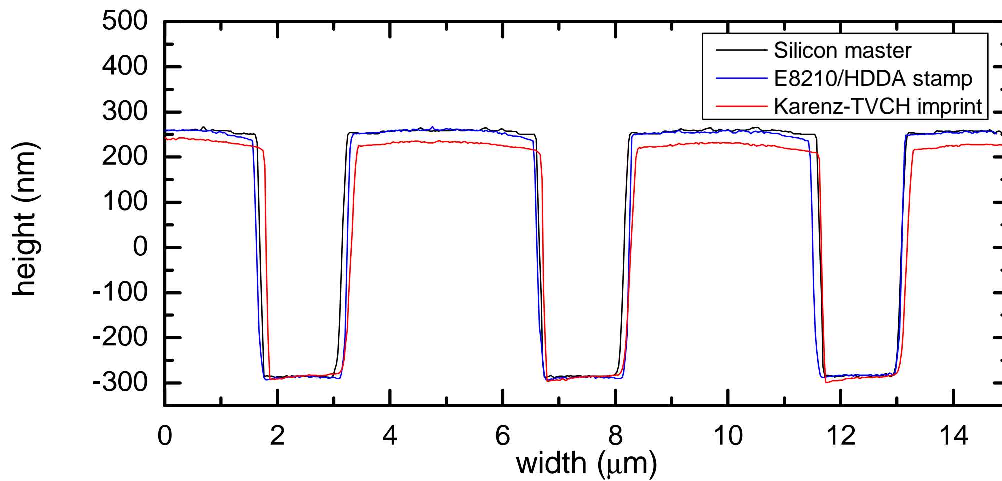

Figure 3.37: AFM profiles of R2R-imprinted line and space patterns with Karenz-TVCH as imprint material. The stamp is made of E8210/HDDA. In contrast to the polymer stamp that was produced in a batch process the height of the imprinted features is reduced (5 %) compared to the silicon master.

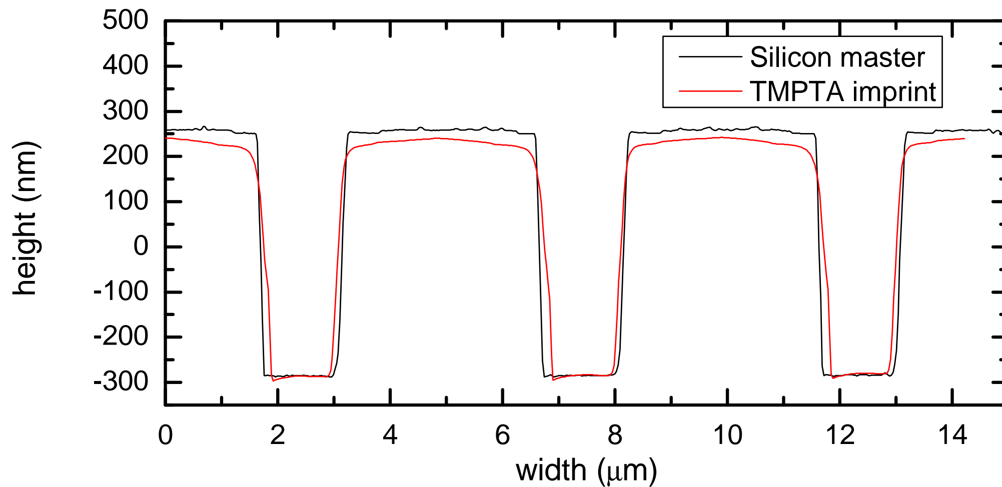

Figure 3.38: AFM profiles of R2R-imprinted line and space patterns with TMPTA as imprint material. The stamp is made of E8210/HDDA. The height of the imprinted features is reduced (4 %) compared to the silicon master.

shows that it is not the high light intensity used in the R2R process compared to the batch process which is responsible for the height reduction. Furthermore, this indicates that the height reduction has nothing to do with the polymerization at all, corroborating the results of the TMPTA-imprint.

What else can be the reason for the height reduction observed in the R2R process? Demolding is not likely to be responsible as it rather leads to deformations like the tails visible in Figure 3.39 or fracture of some features while others are unaffected as will be discussed later on, but not to a uniform height reduction. Imprints performed with Karenz-TVCH and TMPTA do not exhibit any sign of such defects (at least at the beginning of the R2R process) but do show the height reduction of about 4 %. Another possibility would be incomplete filling of the mold cavities with liquid resin before polymerization since filling in the R2R process is different from the batch process. In the batch process a liquid drop is deposited on the stamp and covered with the PET foil which causes the liquid resin to spread due to capillary forces. This leads to a lateral filling of the mold cavities. In contrast, during the R2R process the PET foil is first coated with the liquid resin. Afterwards, the stamp is pushed into the resin from above, so the filling rather happens vertically than laterally. Maybe this causes incomplete filling, e.g. due to entrapped gas. The vertical penetration of the stamp into the resin is no contradiction to roller-like imprinting because the radius of the mold cylinder is 20 cm. Therefore, the curvature is negligible at the size scale of the feature width (1 μm), i.e. a flat stamp is a good approximation. This is true for line and space patterns arranged perpendicular to the web movement but for lines parallel to the web direction gas entrapping should not be an issue as it can easily escape along the lines. However, the height reduction was observed in either case - patterns parallel and perpendicular to the web direction. Therefore, the height reduction of R2R imprinted features is not completely clear.

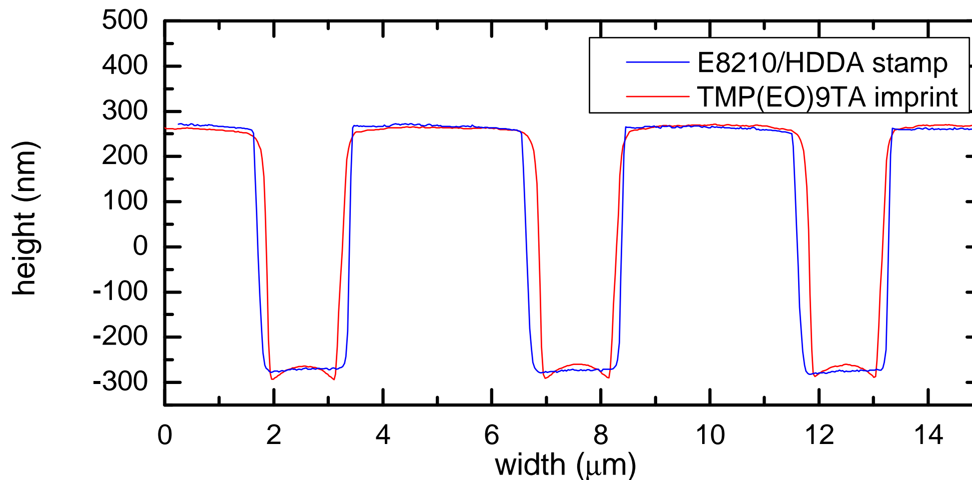

Figure 3.39: AFM-profiles of line and space patterns with TMP(EO)$_9$TA as imprint material replicated from a E8210/HDDA-polymer stamp in a batch process using the R2R-UV lamp as illumination source.

3.3.7.2 Long-term behavior

The height reduction is, however, only 5 % which is sufficiently small for most applications. A much greater issue is mechanical failure of the material during demolding which can generate defects at the imprint as well as at the stamp. This is particularly important regarding the long-time stability of the stamp since the aim is to produce thousands of imprints in a continuous process. Therefore, the development of replication fidelity is investigated over a number of imprint cycles. The silicon template consists of simple test structures such as lines and spaces, pillars, crosses and cross hatches with widths of 200 *nm*, 400 *nm*, 800 *nm* and 1600 *nm* with various pitches. Figure 3.40 shows an electron microscopic image of several features with nominal width of 200 *nm* that were R2R imprinted using Karenz-TVCH as imprint resin and E8210/HDDA as stamp material. The height of all structures is about 550 *nm* as measured by AFM. Figures 3.41-3.44 show light microscopic images of the imprinted test structures using Karenz-TVCH as resin. The 200 *nm* patterns of the first imprint show only a few small defects (Figure 3.41) but the quality of the fifteenth imprint is not good anymore (Figure 3.42). Figure 3.43 shows 200 *nm* patterns of the polymer stamp after fifteen imprints which are contaminated due to fracture of the imprint material. So, the decreased quality of the fifteenth imprint compared to the first is not due fracture of the stamp but of the imprint material. Apparently, the defects are not due to material fatigue of the stamp but due to degradation of the adhesive properties. The 1600 *nm* structures still worked well after fifteen imprints as depicted in Figure 3.44. This demonstrates that it is more difficult to replicate features with high aspect ratio as already discussed in Section 2. The mechanical strength of the imprint resin (Karenz-TVCH) seems to be sufficient for 1600 *nm* structures, but not for the 200 *nm* structures for which a material with higher strength would be desirable (maybe a stamp with lower modulus would also solve this problem - see Section 3.3.5). Furthermore, the cross hatches seem to be more stable than single lines. Figure 3.45 shows the sixth imprint of 800 *nm* structures with TMP(EO)$_9$TA as imprint and stamp material which is worse than the

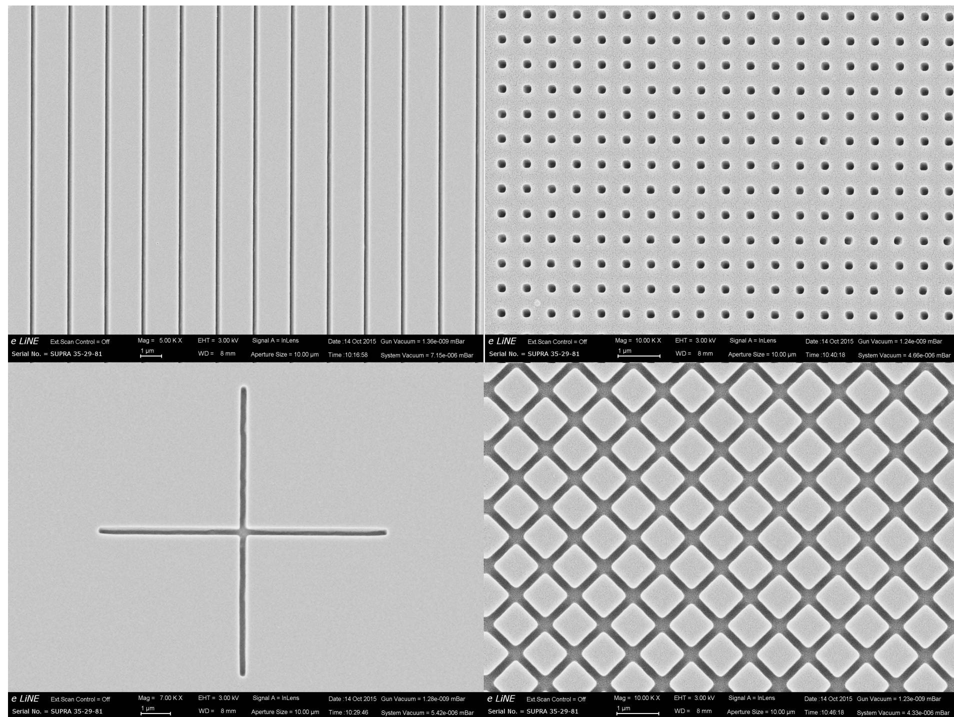

Figure 3.40: Various nanopatterns with a nominal width of 200 *nm* that were R2R imprinted using Karenz-TVCH as imprint resin: lines and spaces (top left), array of holes (top right), crosses (bottom left) and cross-hatches (bottom right).

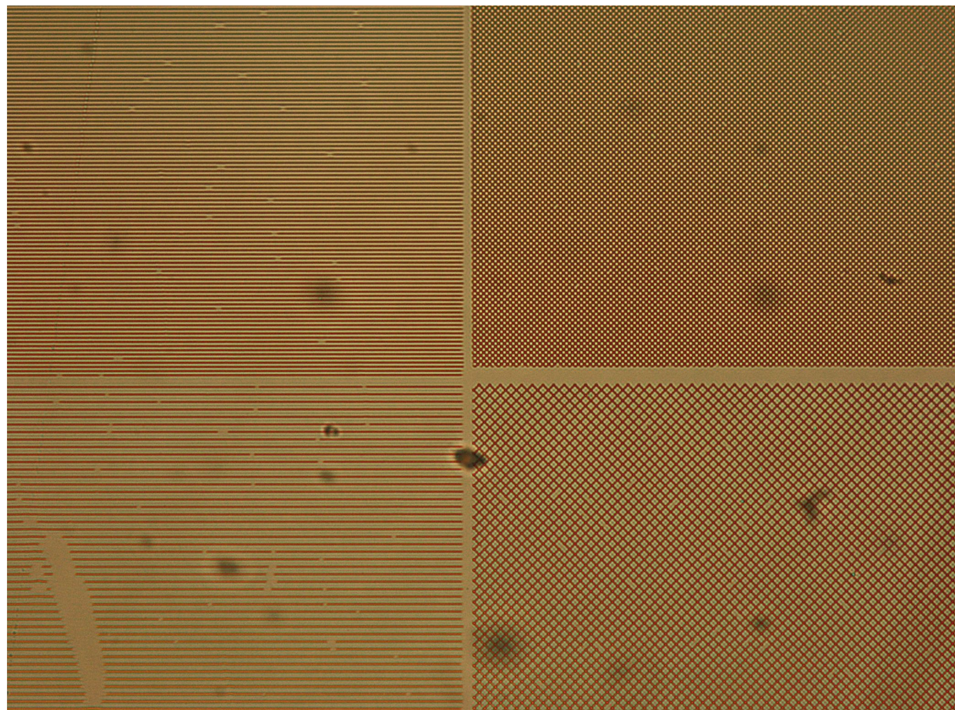

Figure 3.41: First imprint of 200 *nm* structures with Karenz-TVCH at 50x magnification. Only a few small defects are visible.

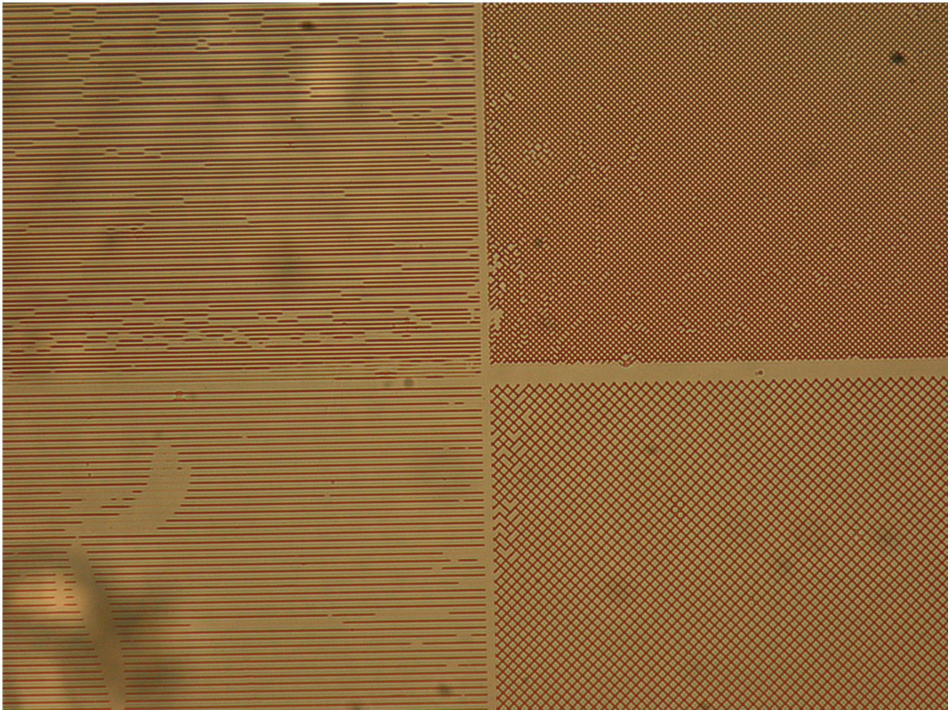

Figure 3.42: Fifteenth imprint of 200 nm structures with Karenz-TVCH at 50x magnification. The replication fidelity is not good anymore.

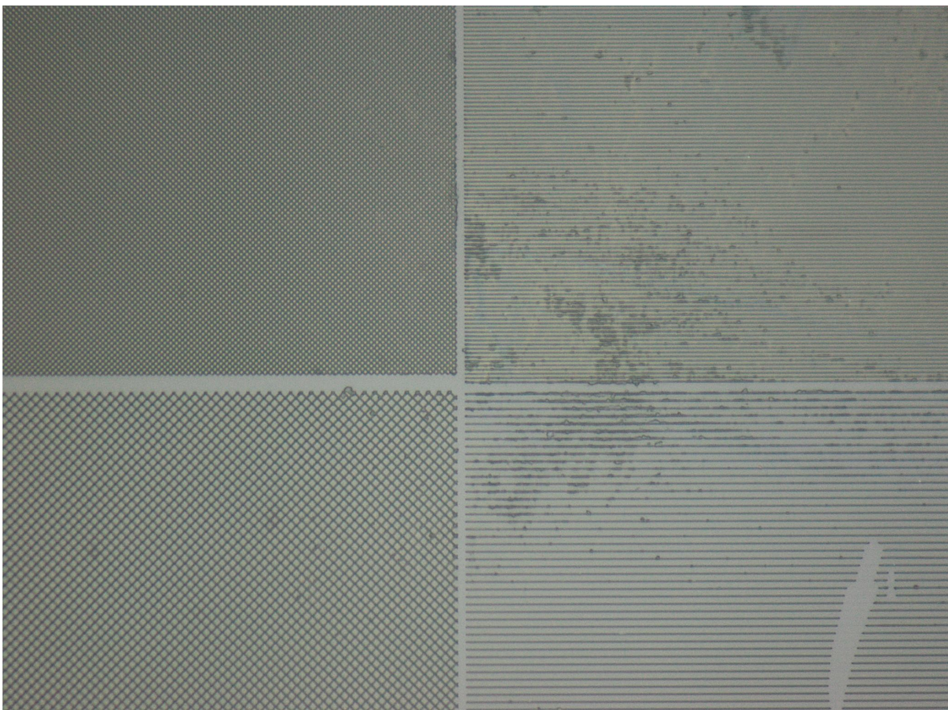

Figure 3.43: Polymer stamp after fifteen imprints of 200 nm structures with Karenz-TVCH at 50x magnification. The stamp is contaminated by the imprint material.

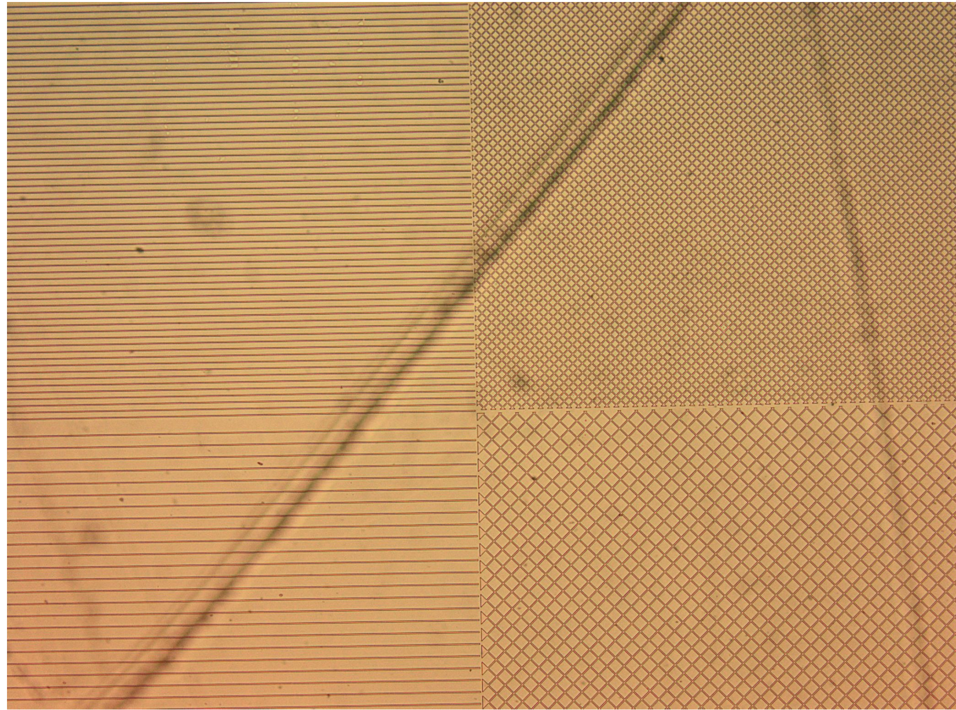

Figure 3.44: Fifteenth imprint of 1600 *nm* structures with Karenz-TVCH at 10x magnification. The pattern is replicated faithfully.

use of E8210/HDDA and Karenz-TVCH as stamp and imprint material, respectively which is probably due to the increased strength of E8210/HDDA. Figures 3.46-3.49 show the imprinted and stamp features of a R2R-process using TMPTA as imprint material and E8210/HDDA as stamp material. The first imprint of 200 *nm* structures worked well (Figure 3.46), whereas the eighth imprint shows some missing features (Figure 3.47). In contrast to Karenz-TVCH this is not because the imprinted features broke but because the stamp was damaged as depicted in Figure 3.48. Apparently, the modulus of TMPTA is too high to ensure defect-free demolding. The 1600 *nm* structures still worked well after eight imprints (Figure 3.49) demonstrating that a lower aspect ratio is less prone to defects during demolding.

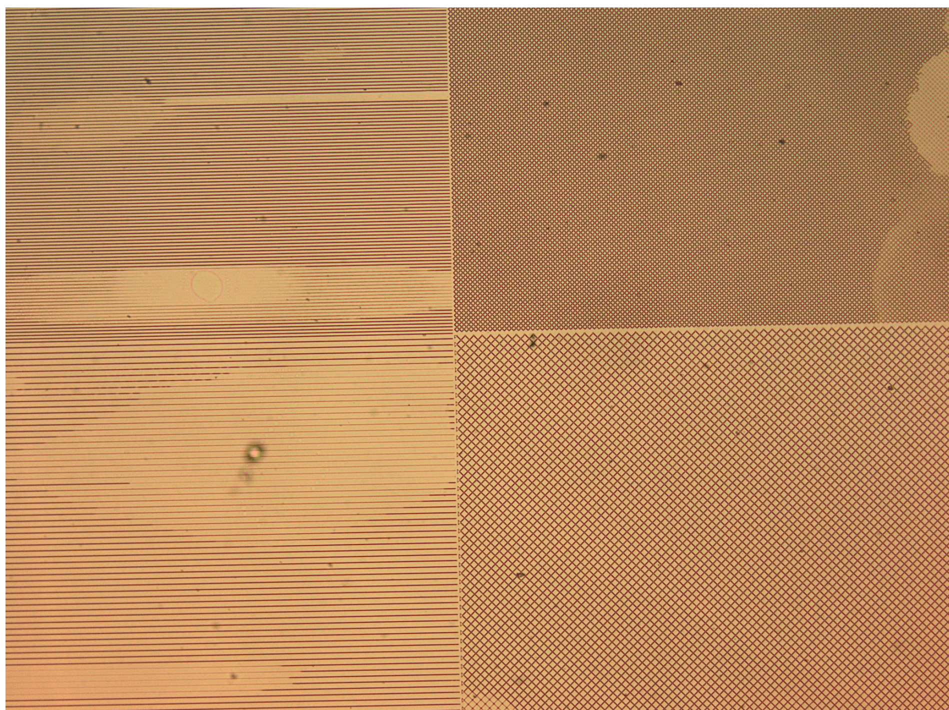

Figure 3.45: Sixth imprint of 800 nm structures with TMP(EO)$_9$TA at 10x magnification. The replication fidelity is not good.

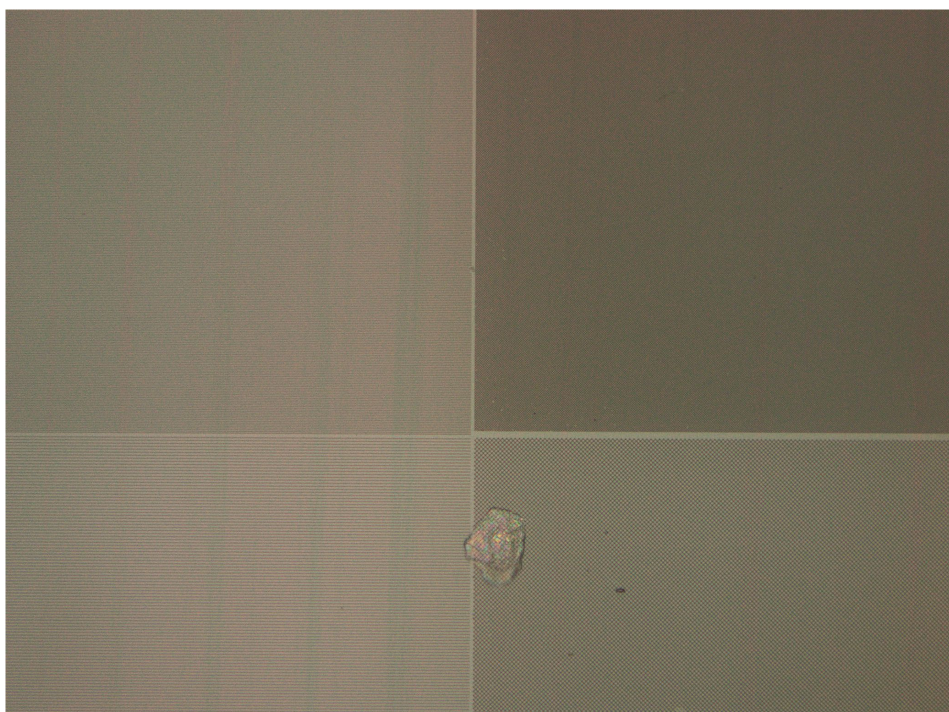

Figure 3.46: First imprint of 200 nm structures with TMPTA at 20x magnification. The pattern is faithfully replicated.

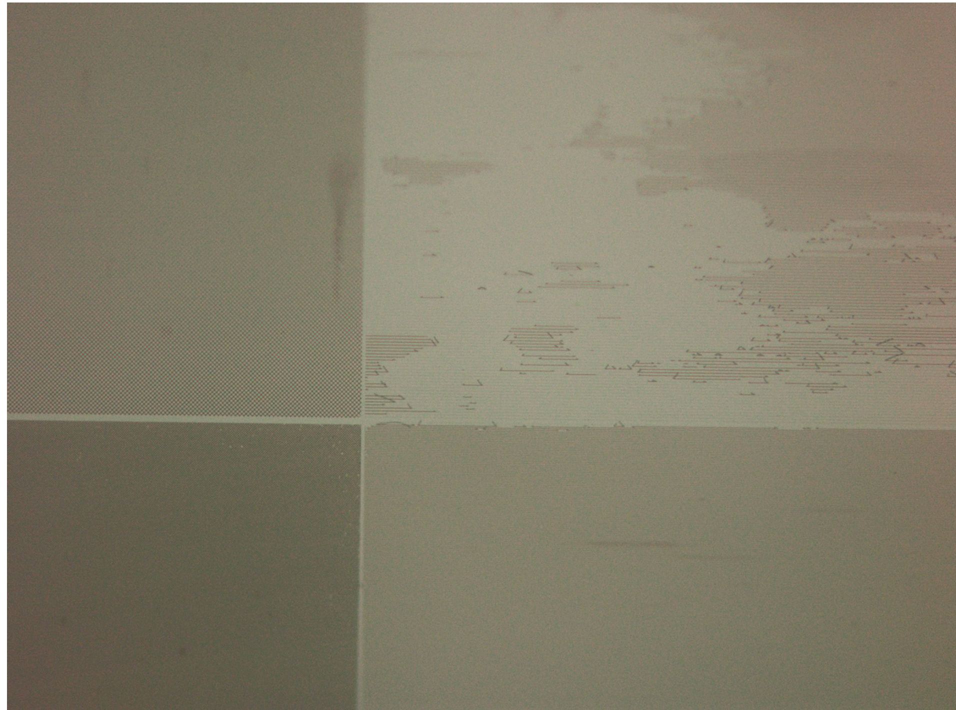

Figure 3.47: Eighth imprint of 200 *nm* structures with TMPTA at 20x magnification. Some of the features are missing.

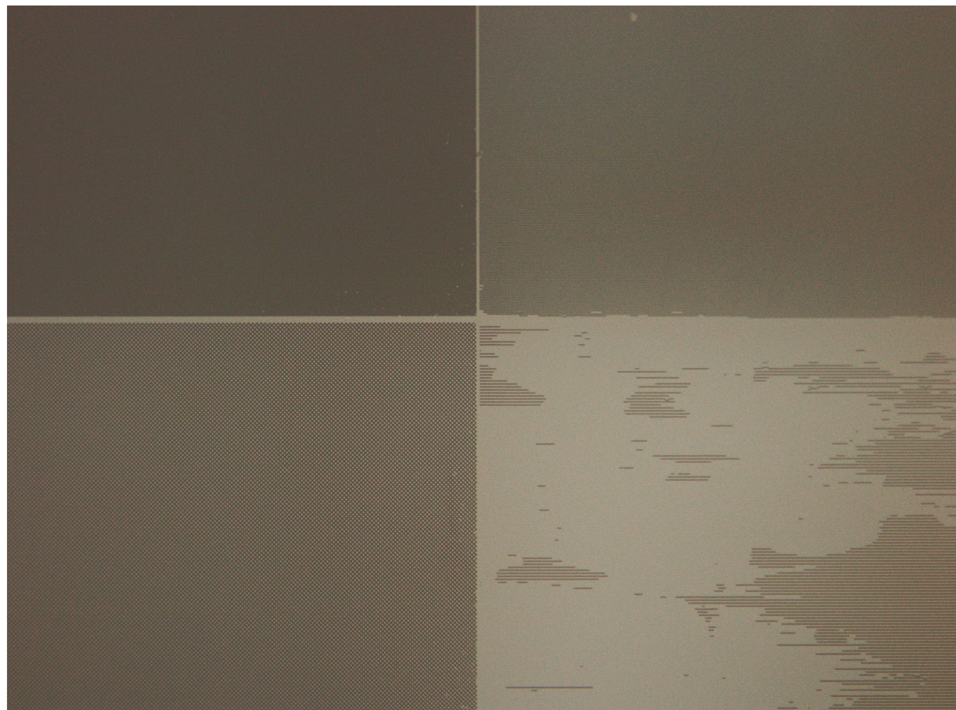

Figure 3.48: Polymer stamp after eight imprints of 200 *nm* structures with TMPTA at 20x magnification. Some of the features are missing.

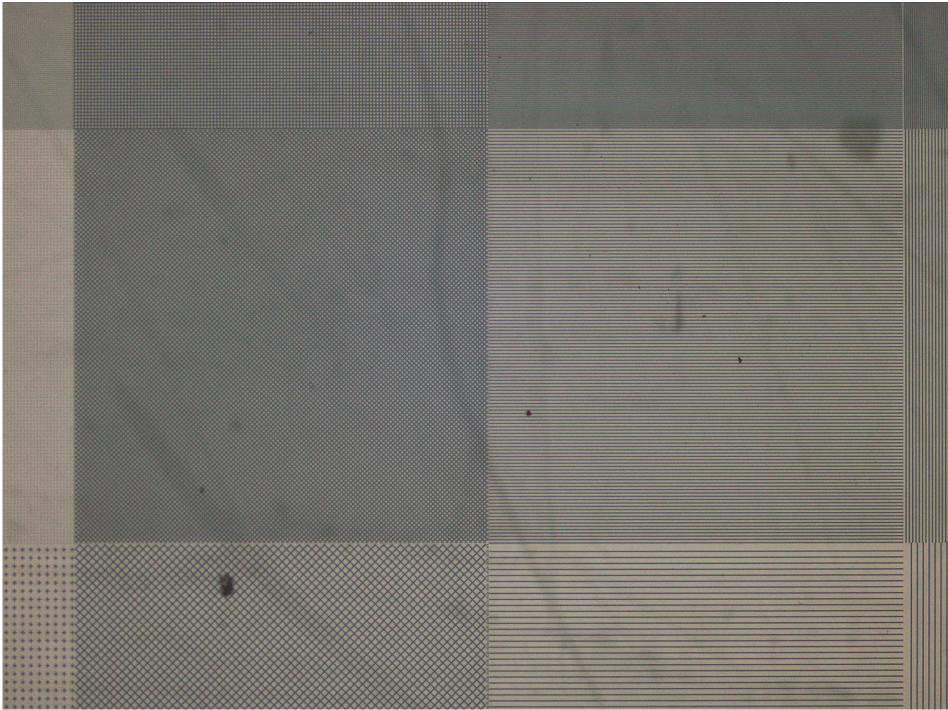

Figure 3.49: Polymer stamp after eight imprints of 1600 *nm* structures with TMPTA at 5x magnification. The pattern is faithfully replicated.

3.4 Summary

Currently, photolithography is the key technique of the semiconductor industry to fabricate integrated circuits. The need to continuously decrease the pattern size is a challenge for this method because the wavelength puts restrictions on the photolithographic resolution, which is why the costs of this process are drastically increasing. A promising alternative is ultraviolet light-assisted nanoimprint lithography (UV-NIL) which replicates a surface pattern by pressing it into a liquid monomer solution which polymerizes and gets rigid upon exposure to UV light before removing the original pattern. UV-NIL can be performed in a continuous way by roll-to-roll UV-NIL (R2R-UV-NIL) that is capable of mass-producing nanostructures at large-areas and low cost. Typically, imprint resins are based on acrylates which, however, exhibit some drawbacks such as oxygen inhibition, incomplete conversion, slow reaction, large polymerization shrinkage, shrinkage-induced stress and network inhomogeneity. Thiol-enes have the potential to overcome these limitations and it is the aim of the present work to investigate how they can be used to improve conventional imprint resins.

Before coming to the experimental part, the theoretical background of the roll-to-roll process is presented to understand which material properties are desirable for the imprint resin. Note that the R2R-UV-NIL process is not understood in its full complexity so far. For example, calculation of the time that is required for the liquid resin to fill the mold cavities is a complex issue. Also the demolding step has not been completely clarified yet. Furthermore, the theory of photopolymerization is discussed and how the molecular structure of monomers can be exploited to tune the properties of the prepolymer mixture as well as of the final polymer.

The experimental work comprises a series of techniques to characterize the liquid as well

as the cured resin. Rheometry, contact angle measurement, Fourier-transform infrared spectroscopy, hydrostatic weighing and microindentation are employed to measure the viscosity, surface energy, polymerization rate and final conversion, volumetric shrinkage and mechanical properties, respectively. Furthermore, the replication fidelity is investigated using light microscopy, electron microscopy, profilometry and atomic force microscopy.

Many of the properties of thiol-enes are due to the fact that they follow a step-growth mechanism, unlike acrylates which polymerize via chain-growth. To gain a better understanding of the thiol chemistry not only thiol-enes are investigated, but also a thiol-acrylate system is studied in which the thiol content is gradually increased. This should go hand in hand with a gradual transition from pure chain-growth to a mixed step-chain-growth in which the step-growth mechanism gets increasingly pronounced.

The investigation of time-dependent conversion showed that the final conversion of the studied acrylate could be increased from 70 % to 100 % by adding a structural similar thiol monomer. At the same time the polymerization rate was greatly increased. The time to reach its full conversion is reduced by a factor of ten for a 50/50 mixture compared to the pure acrylate. Most of the thiol-enes showed even faster polymerizations and they all exhibit near-complete conversion. Different photoinitiators have been tested as well, showing that they offer another possibility to increase the reactivity. The measured data were fitted to a semi-empirical equation for all monomer mixtures that were examined.

Polymerization-induced shrinkage was investigated for bulk samples of several acrylates, the thiol-acrylate system and some thiol-enes. The measured shrinkage values are related to basic monomer properties such as number of functional groups, density and molar mass via a semi-empirical equation. As expected, thiol-enes exhibit significantly lower volumetric shrinkage than conventional acrylates. The investigation of the thiol-acrylate system showed that shrinkage is not affected very much by the addition of thiols because the decrease in shrinkage is compensated to some extent by the increased conversion. Mechanical properties of thiol-enes, like elastic modulus and hardness, are generally restricted to lower values than it is the case for acrylates. However, by using stiff molecules glass transition temperatures well beyond room temperature and hence high elastic moduli can be achieved with thiol-enes as well. Their hardness can, however, not compete with that of acrylates making them less scratch resistant, for example. Another advantage of thiol-enes is their increased network homogeneity and that they build up much lower stress during polymerization. The implications of mechanical properties on the demolding step of NIL are discussed as well. A disadvantage of thiol-enes is their limited shelf-life stability but this is not a severe barrier towards their application because they can be used as two component systems, i.e. separate storage of thiol and ene monomers.

After having characterized the bulk properties of thiol-enes nanoimprint lithography is examined. Since low adhesion between mold and imprint is crucial for successful demolding the surface energy of both the silicon masters and imprinted polymers has to be as low as possible and values as low as 10 mJ/m^2 are realized. For silicon masters this is achieved by the deposition of a fluorinated self-assembled monolayer. For polymers a fluorinated surfactant is used which allows to adjust the surface energy independently from other properties. During the investigation of NIL it turned out that acrylates are usually easy to separate from the template after imprinting leading to defect-free replications in most cases. In contrast, thiol-enes generally adhere well to the stamps and relatively high forces have to be applied to separate them. Therefore, replications often have a bad quality. The good adhesion properties of thiol-enes are well known the reason being the low build-up of polymerization-induced stress.

As mentioned before, volumetric shrinkage occurs in the case of bulk samples, which is a well known fact and can be up to 15 % in the case of acrylates. A major part of this work was to investigate to what extend thiol-enes can be used to decrease the effect of shrinkage since it is desirable that the imprinted features have the same size and shape as the template features. The experimental findings of this work strongly indicate that shrinkage does not significantly reduce the size of the imprinted features, which is quite surprising. Possible explanations for this are discussed and it is probably because the resin is constrained by the mold cavities whereas bulk samples are allowed to shrink freely. In literature, there are contradicting results on the role of shrinkage during NIL and additionally, many works about replication fidelity focus on defects generated during demolding and do not consider polymerization shrinkage. Nevertheless, this finding means that one of the biggest advantages of thiol-enes, namely their potential to reduce the effect of shrinkage on the replication fidelity, due to their lower overall shrinkage and delayed gelation, is redundant because of the general lack of shrinkage. Despite the lack of polymerization-induced shrinkage, the height of features imprinted in the R2R process is reduced by about 5 %. The origin is, however, not completely understood. It was shown that this height reduction is independent of the bulk shrinkage of the monomer and that the high light intensity used in the R2R-process has no significant influence on shrinkage during NIL. This height reduction might be a problem for optical devices, for example, where accurate shape replication is essential [74] but is sufficiently small for most applications.

In summary, thiol-enes were shown to be superior to acrylates in several aspects as they provide reduced oxygen inhibition, nearly complete conversion, very fast reactions, reduced polymerization shrinkage, low stress and improved network homogeneity. Unfortunately, defect-free demolding often fails due to their good adhesion making them less well-suited as imprint material than acrylates. But when used as additives up to concentrations of 20 %, thiols and thiol-enes might still be a valuable means to enhance the performance of imprint resins. Finally, when imprint and stamp material are chosen properly, the R2R-UV-NIL process used in the present work is capable of replicating nanostructures at high throughput with high replication fidelity.

4 Outlook

Since thiol-enes are superior to acrylates in several aspects it would be desirable to make them suitable for R2R-UV-NIL. One aspect of future work might be the investigation of ternary thiol-ene-acrylate systems which are expected to combine the advantageous properties of both thiol-enes and acrylates. Another approach to improve thiol-enes might be the use of ene monomers containing urethane groups which provide additional mechanical strength due to their hydrogen bonds. This might enable thiole-enes to tolerate the stresses during demolding and make them suitable for imprint resins. This might also comprise the synthesis of appropriate ene monomers containing urethane groups. In this respect also an improved understanding of demolding would be desirable. In this work indications were found that the demolding force not only depends on surface energy but is also affected by the elastic modulus of the resin and the stress which is induced by polymerization. To further investigate this an experimental setup would be necessary which is capable of measuring the demolding force. An optimization of the resin regarding demolding force might not only enable the use of thiol-enes as imprint resins but would also be beneficial for the long-term stability of R2R-UV-NIL. Improved theoretical understanding would also be desirable regarding the lack of shrinkage to understand if this is generally true or if there are certain prerequisites for this effect. Furthermore, future work will comprise tuning the resin properties with respect to the intended application, e.g. weatherability for outdoor applications, while maintaining its imprintability.

Bibliography

[1] L Jay Guo. Recent progress in nanoimprint technology and its applications. *Journal of Physics D: Applied Physics*, 37(11):R123, 2004.

[2] Nazrin Kooy, Khairudin Mohamed, Lee Tze Pin, and Ooi Su Guan. A review of roll-to-roll nanoimprint lithography. *Nanoscale research letters*, 9(1):1–13, 2014.

[3] Jarrett J Dumond and Hong Yee Low. Recent developments and design challenges in continuous roller micro-and nanoimprinting. *Journal of Vacuum Science & Technology B*, 30(1):010801, 2012.

[4] L Jay Guo. Nanoimprint lithography: methods and material requirements. *Advanced Materials*, 19(4):495–513, 2007.

[5] Helmut Schift. Nanoimprint lithography: An old story in modern times? a review. *Journal of Vacuum Science & Technology B*, 26(2):458–480, 2008.

[6] A Fuchs, M Bender, U Plachetka, L Kock, N Koo, T Wahlbrink, and H Kurz. Lithography potentials of uv-nanoimprint. *Current Applied Physics*, 8(6):669–674, 2008.

[7] 10 emerging technologies that will change the world. *MIT Technology Review*, 2003. `http://www2.technologyreview.com/featured-story/401775/10-emerging-technologies-that-will-change-the/`.

[8] Stephen Y Chou, Peter R Krauss, and Preston J Renstrom. Imprint of sub-25 nm vias and trenches in polymers. *Applied physics letters*, 67(21):3114–3116, 1995.

[9] Andrea Cattoni, H Anne-Marie, Dominique Decanini, Jian Shi, and Jing Chen. *Soft UV nanoimprint lithography: a versatile tool for nanostructuration at the 20nm scale*. INTECH Open Access Publisher, 2011.

[10] Stephen Y Chou, Peter R Krauss, Wei Zhang, Lingjie Guo, and Lei Zhuang. Sub-10 nm imprint lithography and applications. *Journal of Vacuum Science & Technology B*, 15(6):2897–2904, 1997.

[11] Jan Haisma, Martin Verheijen, Kees Van Den Heuvel, and Jan Van Den Berg. Mold-assisted nanolithography: A process for reliable pattern replication. *Journal of Vacuum Science & Technology B*, 14(6):4124–4128, 1996.

[12] Douglas J Resnick, SV Sreenivasan, and C Grant Willson. Step & flash imprint lithography. *Materials today*, 8(2):34–42, 2005.

[13] Suho Ahn, Joowon Cha, Ho Myung, Seok-min Kim, and Shinill Kang. Continuous ultraviolet roll nanoimprinting process for replicating large-scale nano-and micropatterns. *Applied physics letters*, 89(21):213101, 2006.

[14] Se Hyun Ahn and L Jay Guo. High-speed roll-to-roll nanoimprint lithography on flexible plastic substrates. *Advanced materials*, 20(11):2044–2049, 2008.

[15] Se Hyun Ahn and L Jay Guo. Large-area roll-to-roll and roll-to-plate nanoimprint lithography: a step toward high-throughput application of continuous nanoimprinting. *ACS nano*, 3(8):2304–2310, 2009.

[16] Jarrett J Dumond, Kambiz Ansari Mahabadi, Yew Sok Yee, Christina Tan, Jerry Ying Hsi Fuh, Heow Pueh Lee, and Hong Yee Low. High resolution uv roll-to-roll nanoimprinting of resin moulds and subsequent replication via thermal nanoimprint lithography. *Nanotechnology*, 23(48):485310, 2012.

[17] Tai Yeon Lee, Jacquelyn Carioscia, Zachary Smith, and Christopher N Bowman. Thiol-allyl ether-methacrylate ternary systems. evolution mechanism of polymerization-induced shrinkage stress and mechanical properties. *Macromolecules*, 40(5):1473–1479, 2007.

[18] Theodor Posner. Beiträge zur kenntniss der ungesättigten verbindungen. ii. ueber die addition von mercaptanen an ungesättigte kohlenwasserstoffe. *Berichte der deutschen chemischen Gesellschaft*, 38(1):646–657, 1905.

[19] Thierry Darmanin and Frédéric Guittard. Superhydrophobic and superoleophobic properties in nature. *Materials Today*, 18(5):273–285, 2015.

[20] René Hensel. *Robust omniphobic surfaces by mimicking the springtail skin morphology*. PhD thesis, Saechsische Landesbibliothek-Staats-und Universitaetsbibliothek Dresden, 2014.

[21] Guoyong Xie, Guoming Zhang, Feng Lin, Jin Zhang, Zhongfan Liu, and Shichen Mu. The fabrication of subwavelength anti-reflective nanostructures using a bio-template. *Nanotechnology*, 19(9):095605, 2008.

[22] Rotogravure process. *Discovery Flexibles*, 2008. `http://www.discoveryflexibles.com/rotogravure/`.

[23] Soon-min Seo, Tae-il Kim, and Hong H Lee. Simple fabrication of nanostructure by continuous rigiflex imprinting. *Microelectronic engineering*, 84(4):567–572, 2007.

[24] LJ Heyderman, H Schift, C David, J Gobrecht, and T Schweizer. Flow behaviour of thin polymer films used for hot embossing lithography. *Microelectronic Engineering*, 54(3):229–245, 2000.

[25] Siddharth Chauhan. *Modeling and defect analysis of step and flash imprint lithography and photolithography*. PhD thesis, The University of Texas, 2010.

[26] Aydin Akgerman and John L Gainer. Predicting gas-liquid diffusivities. *Journal of Chemical and Engineering Data*, 17(3):372–377, 1972.

[27] Xiaogan Liang, Hua Tan, Zengli Fu, and Stephen Y Chou. Air bubble formation and dissolution in dispensing nanoimprint lithography. *Nanotechnology*, 18(2):025303, 2007.

[28] Se-Jin Choi, Dongha Tahk, and Hyunsik Yoon. Spontaneous dewetting-induced residue-free patterning at room temperature. *Journal of colloid and interface science*, 340(1):74–81, 2009.

[29] A Martin, J Clain, A Buguin, and F Brochard-Wyart. Wetting transitions at soft, sliding interfaces. *Physical Review E*, 65(3):031605, 2002.

[30] Jan-Michael Y Carrillo and Andrey V Dobrynin. Molecular dynamics simulations of nanoimprinting lithography. *Langmuir*, 25(22):13244–13249, 2009.

[31] Antonin Marchand, Joost H Weijs, Jacco H Snoeijer, and Bruno Andreotti. Why is surface tension a force parallel to the interface? *American Journal of Physics*, 79(10):999–1008, 2011.

[32] K Kendall. Thin-film peeling-the elastic term. *Journal of Physics D: Applied Physics*, 8(13):1449, 1975.

[33] RS Rivlin. *The effective work of adhesion*. Springer, 1997.

[34] John A Williams and James J Kauzlarich. The influence of peel angle on the mechanics of peeling flexible adherends with arbitrary load–extension characteristics. *Tribology International*, 38(11):951–958, 2006.

[35] Christopher Kovalchick and Alain Molinari. Mechanics of peeling for extensible elastic adhesive tapes. 2009.

[36] K Kendall. Shrinkage and peel strength of adhesive joints. *Journal of Physics D: Applied Physics*, 6(15):1782, 1973.

[37] Tomoki Nishino, Norihiro Fujikawa, Hiroaki Kawata, and Yoshihiko Hirai. Evaluation of demolding energy for various demolding modes in embossing process. *Japanese Journal of Applied Physics*, 52(6S):06GJ05, 2013.

[38] G Fischer, A Hagemeyer, J Dembowski, and H Hibst. Improvement of adhesion of co-cr layers by plasma surface modifications of the pet substrate. *Journal of adhesion science and technology*, 8(2):151–161, 1994.

[39] Kwang-Seop Kim, Jae-Hyun Kim, Hak-Joo Lee, and Sang-Rok Lee. Tribology issues in nanoimprint lithography. *Journal of mechanical science and technology*, 24(1):5–12, 2010.

[40] S Landis, N Chaix, C Gourgon, and T Leveder. Quantitative characterizations of a nanopatterned bonded wafer: force determination for nanoimprint lithography stamp removal. *Nanotechnology*, 19(12):125305, 2008.

[41] Reinhold Schwalm. *UV coatings: basics, recent developments and new applications*. Elsevier, 2006.

[42] Alborz Amirsadeghi, Jae Jong Lee, and Sunggook Park. Polymerization shrinkage stress measurement for a uv-curable resist in nanoimprint lithography. *Journal of Micromechanics and Microengineering*, 21(11):115013, 2011.

[43] Takahiro Shiotsu, Naoki Nishikura, Masaaki Yasuda, Hiroaki Kawata, and Yoshihiko Hirai. Simulation study on the template release mechanism and damage estimation for various release methods in nanoimprint lithography. *Journal of Vacuum Science & Technology B*, 31(6):06FB07, 2013.

[44] Ewa Andrzejewska. Photopolymerization kinetics of multifunctional monomers. *Progress in polymer science*, 26(4):605–665, 2001.

[45] Devdatt L Kurdikar and Nikolaos A Peppas. A kinetic model for diffusion-controlled bulk crosslinking photopolymerizations. *Macromolecules*, 27(15):4084–4092, 1994.

[46] James V Crivello and Elsa Reichmanis. Photopolymer materials and processes for advanced technologies. *Chemistry of Materials*, 26(1):533–548, 2013.

[47] George Odian. *Principles of polymerization*. John Wiley & Sons, 2004.

[48] Neil B Cramer, Tanner Davies, Allison K O'Brien, and Christopher N Bowman. Mechanism and modeling of a thiol-ene photopolymerization. *Macromolecules*, 36(12):4631–4636, 2003.

[49] Johan G Kloosterboer. Network formation by chain crosslinking photopolymerization and its applications in electronics. In *Electronic applications*, pages 1–61. Springer, 1988.

[50] Christopher N Bowman and Christopher J Kloxin. Toward an enhanced understanding and implementation of photopolymerization reactions. *AIChE Journal*, 54(11):2775–2795, 2008.

[51] NB Cramer, JW Stansbury, and CN Bowman. Recent advances and developments in composite dental restorative materials. *Journal of dental research*, 90(4):402–416, 2011.

[52] JG Kloosterboer and GFCM Lijten. Photopolymers exhibiting a large difference between glass transition and curing temperatures. *Polymer*, 31(1):95–101, 1990.

[53] Mickael Krzeminski, Michael Molinari, Michel Troyon, and Xavier Coqueret. Characterization by atomic force microscopy of the nanoheterogeneities produced by the radiation-induced cross-linking polymerization of aromatic diacrylates. *Macromolecules*, 43(19):8121–8127, 2010.

[54] JG Kloosterboer and GFCM Lijten. The influence of vitrification on the formation of densely crosslinked networks using photopolymerization. In *Biological and Synthetic Polymer Networks*, pages 345–355. Springer, 1988.

[55] Kristi S Anseth, Christopher N Bowman, and Nikolaos A Peppas. Polymerization kinetics and volume relaxation behavior of photopolymerized multifunctional monomers producing highly crosslinked networks. *Journal of Polymer Science Part A: Polymer Chemistry*, 32(1):139–147, 1994.

[56] Eui Kyoon Kim and C Grant Willson. Thermal analysis for step and flash imprint lithography during uv curing process. *Microelectronic engineering*, 83(2):213–217, 2006.

[57] Marko Vogler, Sabine Wiedenberg, Michael Mühlberger, Iris Bergmair, Thomas Glinsner, Holger Schmidt, Ernst-Bernhard Kley, and Gabi Grützner. Development of a novel, low-viscosity uv-curable polymer system for uv-nanoimprint lithography. *Microelectronic engineering*, 84(5):984–988, 2007.

[58] Ryan L Burns, Stephen C Johnson, Gerard M Schmid, Eui K Kim, Michael D Dickey, Jason Meiring, Sean D Burns, Nicholas A Stacey, C Grant Willson, Diana Convey, et al. Mesoscale modeling for sfil simulating polymerization kinetics and densification. In *Microlithography 2004*, pages 348–360. International Society for Optics and Photonics, 2004.

[59] David C Watts. Reaction kinetics and mechanics in photo-polymerised networks. *Dental Materials*, 21(1):27–35, 2005.

[60] Nick Silikas, Abdulaziz Al-Kheraif, and David C Watts. Influence of p/l ratio and peroxide/amine concentrations on shrinkage-strain kinetics during setting of pmma/mma biomaterial formulations. *Biomaterials*, 26(2):197–204, 2005.

[61] Hui Lu, Jacquelyn A Carioscia, Jeffery W Stansbury, and Christopher N Bowman. Investigations of step-growth thiol-ene polymerizations for novel dental restoratives. *Dental Materials*, 21(12):1129–1136, 2005.

[62] MP Patel, M Braden, and KWM Davy. Polymerization shrinkage of methacrylate esters. *Biomaterials*, 8(1):53–56, 1987.

[63] Yu Jian, Yong He, Tongzhou Jiang, Chunguang Li, Wantai Yang, and Jun Nie. Polymerization shrinkage of (meth) acrylate determined by reflective laser beam scanning. *Journal of Polymer Science Part B: Polymer Physics*, 50(13):923–928, 2012.

[64] J De Boer, RJ Visser, and GP Melis. Time-resolved determination of volume shrinkage and refractive index change of thin polymer films during photopolymerization. *Polymer*, 33(6):1123–1126, 1992.

[65] Charles E Hoyle, Tai Yeon Lee, and Todd Roper. Thiol–enes: chemistry of the past with promise for the future. *Journal of Polymer Science Part A: Polymer Chemistry*, 42(21):5301–5338, 2004.

[66] Charles E Hoyle and Christopher N Bowman. Thiol–ene click chemistry. *Angewandte Chemie International Edition*, 49(9):1540–1573, 2010.

[67] Matthew J Kade, Daniel J Burke, and Craig J Hawker. The power of thiol-ene chemistry. *Journal of Polymer Science Part A: Polymer Chemistry*, 48(4):743–750, 2010.

[68] Charles E Hoyle, Andrew B Lowe, and Christopher N Bowman. Thiol-click chemistry: a multifaceted toolbox for small molecule and polymer synthesis. *Chemical Society Reviews*, 39(4):1355–1387, 2010.

[69] Andrew B Lowe. Thiol–ene “click” reactions and recent applications in polymer and materials synthesis: a first update. *Polymer Chemistry*, 5(17):4820–4870, 2014.

[70] M S Kharasch, A T Read, and Mayo F R. The peroxide effect in the addition of reagents to unsaturated compounds. xvi. the addition of thioglycolic acid to styrene and isobutylene. *Chem Ind*, 57(752), 1938.

[71] Neil B Cramer, Sirish K Reddy, Allison K O’Brien, and Christopher N Bowman. Thiol-ene photopolymerization mechanism and rate limiting step changes for various vinyl functional group chemistries. *Macromolecules*, 36(21):7964–7969, 2003.

[72] Sirish K Reddy, Oguz Okay, and Christopher N Bowman. Network development in mixed step-chain growth thiol-vinyl photopolymerizations. *Macromolecules*, 39(25):8832–8843, 2006.

[73] Jacquelyn A Carioscia, Hui Lu, Jeffrey W Stanbury, and Christopher N Bowman. Thiol-ene oligomers as dental restorative materials. *Dental Materials*, 21(12):1137–1143, 2005.

[74] Peng Jin, Nan Liu, Jie Lin, Jiubin Tan, and Philip D Prewett. Replication of micro-optical elements with continuous relief by ultraviolet embossing with thiol-ene-based resist. *Applied optics*, 50(21):4063–4067, 2011.

[75] Paricher Esfandiari, Samuel Clark Ligon, Jean Jacques Lagref, Richard Frantz, Zoubair Cherkaoui, and Robert Liska. Efficient stabilization of thiol-ene formulations in radical photopolymerization. *Journal of Polymer Science Part A: Polymer Chemistry*, 51(20):4261–4266, 2013.

[76] Zakaria Belbakra, Zoubair M Cherkaoui, and Xavier Allonas. Photocurable polythiol based (meth) acrylate resins stabilization: New powerful stabilizers and stabilization systems. *Polymer Degradation and Stability*, 110:298–307, 2014.

[77] Qin Li, Hui Zhou, and Charles E Hoyle. The effect of thiol and ene structures on thiol–ene networks: Photopolymerization, physical, mechanical and optical properties. *Polymer*, 50(10):2237–2245, 2009.

[78] J Heijboer. Modulus and damping of polymers in relation to their structure. *British Polymer Journal*, 1(1):3–14, 1969.

[79] Sebastian Koltzenburg, Michael Maskos, and Oskar Nuyken. *Polymere: Synthese, Eigenschaften und Anwendungen*. Springer, 2014.

[80] S Fakirov, FJ Baltá Calleja, and M Krumova. On the relationship between microhardness and glass transition temperature of some amorphous polymers. *Journal of Polymer Science Part B: Polymer Physics*, 37(13):1413–1419, 1999.

[81] P Bartolomeo, M Irigoyen, E Aragon, MA Frizzi, and FX Perrin. Dynamic mechanical analysis and vickers micro hardness correlation for polymer coating uv ageing characterisation. *Polymer degradation and stability*, 72(1):63–68, 2001.

[82] Jacquelyn A Carioscia, Lauren Schneidewind, Casey O'Brien, Robert Ely, Caitlin Feeser, Neil Cramer, and Christopher N Bowman. Thiol–norbornene materials: Approaches to develop high tg thiol–ene polymers. *Journal of Polymer Science Part A: Polymer Chemistry*, 45(23):5686–5696, 2007.

[83] Loren W Hill. Calculation of crosslink density in short chain networks. *Progress in organic coatings*, 31(3):235–243, 1997.

[84] Douglas R Miller and Christopher W Macosko. Network parameters for crosslinking of chains with length and site distribution. *Journal of Polymer Science Part B: Polymer Physics*, 26(1):1–54, 1988.

[85] M Żenkiewicz. Methods for the calculation of surface free energy of solids. *Journal of Achievements in Materials and Manufacturing Engineering*, 24(1):137–145, 2007.

[86] Krüss GmbH. *Practical contact angle measurement (1)-(5).* `https://cmi.epfl.ch/metrology/files/Kruss-DSA30/kruss-tn311-315-en.pdf`.

[87] Daniel K Owens and RC Wendt. Estimation of the surface free energy of polymers. *Journal of applied polymer science*, 13(8):1741–1747, 1969.

[88] Brookfield Engineering Laboratories, Inc. *More Solutions to Sticky Problems.*

[89] Brookfield Engineering Laboratories, Inc. *Brookfield DV-III Ultra programmable Rheometer Operating Instructions.*

[90] HF Shurvell. Spectra–structure correlations in the mid-and far-infrared. *Handbook of vibrational spectroscopy*, 2002.

[91] John Coates. Interpretation of infrared spectra, a practical approach. *Encyclopedia of analytical chemistry*, 2000.

[92] Barbara Stuart. *Infrared spectroscopy.* Wiley Online Library, 2005.

[93] Andrew R Hind, Suresh K Bhargava, and Anthony McKinnon. At the solid/liquid interface: Ftir/atr—the tool of choice. *Advances in colloid and interface science*, 93(1):91–114, 2001.

[94] Sheryl R Kane, Paul D Ashby, and Lisa A Pruitt. Atr-ftir as a thickness measurement technique for hydrated polymer-on-polymer coatings. *Journal of Biomedical Materials Research Part B: Applied Biomaterials*, 91(2):613–620, 2009.

[95] Bor-Sen Chiou and Saad A Khan. Real-time ftir and in situ rheological studies on the uv curing kinetics of thiol-ene polymers. *Macromolecules*, 30(23):7322–7328, 1997.

[96] Yu Jian, Yong He, Yukun Sun, Haitao Yang, Wantai Yang, and Jun Nie. Thiol–epoxy/thiol–acrylate hybrid materials synthesized by photopolymerization. *Journal of Materials Chemistry C*, 1(29):4481–4489, 2013.

[97] Jolanta Świderska, Zbigniew Czech, Waldemar Świderski, and Agnieszka Kowalczyk. Reducing of on polymerization shrinkage by application of uv curable dental restorative composites. *Polish Journal of Chemical Technology*, 16(3):51–55, 2014.

[98] AJ Hudson, SC Martin, M Hubert, and JK Spelt. Optical measurements of shrinkage in uv-cured adhesives. *Journal of Electronic Packaging*, 124(4):352–354, 2002.

[99] S Bandyopadhyay. A study of the volumetric setting shrinkage of some dental materials. *Journal of biomedical materials research*, 16(2):135–144, 1982.

[100] Hong Lin, Xia Wan, Xuesong Jiang, Qingkang Wang, and Jie Yin. A nanoimprint lithography hybrid photoresist based on the thiol–ene system. *Advanced Functional Materials*, 21(15):2960–2967, 2011.

[101] AJ De Gee, AJ Feilzer, and CL Davidson. True linear polymerization shrinkage of unfilled resins and composites determined with a linometer. *Dental Materials*, 9(1):11–14, 1993.

[102] Stephen W Hughes. Archimedes revisited: a faster, better, cheaper method of accurately measuring the volume of small objects. *Physics education*, 40(5):468, 2005.

[103] Warren Carl Oliver and George Mathews Pharr. An improved technique for determining hardness and elastic modulus using load and displacement sensing indentation experiments. *Journal of materials research*, 7(06):1564–1583, 1992.

[104] Warren C Oliver and Georges M Pharr. Measurement of hardness and elastic modulus by instrumented indentation: Advances in understanding and refinements to methodology. *Journal of materials research*, 19(01):3–20, 2004.

[105] Yang-Tse Cheng and Che-Min Cheng. Scaling, dimensional analysis, and indentation measurements. *Materials Science and Engineering: R: Reports*, 44(4):91–149, 2004.

[106] Enoch Kim, Younan Xia, and George M Whitesides. Micromolding in capillaries: applications in materials science. *Journal of the American Chemical Society*, 118(24):5722–5731, 1996.

[107] Achille Francone. *Materials and anti-adhesive issues in UV-NIL*. PhD thesis, Institut National Polytechnique de Grenoble-INPG, 2010.

[108] Nader Jalili and Karthik Laxminarayana. A review of atomic force microscopy imaging systems: application to molecular metrology and biological sciences. *Mechatronics*, 14(8):907–945, 2004.

[109] Franz J Giessibl. Advances in atomic force microscopy. *Reviews of modern physics*, 75(3):949, 2003.

[110] Bruker Corporation. *NanoScope Software 7.30 User Guide*, 2011.

[111] Veeco Instruments Inc. *Dektak 150 Profiler user's manual*, 2007.

[112] H Seiler. Secondary electron emission in the scanning electron microscope. *Journal of Applied Physics*, 54(11):R1–R18, 1983.

[113] KD Vernon-Parry. Scanning electron microscopy: an introduction. *III-Vs Review*, 13(4):40–44, 2000.

[114] Jacob John, YuYing Tang, Jonathan P Rothstein, James J Watkins, and Kenneth R Carter. Large-area, continuous roll-to-roll nanoimprinting with pfpe composite molds. *Nanotechnology*, 24(50):505307, 2013.

[115] Stuart S Williams, Scott Retterer, Rene Lopez, Ricardo Ruiz, Edward T Samulski, and Joseph M DeSimone. High-resolution pfpe-based molding techniques for nanofabrication of high-pattern density, sub-20 nm features: a fundamental materials approach. *Nano letters*, 10(4):1421–1428, 2010.

[116] Markus Leitgeb. Herstellung und charakterisierung flexibler stempel für r2r-nanoprägen. Master's thesis, Technische Universität Wien, 2014.

[117] Sirish K Reddy, Kristi S Anseth, and Christopher N Bowman. Modeling of network degradation in mixed step-chain growth polymerizations. *Polymer*, 46(12):4212–4222, 2005.

[118] Sirish K Reddy, Neil B Cramer, Allison K O'Brien, Tsali Cross, Rishi Raj, and Christopher N Bowman. Rate mechanisms of a novel thiol-ene photopolymerization reaction. In *Macromolecular Symposia*, volume 206, pages 361–374. Wiley Online Library, 2004.

[119] Nicole Stephenson Kenning, Beth A Ficek, Cindy C Hoppe, and Alec B Scranton. Spatial and temporal evolution of the photoinitiation rate for thick polymer systems illuminated by polychromatic light: selection of efficient photoinitiators for led or mercury lamps. *Polymer International*, 57(10):1134–1140, 2008.

[120] Hany F Sobhi. *Synthesis and Characterization of Acylphosphine Oxide Photoinitiators*. PhD thesis, Cleveland State University, 2008.

[121] Mustafa Uygun, Mehmet Atilla Tasdelen, and Yusuf Yagci. Influence of type of initiation on thiol–ene "click" chemistry. *Macromolecular Chemistry and Physics*, 211(1):103–110, 2010.

[122] Neil B Cramer and Christopher N Bowman. Kinetics of thiol–ene and thiol–acrylate photopolymerizations with real-time fourier transform infrared. *Journal of Polymer Science Part A: Polymer Chemistry*, 39(19):3311–3319, 2001.

[123] Vaibhav S Khire, Youngwoo Yi, Noel A Clark, and Christopher N Bowman. Formation and surface modification of nanopatterned thiol-ene substrates using step and flash imprint lithography. *Advanced Materials*, 20(17):3308–3313, 2008.

[124] JR Cahoon, WH Broughton, and AR Kutzak. The determination of yield strength from hardness measurements. *Metallurgical Transactions*, 2(7):1979–1983, 1971.

[125] EJ Pavlina and CJ Van Tyne. Correlation of yield strength and tensile strength with hardness for steels. *Journal of Materials Engineering and Performance*, 17(6):888–893, 2008.

[126] John Lopez. Microhardness testing of plastics: literature review. *Polymer testing*, 12(5):437–458, 1993.

[127] K-H CHUNG and EH Greener. Correlation between degree of conversion, filler concentration and mechanical properties of posterior composite resins. *Journal of Oral Rehabilitation*, 17(5):487–494, 1990.

[128] Alan Harrison and Robert A Draughn. Abrasive wear, tensile strength, and hardness of dental composite resins—is there a relationship? *The Journal of prosthetic dentistry*, 36(4):395–398, 1976.

[129] JP Berry. Fracture processes in polymeric materials. i. the surface energy of poly (methyl methacrylate). *Journal of Polymer Science*, 50(153):107–115, 1961.

[130] JP Berry. Fracture processes in polymeric materials. ii. the tensile strength of polystyrene. *Journal of Polymer Science*, 50(154):313–321, 1961.

[131] JP Berry. Fracture processes in polymeric materials. iii. topography of fracture surfaces of poly (methyl methacrylate). *Journal of Applied Physics*, 33(5):1741–1744, 1962.

[132] JP Berry. Fracture processes in polymeric materials. iv. dependence of the fracture surface energy on temperature and molecular structure. *Journal of Polymer Science Part A: General Papers*, 1(3):993–1003, 1963.

[133] JP Berry. Fracture processes in polymeric materials. v. dependence of the ultimate properties of poly (methyl methacrylate) on molecular weight. *Journal of Polymer Science Part A: General Papers*, 2(9):4069–4076, 1964.

[134] Alborz Amirsadeghi, Jae Jong Lee, and Sunggook Park. A simulation study on the effect of cross-linking agent concentration for defect tolerant demolding in uv nanoimprint lithography. *Langmuir*, 28(31):11546–11554, 2012.

[135] HM Pollock, D Maugis, and M Barquins. The force of adhesion between solid surfaces in contact. *Applied Physics Letters*, 33(9):798–799, 1978.

[136] Alborz Amirsadeghi, Jae Jong Lee, and Sunggook Park. Surface adhesion and demolding force dependence on resist composition in ultraviolet nanoimprint lithography. *Applied Surface Science*, 258(3):1272–1278, 2011.

[137] Xiangdong Ye, Yucheng Ding, Yugang Duan, Hongzhong Liu, and Bingheng Lu. Effects of exposure time on defects and demolding force in soft ultraviolet nanoimprint lithography. *Journal of Vacuum Science & Technology B*, 27(5):2091–2096, 2009.

[138] Weitao Jiang, Yucheng Ding, Hongzhong Liu, Bingheng Lu, Yongsheng Shi, Jinyou Shao, and Lei Yin. Two-step curing method for demoulding in uv nanoimprint lithography. *Microelectronic Engineering*, 85(2):458–464, 2008.

[139] Jakob Lange, Staffan Toll, Jan-Anders E Månson, and Anders Hult. Residual stress build-up in thermoset films cured above their ultimate glass transition temperature. *Polymer*, 36(16):3135–3141, 1995.

[140] Jakob Lange, Staffan Toll, Jan-Anders E Månson, and Anders Hult. Residual stress build-up in thermoset films cured below their ultimate glass transition temperature. *Polymer*, 38(4):809–815, 1997.

[141] Hiroshi Hiroshima and Kenta Suzuki. Study on change in uv nanoimprint pattern by altering shrinkage of uv curable resin. *Japanese Journal of Applied Physics*, 50(6S):06GK09, 2011.

[142] Luis M Campos, Ines Meinel, Rosette G Guino, Martin Schierhorn, Nalini Gupta, Galen D Stucky, and Craig J Hawker. Highly versatile and robust materials for soft imprint lithography based on thiol-ene click chemistry. *Advanced Materials*, 20(19):3728–3733, 2008.

[143] Erik C Hagberg, Michael Malkoch, Yibo Ling, Craig J Hawker, and Kenneth R Carter. Effects of modulus and surface chemistry of thiol-ene photopolymers in nanoimprinting. *Nano letters*, 7(2):233–237, 2007.

[144] Matthew Colburn, Itai Suez, Byung Jin Choi, Mario Meissl, Todd Bailey, SV Sreenivasan, John G Ekerdt, and C Grant Willson. Characterization and modeling of volumetric and mechanical properties for step and flash imprint lithography photopolymers. *Journal of Vacuum Science & Technology B*, 19(6):2685–2689, 2001.

[145] S Johnson, R Burns, EK Kim, M Dickey, G Schmid, J Meiring, S Burns, CG Willson, D Convey, Y Wei, et al. Effects of etch barrier densification on step and flash imprint lithography. *Journal of Vacuum Science & Technology B*, 23(6):2553–2556, 2005.

[146] CL Davidson and AJ Feilzer. Polymerization shrinkage and polymerization shrinkage stress in polymer-based restoratives. *Journal of Dentistry*, 25(6):435–440, 1997.

[147] Jeremy L Gilbert, Julie M Hasenwinkel, Richard L Wixson, and Eugene P Lautenschlager. A theoretical and experimental analysis of polymerization shrinkage of bone cement: a potential major source of porosity. *Journal of biomedical materials research*, 52(1):210–218, 2000.